Low Reynolds Number Fluid Dynamics with Applications to suspension feeding Animals

Finderup Nielsen, Niels

Publication date:
1991

Document Version
Publisher's PDF, also known as Version of record

REPORT 1

CILIATED PLANE CHANNEL FLOW WITH PRESSURE GRADIENT

Niels Finderup Nielsen.

Table of contents

CILIATED PLANE CHANNEL FLOW WITH PRESSURE GRADIENT

Niels Finderup Nielsen.

Abstract

The envelope model for cilia water propulsion is applied to the case of a two dimensional channel with ciliated parallel walls. Results of a perturbation analysis of the creeping flow are presented, in terms of the steady velocity (streaming) produced by oscillatory motions of two opposing flexible surfaces. Two specific cases are considered, that of no pressure gradient, and that of a finite pressure gradient. The latter case appears as a coupled flow problem including pressure gradient and induced streaming. The results indicate that effective propulsion (pumping) occurs for symplectic metachronism in ciliated channels with predominantly transverse waves, and for antiplectic metachronism in channels with predominantly longitudinal waves, in both cases provided the effective stroke is in the same direction as the streaming velocity. The ratio of the streaming velocity for the channel model and that of the single ciliated wall is discussed. This ratio shows the degree to which streaming is augmented or impeded by the flow interaction. It depends on phase relation, distance between the two sheets, and their amplitude ratio. The net flow arising from streaming and pressure gradient is shown as pump characteristics. These results, discussed for different phase relation and distance between the two sheets, are related qualitatively to known characteristics of the gill of *Mytilus edulis*.

1. Introduction

Fluid transport due to systems of beating cilia has been analyzed by two main approaches. The first approach, the sublayer model, was initiated by Blake (1972) (see also Liron & Mochon 1976a and Liron 1978) and approximates each cilium by a line of force singularities (stokeslets). The velocity field due to all cilia is then found by summing over all cilia. This model allows computation of the average fluid flow rate at any point inside or outside the cilia layer. The model applies to widely spaced cilia. The second approach, the envelope model, which will be the model considered here, replaces the array of closely packed cilia by an envelope of cilia tip profiles, which requires that

the cilia totally entrain the fluid in the interstitial space so that the exterior fluid essentially experiences the motion of a flexible surface whose motions roughly correspond to those of the cilium tips. This model is appropriate for many biological systems where the flow between neighboring cilia are unimportant because of close spacing, see Brennen & Winet (1977) for summary.

Basic mechanism of ciliary beating. – Each individual cilium has a regular beat pattern consisting of the effective stroke, which determines the direction of the induced flow, and the recovery stroke. In the effective stroke the cilium remains straight, or nearly so. During the recovery stroke, the cilium turns to its starting position through a bend propagation from the base to the tip of the cilium (figure 1).

In a given surface direction, a cilium beats slightly out of phase with its neighbours so as to produce a metachronal wave traveling over the surface.

In the two dimensional case, as considered here, the ciliary beat and the metachronal wave may be such that the direction of the effective stroke is opposite to the direction of wave propagation, as in figure 1b, or in the same direction, as in figure 1a. These two relations are called antiplectic and symplectic metachronism, respectively.

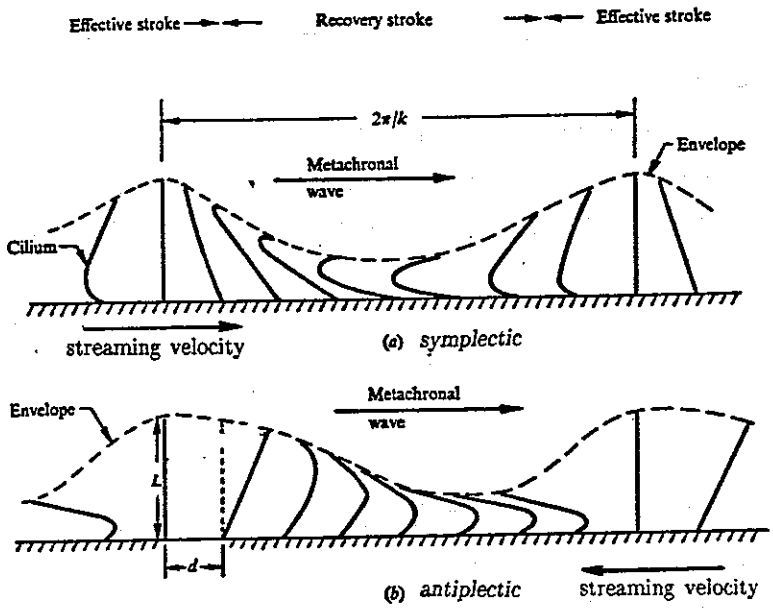

Figure 1. Schematic diagram of ciliary metachronism indicating the relative directions of metachronal wave propagation and streaming velocity for (a) symplectic and (b) antiplectic metachronism (adapted from Brennen & Winet 1977).

In the more general case, the motion is often three dimensional with some of the recovery stroke taking place out of the plane, as in the case of the lateral cilia of the gill

Mytilus edulis. In these cases, the motion is termed diaplectic (dexioplectic if the rotation from the metachronal wave direction to the effective stroke direction is 90^0 anti–clockwise, viewed from above, and laeoplectic if 90^0 clock–wise). These relationships were identified by Knight & Jones (1954) (see figure 2).

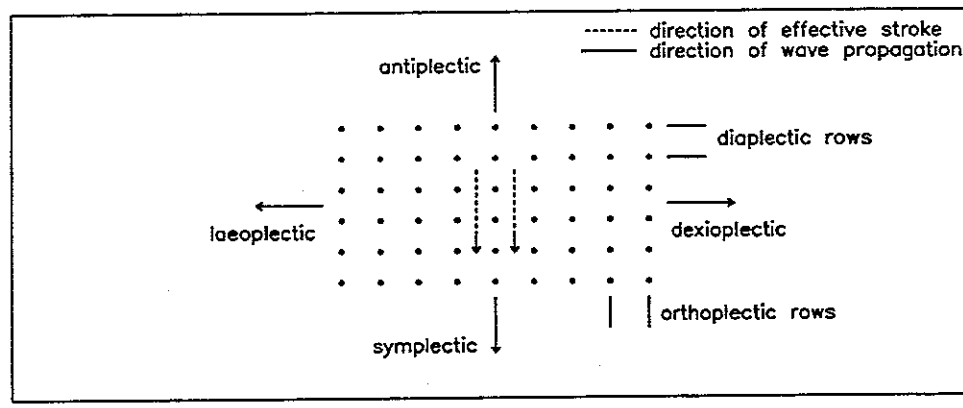

Figure 2. Nomenclature of ciliary patterns and metachronal waves given by Knight–Jones (1954). The arrows indicate the directions of metachronal waves in the various patterns.

As mentioned, the envelope model is appropriate for cilia that are sufficiently closely packed together, which is the case for symplectic metachronism, where the cilium beats in the same direction as the wave is progressing and the cilia are close together throughout the whole beat (see figure 1). This is contrary to that of antiplectic metachronism (a conclusion reached by Blake 1972, when using a sublayer model). However, Brennen (1974) pointed out a condition where the envelope model is valid for both symplectic and antiplectic metachronism,

$$\nu/\omega L >> kLd\,, \quad kd < 1\,, \tag{1}$$

where ν is the kinematic viscosity, ω the radian frequency ($\omega=2\pi f$), L the cilium length, d the base separation and k the wave number,$k=2\pi/\lambda$, λ being the wavelength.

Condition (1) is valid for many cilia systems, including that of *Mytilus edulis*. So, here we consider two dimensional cilium beat, represented by both symplectic and antiplectic waves. In the bands of lateral cilia on the gill filaments in *Mytilus edulis* the cilium beat is a more complicated three dimensional beat and the streaming velocity is perpendicular to the direction of the wave propagation. In spite of this we expect, from the present analyses, to obtain important information about cilia water propulsion in ciliated channels.

Considering the envelope model, the ciliary tip performs a simple harmonic motion where the amplitude of the longitudinal motion is a and the amplitude of the transverse motion is b. The longitudinal motion will lead the transverse motion by the phase angle φ and the metachronal wave will travel with velocity c ($c=\omega/k$), and wavelength λ ($k=2\pi/\lambda$), in the positive x–direction. If at any point x the longitudinal motion leads the transverse motion by a phase angle φ, then the various cilia loci that are so described are indicated in figure 3.

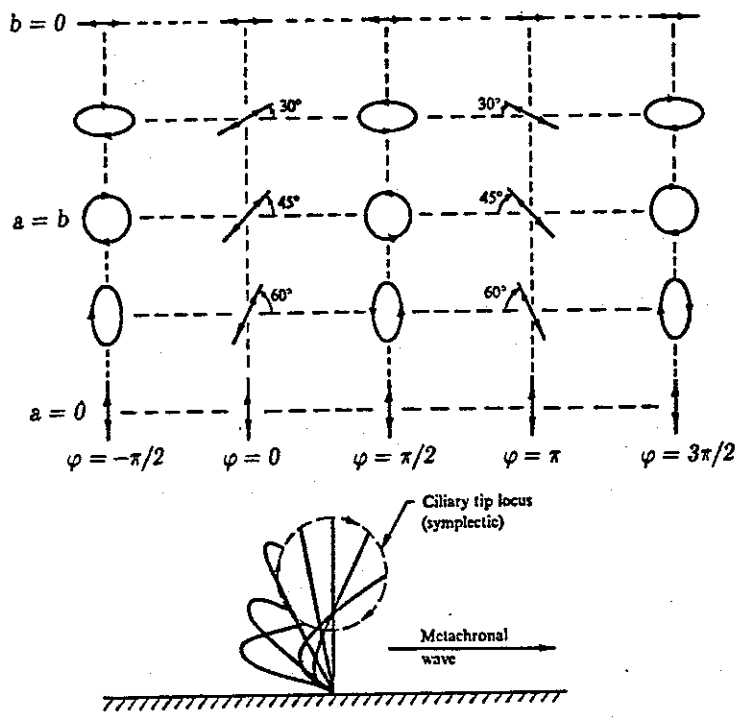

Figure 3. Variations of arbitrary elliptical ciliary tip loci with parameter a, b and φ. An example of a ciliary- tip locus (symplectic) is indicated in the lower part of the figure (adapted from Brennen & Winet 1977).

Preliminary rewiew of literature. – Many models have been made for water propulsion based on the two dimensional waving sheet. Taylor (1951) made an inextensible model of a transverse wave at zero Reynolds number. Reynolds (1965) introduced a first order movement in the longitudinal direction, as well as in the transverse direction by allowing the sinusoidal surface to strain. Tuck (1968) simplified Taylor and Reynolds results and considered longitudinal and transverse oscillations separately. Blake (1971b) considered longitudinal and transverse oscillations acting together which implied that the envelope surface would be quite different from the ones considered previously.

Other geometrically shaped models for external flows have been considered, such as the infinite long cylinder (Blake 1971b), traveling surface waves on a sphere (Blake 1971a), and a thin oscillating boundary layer on a sphere (Brennen 1974).

In the case of two dimensional channel flow Burns & Parkes (1967) considered transverse oscillations in the interior of a channel (peristaltic motion), subject to a zero pressure gradient. They also determined the frictional pressure drop associated with flow though a channel with fixed wavy walls. Here, we consider longitudinal movements as well as the transverse oscillations, and include an arbitrary pressure gradient. Besides, the oscillating walls may be out of phase (see figure 4).

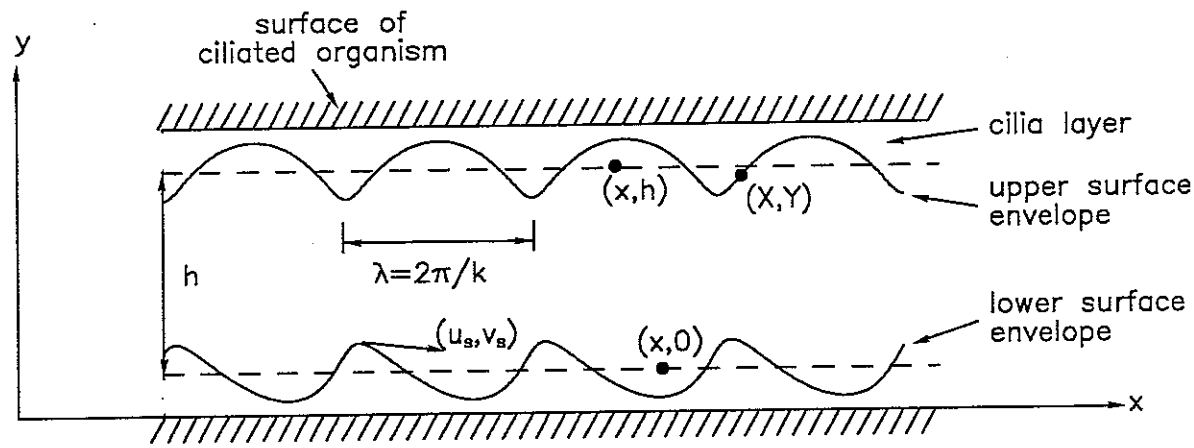

Figure 4. Schematic diagram illustrating the envelope over cilia. Coordinates (X,Y) represent envelope, (x,0) and (x,h) represent mean position.

The expressions for the streaming velocity are obtained with use of perturbation theory. The no slip condition is satisfied at the envelope surface by expanding the solution for the velocities in terms of small perturbations. From this we obtain an infinite set of linear equations which is truncated to the required order of accuracy. Presently, solutions are worked out to second order.

2. Formulation of the problem

Considering creeping motion at vanishing oscillatory Reynolds number ($\omega/k^2\nu$), inertia may be neglected and the two dimensional, incompressible flow is governed by

$$\nabla\cdot\mathbf{v} = 0 \quad ; \quad \nabla p = \mu\nabla^2\mathbf{v}\,, \tag{2}$$

where $\mathbf{v} = (u,v)$ denotes the velocity, p the pressure, and μ the dynamic viscosity, assumed to be constant. Here continuity is satisfied by introducing the stream function,

$$u = \frac{\partial \psi}{\partial y}, \qquad v = -\frac{\partial \psi}{\partial x}, \tag{3}$$

and the curl of the balance of momentum becomes

$$\nabla^4 \psi = 0 . \tag{4}$$

The oscillating extensible walls of the channel at $(x,y) = (X,Y)$, are defined by (see figure 4)

$$X_L = x + a\cdot\sin(z + \varphi_L) \quad ; \quad Y_L = b\cdot\sin(z) , \tag{5a}$$

$$X_U = x + a\cdot\sin(z + \varphi_U) \quad ; \quad Y_U = h - b\cdot\sin(z) , \tag{5b}$$

where L and U refer to lower and upper surface, respectively, a is the longitudinal and b the transversal amplitude, h the nominal channel width, φ the phase, and

$$z = \omega t - kx \tag{6}$$

is a convenient parameter representing a frame in which waves are stationary. Equation (6) describe progressive waves of velocity $c = \omega/k$ in the positive x direction, of frequency $f = \omega/2\pi$, of wave number k, and wavelength $\lambda = 2\pi/k$. Two different phase parameters give considerable flexibility. It is noted that the effective beat in the ciliated surfaces represented by (5) occurs near $z = \pi/2$ where the velocity component in x is $\dot{X} = -a\omega\sin(\varphi)$ (see (7) below). It therefore follows that (5) represent symplectic metachronism for $\pi < \varphi < 2\pi$ and antiplectic metachronism for $0 < \varphi < \pi$. Thus, any combination of metachronism of the two walls may be studied.

The boundary conditions are those of no slip along the walls, implying the following specified velocities at the upper and lower wall, respectively,

$$u_L = \dot{X}_L = a\omega(\cos z\cdot\cos\varphi_L - \sin z\cdot\sin\varphi_L) \quad ; \quad v_L = \dot{Y}_L = b\omega\cos z , \tag{7a}$$

$$u_U = \dot{X}_U = a\omega(\cos z\cdot\cos\varphi_U - \sin z\cdot\sin\varphi_U) \quad ; \quad v_U = \dot{Y}_U = -b\omega\cos z . \tag{7b}$$

A final volume condition of an externally imposed pressure gradient is needed for a complete statement of the problem of determining the volume flow through the channel. (the inverse problem of an externally imposed volume flow, with the aim at determining the pressure gradient, will not be considered). Following Burns & Parkes (1967) partial integration of (2) gives the condition

$$\Delta p = \mu \cdot \int_0^{\lambda} \nabla^2 u \, dx \, , \tag{8}$$

which may be evaluated at any value of y.

3. Perturbation solution

In view of the nature of the boundary conditions the solution to (4) is expressed as

$$\psi(x,y,t) = l_0 y^3 + m_0 y^2 + \frac{\omega}{k} \sum_{n=0}^{\infty} \Big\{ \sinh(nky) \Big[\Big[a_n + b_n y \Big] \sin(nz) + \Big[c_n + d_n y \Big] \cos(nz) \Big] + \cosh(nky) \Big[\Big[e_n + f_n y \Big] \sin(nz) + \Big[g_n + h_n y \Big] \cos(nz) \Big] \Big\} \, , \tag{9}$$

which implies the velocity components

$$u(x,y,t) = 3l_0 y^2 + 2m_0 y + \frac{\omega}{k} \sum_{n=0}^{\infty} \Big\{ \cosh(nky) \Big[\Big[nk \Big[a_n + b_n y \Big] + f_n \Big] \sin(nz) + \Big[nk \Big[c_n + d_n y \Big] + h_n \Big] \cos(nz) \Big] + \sinh(nky) \Big[\Big[nk \Big[e_n + f_n y \Big] + b_n \Big] \sin(nz) + \Big[nk \Big[g_n + h_n y \Big] + d_n \Big] \cos(nz) \Big] \Big\} \, , \tag{10a}$$

$$v(x,y,t) = \frac{\omega}{k} \sum_{n=0}^{\infty} nk \Big\{ \sinh(nky) \Big[\Big[a_n + b_n y \Big] \cos(nz) - \Big[c_n + d_n y \Big] \sin(nz) \Big] + \cosh(nky) \Big[\Big[e_n + f_n y \Big] \cos(nz) - \Big[g_n + h_n y \Big] \sin(nz) \Big] \Big\} \, , \tag{10b}$$

where coefficient l_0, m_0 and $a_n \cdots h_n$, to desired order, are determined from boundary conditions.

Inserting (10a) into (8) yields immediately

$$l_0 = -\frac{P}{6 \cdot \mu}, \tag{11}$$

where P denote the pressure drop per wavelength ($P=-\Delta p/\lambda$). Thus, positive P indicate imposed pressure gradient for symplectic metachronism and negative P indicate imposed pressure gradient for antiplectic metachronism (see figure 1 for definition of symplectic and antiplectic metachronism).

To approximately satisfy (7) at the actual location of the walls (5) we expand (10) in Taylor series, from (x,0) for the lower wall,

$$\begin{aligned} u(X_L,Y_L) &= u(x,0) + (X_L - x)\cdot\frac{\partial u}{\partial x}(x,0) + Y_L\cdot\frac{\partial u}{\partial y}(x,0) + \cdots, \\ v(X_L,Y_L) &= v(x,0) + (X_L - x)\cdot\frac{\partial v}{\partial x}(x,0) + Y_L\cdot\frac{\partial v}{\partial y}(x,0) + \cdots, \end{aligned} \tag{12a}$$

and from (x,h) for the upper wall,

$$\begin{aligned} u(X_U,Y_U) &= u(x,h) + (X_U - x)\cdot\frac{\partial u}{\partial x}(x,h) + (Y_U - h)\cdot\frac{\partial u}{\partial y}(x,h) + \cdots, \\ v(X_U,Y_U) &= v(x,h) + (X_U - x)\cdot\frac{\partial v}{\partial x}(x,h) + (Y_U - h)\cdot\frac{\partial v}{\partial y}(x,h) + \cdots. \end{aligned} \tag{12b}$$

Clearly the velocity (10) subject to (7) in terms of (12) is a series solution in dimensionless amplitudes ka and kb which must therefore be assumed small compared to unity. It is worth noting, as shown by Blake (1971b), that expanding (10) in Taylor series has the effect of making the series solution restricted in other variables, including the nondimensional channel width kh.

Then, to first order in ka,kb, employing the first term in (12), gives

$$m_0 = -\tfrac{3}{2}hl_0 \quad , \quad h_0 = 0 , \tag{13}$$

and the values of the coefficients $a_1 - h_1$, listed in the appendix. These coefficients can be solved in pairs and are, to this order, uncoupled from m_0 and l_0. As expected, the solution to this order consists of linear harmonic oscillations superposed a Poiseuille flow driven by P.

Next, to second order in ka,kb, employing the three terms in (12) it is necessary to recalculate m_0, h_0, a_1, b_1 and f_1 to determine the modified coupled flow problem arising from nonlinear terms. The calculations give

$$m_0 = -\frac{\omega}{2kb}\cdot\left[a_1+f_1+ka\cdot\sin\varphi_L\right] , \tag{14}$$

$$h_0 = \frac{1}{2}\cdot\frac{\omega}{k}\left\{ka\left[\sin\varphi_L\left[a_1+f_1\right]-\cos\varphi_L\left[c_1+h_1\right]\right]-kb\left[2b_1+e_1\right]\right\} , \tag{15}$$

and the new first order coefficients a_1, b_1 and f_1, which are solved numerically and listed in the appendix.

The time mean velocity of (10a) is calculated by integrating over the period T

$$\bar{u} = 3l_0y^2 + 2m_0y + h_0 , \tag{16}$$

and finally, integrating across the channel width from y=0 to h gives the resulting mean velocity in the channel,

$$U = l_0h^2 + m_0h + h_0 , \tag{17}$$

arising from the coupled flow problem including pressure gradient and induced streaming. It is worth notice that for the case of zero pressure gradient, l_0=0.

4. Discussion of the kinematics of the envelope model

In this section the oscillating surface envelope defined by equation (5) is discussed. Using a parametric representation for the envelope model and looking for the values of the parameter s where the tips of cilia are crossing each other we will find the permissible values of the model parameters.

The parametric representation for the lower surface envelope, for example, appears as

$$r(s) = [s+a\cdot\sin(\omega t-ks+\varphi),\ b\cdot\sin(\omega t-ks+\varphi)] , \tag{18}$$

where we are looking for crossings (double values of the function), that is, solutions to the equation

$$r(s_1) = r(s_2) \ , \tag{19}$$

implying the transcendental equation

$$ks + aksin\varphi \cdot cos(\omega t - ks) - \omega t + \pi(n+1/2) = 0, \ n=0,1,2,\cdots \tag{20}$$

A solution to equation (20) in terms of the nondimensional parameter ks denotes crossing while no solution denotes no crossing.

Without loss of generality, we set the time t equal to zero and (20) becomes

$$ks + aksin\varphi \cdot cos(ks) + \pi(n+1/2) = 0, \quad n=0,1,2, \cdots \tag{21}$$

An analysis of equation (21) shows that the criterion for no crossing is given by

$$-1 < ak \cdot sin\varphi < 1 \ . \tag{22}$$

Figures 5 and 6 show examples of crossing and no crossing, respectively.

It is worth noting that (22) is independent of the transversal amplitude b but dependents of the longitudinal amplitude a, wavelength λ, and phase φ. In a physical sense, a crossing indicates that, at a given position, two cilia tips are at the same position (see figure 5). The no crossing criteria given by (22) will, according to perturbation theory ($ak < 1$), always be satisfied. Therefore, the calculations done here are not subject to restrictions. However, when using models with greater amplitudes the envelope model (equation (5)) may not be sufficient.

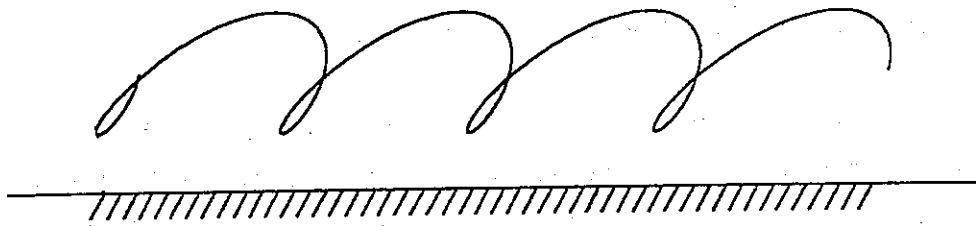

Figure 5. Envelope Model for cilia crossing ($ak \cdot sin\varphi$=1.48, see equation(22))

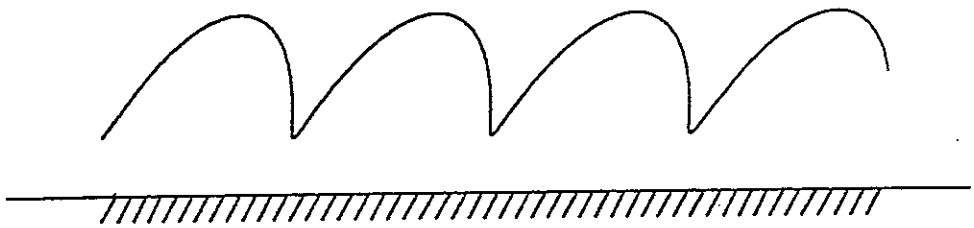

Figure 6. Envelope Model for no cilia crossing ($ak \cdot sin\varphi$=0.74, see equation(22))

5. Numerical results

In this section we consider the mean velocity, normalizes by the wave velocity, U/c, resulting from induced streaming and imposed pressure gradient, for the two dimensional channel given by (17). The results, are determined for different phase relations and amplitude ratios, implying different envelope surface forms.

Clearly, (17) is linear in the frequency f, and it can be shown that (17) is quadratic in the nondimensional amplitudes ka,kb and in the nondimensional channel width kh. The mean velocity of a viscous fluid through a uniform two dimensional channel is given by $U_P = Ph^2/12\mu$ which is the value of the net flow U when a=0, b=0. Now, introducing a new "pressure" parameter U_P/c we consider results of different values of the pressure parameter and related pump characteristics.

The equations have been solved for boundary conditions similar to those used by Burns & Parkes 1967. These correspond to peristaltic motion where the longitudinal amplitude a equals zero. The results show agreement with the second order case with no pressure gradient and are lower than the second order case with fixed boundary and a prescribed pressure gradient.

Parameter selection

Taking advantage of dimensionless parameters and confined attention to U/c, there still remains six parameters, kh, ka, kb, φ_L, φ_U, and U_P/c. Thus, a complete parameter study is not possible. Representative values for the lateral cilia in *Mytilus edulis* are f=15 Hz and λ=15 μm (see Brennen & Winet 1977), which yields $Re_\omega = 5.4 \cdot 10^{-4}$. Further, according to perturbation theory, ka and kb are small and we select the values of ka/kb=2.5 (ka=0.5, kb=0.2) and ka/kb=0.4 (ka=0.2, kb=0.5) which indicate predominantly longitudinal waves and predominantly transverse waves, respectively. In the numerical investigation the four remaining parameters (kh, φ_L, φ_U, and U_P/c) will be studied with special attention to the nondimensional channel width kh.

To obtain general results we are looking at variation of the asymptotic solutions ($hk \rightarrow \infty$) with phase angle φ_L and φ_U. These results also include the combination symplectic–antiplectic waves (see figure 1 for definition of symplectic and antiplectic metachronism) on the surface envelope which, in a ciliated channel, seems to be physically unrealistic and only of mathematical interest.

Generating symplectic and antiplectic waves is a matter of selecting different phase angles φ_L and φ_U (see equation (5) and figure 3). Figure 7 shows different surface envelope forms, and it is worth noting the considerable difference of symplectic and antiplectic wave forms.

Numerical results

Figure 8–11 show two cases, of amplitude ratio ka/kb=0.4 and amplitude ratio ka/kb=2.5 with no pressure gradient. This means that the mean velocity equals the streaming velocity originating from the oscillatory motions of the walls. First, in figures 8 and 9, we consider asymptotic solutions (hk=10) versus phases at the lower and upper wall φ_L and φ_U, and second, in figures 10 and 11, we consider solutions for spacing equal to about 1/3 wavelength (kh=2) versus phases.

For amplitude ratio ka/kb=0.4 (figure 8 and 10), it is found that the streaming velocity is always positive (positive x–direction as the wave propagation) and we notice the large values of streaming for the small spacing equal to about 1/3 wavelength. The maximum and minimum streaming velocity for φ_L and φ_U is equal to $3\pi/2$ and $\pi/2$, respectively. For amplitude ratio ka/kb=2.5 (figure 9 and 11) the streaming velocity is always negative, however, for spacing equal to about 1/3 wavelength we have positive values in the region of symplectic metachronism. Contrary to that of figure 8 and 10 we get maximum and minimum streaming, in the negative x–direction, for φ_L and φ_U equal to $\pi/2$ and $3\pi/2$, respectively.

Figures 12 and 13 show results for the streaming velocity normalized with the wave velocity U/c, versus channel width for different envelope surfaces defined by (5). Here we consider ciliated channels with symplectic or antiplectic waves on both surfaces.

Clearly, the streaming velocity depends on the phase, and for symplectic metachronism (figure 12) the streaming velocity in the positive x–direction decreases as the channel width increases. Figure 12 also shows the special case of peristaltic motion and it should be noted that the streaming is always lesser than the values obtained for channels with boundary conditions given by (5). For antiplectic metachronism (figure 13) it is found that the streaming in the negative x–direction increases as the channel width increases. However, here we find an overshoot for channel width in the region 1/6 to 1/2 wavelength.

It is worth noting that streaming velocity is symmetrical about $\varphi_L=\varphi_U=3\pi/2$ for symplectic metachronism and about $\varphi_L=\varphi_U=\pi/2$ for antiplectic metachronism (see figure 8–11).

Figures 14 and 15 show mean velocity normalized with wave velocity, U/c, versus channel width for different values of the pressure parameter U_P/c, which is proportional to the imposed pressure gradient in x. The mean velocity now equals net flow arising from both pressure gradient and induced streaming. It can be seen from figure 14 (ka/kb=0.4) and figure 15 (ka/kb=2.5) that the effect of a pressure gradient, positive or negative, diminishes with channel width. Calculations for other phase parameters than those used in figures 14 and 15 will give similar trends.

Next, consider the ciliated channel to be a pump subject to a back pressure ($U_P/c < 0$ for symplectic metachronism and $U_P/c > 0$ for antiplectic metachronism). Figures 16–18 show pump characteristics, in terms of pump head (equal to back pressure) versus flow, for different values of phases and spacing between the two sheets. The calculations are shown for both symplectic and antiplectic metachronism as well as for the special case of peristaltic motion. For clarity, all pressures and flows are shown as being positive. Figures 16a–c show pump characteristics for the case of amplitude ratio ka/kb=0.4, where different phase relations and distance between the two sheets are considered. Clearly, the most efficient pump is that of channel width kh=3.0 and phases $\varphi_L=3\pi/2$, $\varphi_U=3\pi/2$. In Figures 17a–c we consider the amplitude ratio ka/kb=2.5 and, as in figure 16, flow and pump head increases with decreasing spacing, in all cases being greatest when phases equal $\varphi_L=\pi/2$, $\varphi_U=\pi/2$. Figure 18 shows the special case of peristaltic motion, involving no phase relations. Again, the most efficient pump is clearly that of close spacing. Comparing figures 18, 16a and 17b for the case kh=3.0 shows that the peristaltic pump is good but not the best. Any of the cases of figure 16a shows better performance.

In conclusion, the most efficient pump will be that of symplectic metachronism, close spacing of two opposing sheets, and with the two walls in phase.

Finally, two examples of time mean velocity profiles are shown in figure 19, the two sheets being in phase, figure 19 upper part, and the two sheets out of phase, figure 19 lower part, for the two extreme cases, U=0 and P=0. As expected for the two cases (see equation (16)) we have a linear function for the purely streaming velocity (P=0) and a parabolic function for purely pressure driven flow (U=0). We notice that the case where the walls are in phase, the streaming velocity (P=0) is a constant.

6. Discussion

Mean velocity with no pressure gradient (streaming): – Consider the asymptotic solutions (figure 8 and 9) where the channel width is about 1.6 times the wavelength (hk=10) or more, and recall that the effective stroke is in the same direction as the streaming velocity ($\pi<\varphi<2\pi$ and $0<\varphi<\pi$ for symplectic and antiplectic metachronism, respectively, see figure 7). The asymptotic solutions then indicate symplectic metachronism for amplitude ratio ka/kb=0.4 with maximum streaming $U/c\simeq0.21$ for φ_L and φ_U equal to $3\pi/2$, and antiplectic metachronism for amplitude ratio ka/kb=2.5 with maximum streaming in the negative x–direction $U/c\simeq0.21$ for φ_L and φ_U equal to $\pi/2$. In conclusion, symplectic metachronism in ciliated channels appears at predominantly transverse waves and antiplectic metachronism appears at predominantly

longitudinal waves. Also the metachronism has an optimum for optimal wave form. These conclusions were also was obtained by Blake (1975) for the infinite sheet, and it is of interest to compare to this case.

The streaming velocity for the two dimensional waving sheet is given by (see, for example Brennen & Winet 1977)

$$U_s/c = \frac{1}{2}\cdot\left[-(ak)^2+(bk)^2-2\cdot ak\cdot bk\cdot\sin\varphi\right], \tag{23}$$

which for the two amplitude ratios used in the present study reduces to

$$\left(\frac{U}{c}\right)_{s,ak/bk=2.5} = -0.1050-0.10\cdot\sin\varphi, \tag{24a}$$

$$\left(\frac{U}{c}\right)_{s,ak/bk=0.4} = 0.1050-0.10\cdot\sin\varphi, \tag{24b}$$

for antiplectic and symplectic metachronism, respectively.

Now comparing results for the channel (figures 8–13) with that of the sheet, (24a–b), the streaming velocity is largest for the infinite sheet in antiplectic metachronism (see for example the diagonal from (0,0) to (π,π) in figure 9 or figure 11 and compare with (24a)), and largest for the channel in symplectic metachronism, provided there is close spacing of two opposing sheets in the channel (see for example the diagonal from (π,π) to $(2\pi,2\pi)$ in figure 10 and compare with (24b)). It is noted, that for the case of predominantly longitudinal waves (antiplectic metachronism) we have streaming in the negative x–direction of about $U/c\simeq 0.23$ as the spacing between the two sheets equals about 1/4 wavelength, which is allways greater than (24a) (see figure 13, $\varphi_U=\pi/2$). This suggests an additive or a destructive interference of the oscillating motion generated by each sheet when the metachronism appears to have predominantly longitudinal waves, and an additive interference, when the metachronism appears to have predominantly transverse waves.

As spacing extends to infinity, channel cases with the two sheets in phase yields exactly the value of the waving sheets solution (see figure 8 and 9), which is in agreement with asymptotic analysis for the limit $kh \longrightarrow \infty$.

Considering the infinite sheet model (equation (23)) we notice that the steady velocity is quadratic in the nondimensional amplitudes ak and bk. Since these are assumed small, the streaming velocity U is much smaller than the oscillatory velocities associated with the motion of the envelope which are first order in ak and bk (see equation (7)). Thus, an analysis gives

$$\left| \frac{U_{s,max}}{u_{wall,max}} \right| = 0.5 \cdot ak \,. \qquad (25)$$

Clearly, (25) gives a streaming velocity U smaller than the velocities at the envelope. Now, the conclusions from comparing the two dimensional channel with the the two dimensional sheet indicate a greater streaming velocity for the channel than for the sheet It is therefore possible that the streaming velocity might exceed the velocity at the surface envelope for the two dimensional channel. However, there is no proof of this conjecture in the present analysis. Pursuit of this question requires higher order solutions.

From the numerical results of figure 10, it was found that the direction of streaming is always the same as the wave direction of propagation (positive x–direction). Now, examination of (24b) shows that the direction of streaming delivered by each sheet will always be positive, independent of the value of φ. Thus, choosing the lower sheet to give a positive streaming, then the sheet at the upper surface can either have a destructive or a constructive effect. Nevertheless, figure 10 shows an increased streaming in all cases, this in spite of cases where the upper surface has the effective stroke against that of the lower surface.

Mean velocity with pressure gradient: – Including a pressure gradient the net flow U will be coupled though pressure gradient and streaming. Investigating (17) and writing the last two terms of the form $m_0 h = l_0 F_1 + \omega F_2$ and $l_0 = l_0 F_1 + \omega F_2$ (see (14) and (15)), where $F_1 = F_1(a,b,k,h,\varphi)$ and $F_2 = F_2(a,b,k,h,\varphi)$ yields

$$U = C l_0 + l_0 F_1 + \omega F_2 \,, \qquad (26)$$

where C is a constant determined by geometry. Inserting (11) into (26) yields

$$U = \frac{(-dp/dx)}{\mu} \left[C + F_1 \right] + \omega F_2 \,, \qquad (27)$$

μ denotes the dynamic viscosity of the fluid. Rearranging (27) yields the pump characteristic

$$dp/dx = \mu \cdot \left[\frac{\omega \cdot F_2 - U}{C + F_1} \right] . \qquad (28)$$

Now, assuming kinematic and geometric parameters to be constant, (28) shows that the net flow is linear to dp/dx (or to the pressure parameter U_P). So, the linear dependence

in figures 16–18 is not surprising.

For given geometry and kinematics, the shut–off head of this pump (dp/dx for U=0) is proportional to the product of beat frequency and fluid viscosity, $\mu\omega$, and the zero back–pressure flow (U for dp/dx=0) is proportional to the beat frequency ω and independent of viscosity. Clearly, the geometry of this pump is a poor approximation to that of the bands of lateral cilia in *Mytilus edulis*. In view of this, and the fact that the present theory is limited to small amplitudes, it is also not surprising that the pump characteristic of equation (28) does not match that inferred from experiments, Jørgensen et al (1990). The latter suggest shut–off head to be independent of both beat frequency and viscosity μ, and the zero back–pressure flow to be inversely proportional to viscosity.

7. Conclusions

In conclusion, this report has presented a two dimensional channel model for ciliary water propulsion based on the envelope model. The creeping flow equations with boundary conditions (equation (2) and (7)) have been solved by usual perturbation theory which is valid provided the nondimensional amplitudes in the longitudinal and transverse directions are small.

Two cases are considered, that of steady velocity (streaming) produced by oscillatory motions of two opposing flexible surfaces, and that of including a pressure gradient. The latter case appears as a coupled flow problem including pressure gradient and induced streaming.

Results for the net velocity are presented for the two–dimensional channel in comparison with the wave velocity. The ratio of the streaming velocity for the two dimensional channel and that of the single sheet model is discussed. Depending on phase relations and distance between sheets of the channel this ratio illustrates the degree to which streaming is augmented or impeded by the flow interaction.

Specific cases of amplitude ratio ka/kb include that of predominantly longitudinal waves (representative for the lateral cilia of *Mytilus edulis*), that of predominantly transverse waves, and that of zero longitudinal waves (peristaltic pumping) has been considered. The first one indicates antiplectic metachronism in ciliated channels and the second one indicates symplectic metachronism, provided that the effective stroke is in the same direction as the streaming velocity. At close spacing of two opposing sheets, the results indicate additive interference when the metachronism appears to have predominantly transverse waves, and additive or destructive interference when the metachronism appears to have predominantly longitudinal waves. In agreement with

asymptotic analysis for the limit kh $\longrightarrow \infty$, the streaming equals that of a single sheet as the spacing between the sheets becomes large compared to the wavelength of the metachronal waves of cilia motion.

Also, the streaming velocity is relatively insensitive to the phase between waves of opposing sheets. This seems to be an appropriate choice in an evolutionary context in view of the fact that opposing bands of lateral cilia in *Mytilus edulis* have randomly changing phase. These observations are subject to the limitations implicit in the present perturbation analysis. It treats opposing infinite sheets that have small amplitudes, while ciliary systems in bivalves involve opposing narrow bands that have amplitudes of order one or greater.

Including a pressure gradient on the induced channel flow the results has been interpreted and presented as pump characteristics. The results indicate that the most efficient pump is that of close spacing of two opposing sheets and with the two sheets in phase. However, its dependence on viscosity and frequency of cilia motion does not agree with observations on *Mytilus edulis*, suggesting the need for further analysis including finite amplitudes, finite geometry and higher order harmonics in time in order to model the differences in the speeds of the effective and recovery strokes.

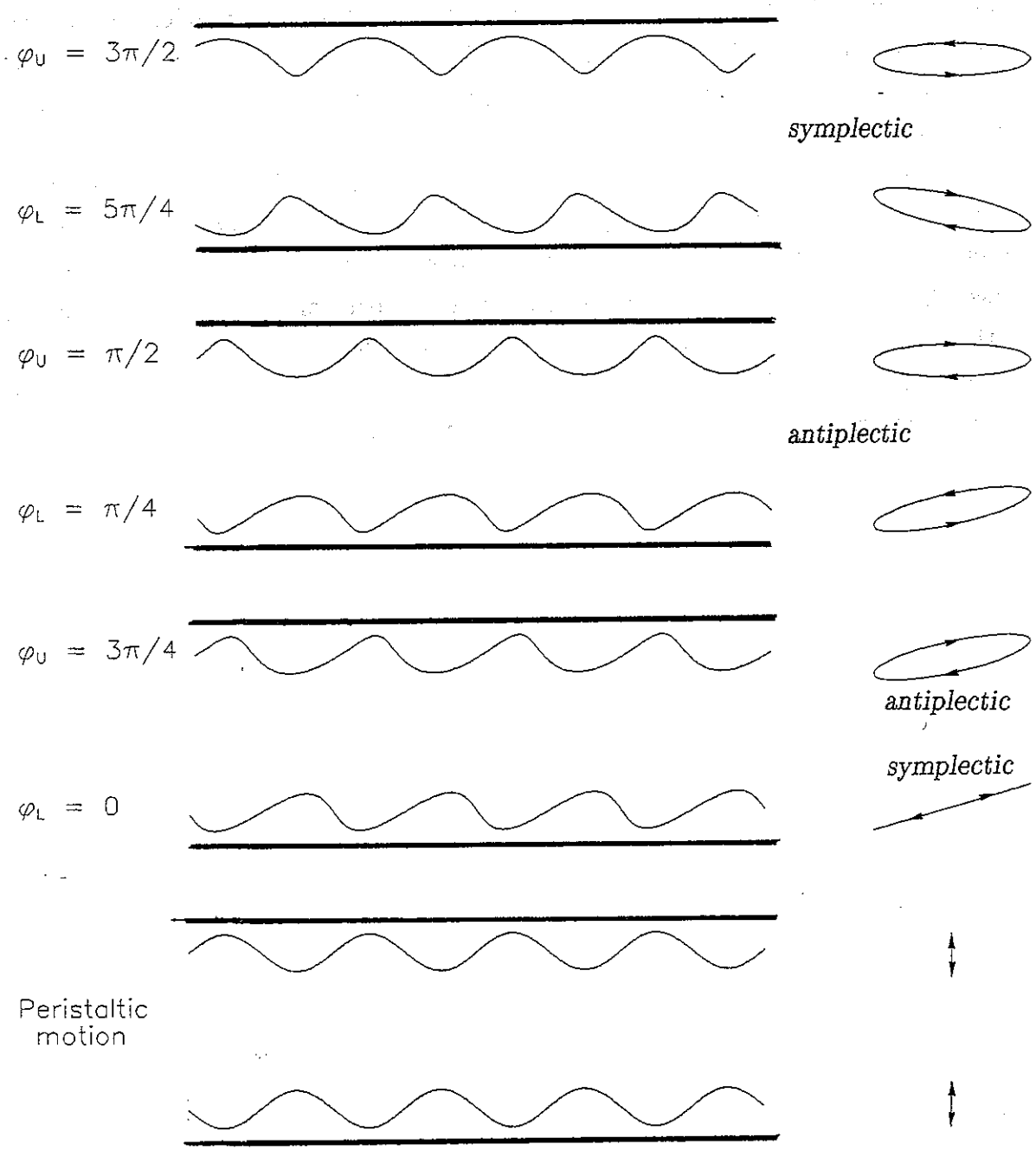

Figure 7. Graphs showing surface envelope shapes, and particle paths for combinations of symplectic–antiplectic waves (symplectic metachronism; $\pi<\varphi<2\pi$, antiplectic metachronism; $0<\varphi<\pi$) and the special case of peristaltic motion.

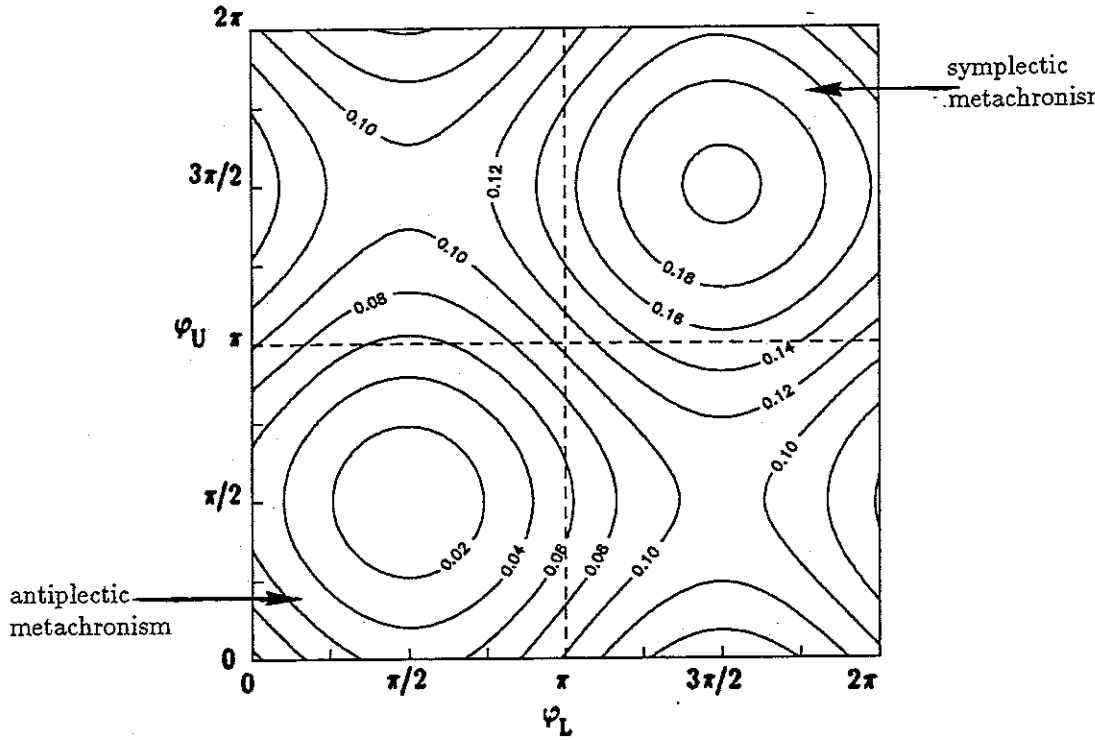

Figure 8. Variation of the dimensionless streaming velocity U/c with phase angles φ_L and φ_U at lower and upper surface, respectively; case of, ka=0.20, kb=0.50 (ka/kb=0.4), c=0.225mm/s, kh=10, P=0.

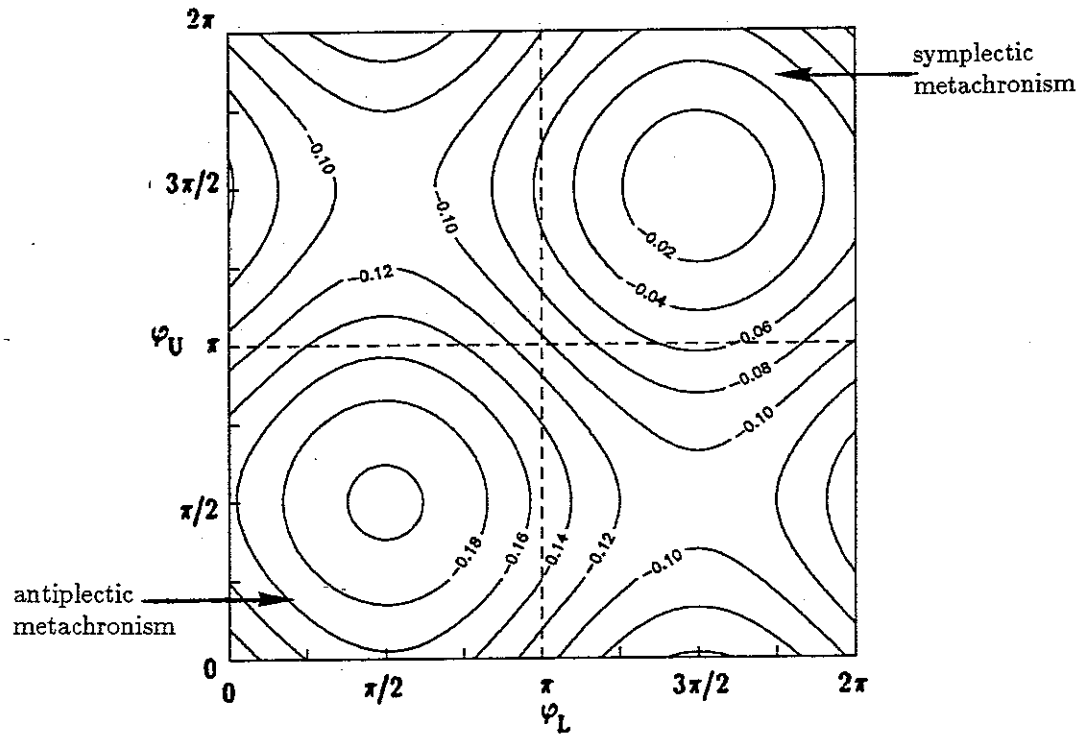

Figure 9. Variation of the dimensionless streaming velocity U/c with phase angles φ_L and φ_U at lower and upper surface, respectively; case of, ka=0.50, kb=0.20 (ka/kb=2.5), c=0.225mm/s, kh=10, P=0.

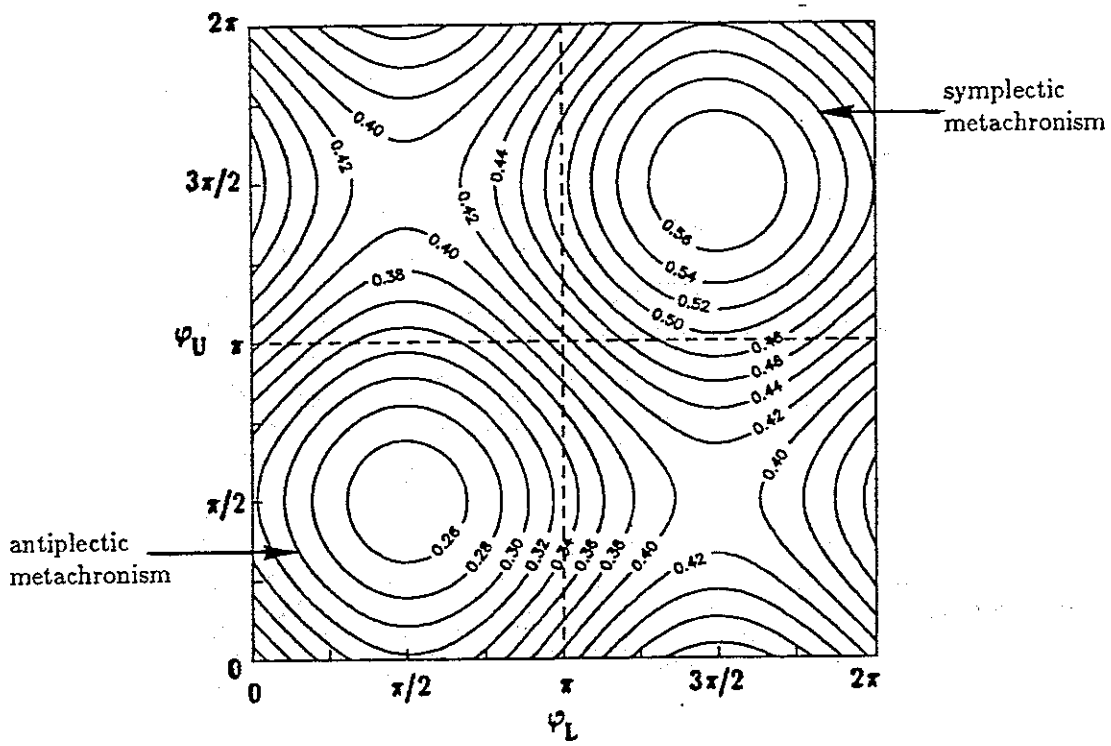

Figure 10. Variation of the dimensionless streaming velocity U/c with phase angles φ_L and φ_U at lower and upper surface, respectively; case of, ka=0.20, kb=0.50 (ka/kb=0.4), c=0.225mm/s, kh=2, P=0.

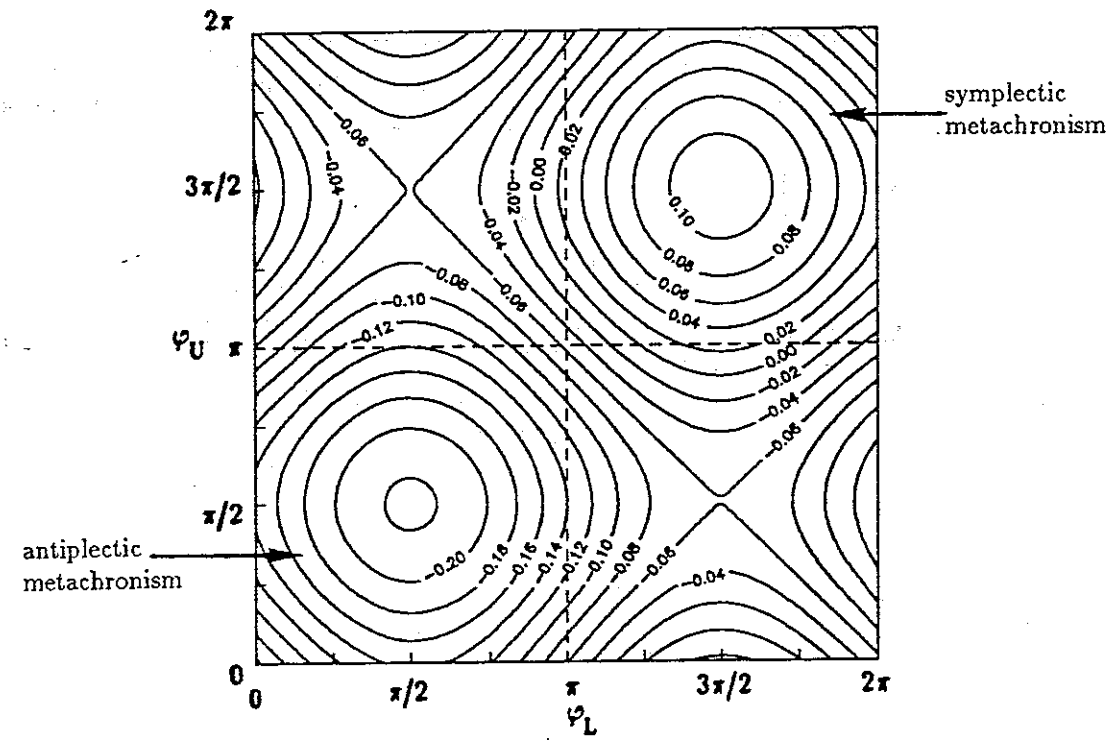

Figure 11. Variation of the dimensionless streaming velocity U/c with phase angles φ_L and φ_U at lower and upper surface, respectively; case of, ka=0.50, kb=0.20 (ka/kb=2.5), c=0.225mm/s, kh=2, P=0.

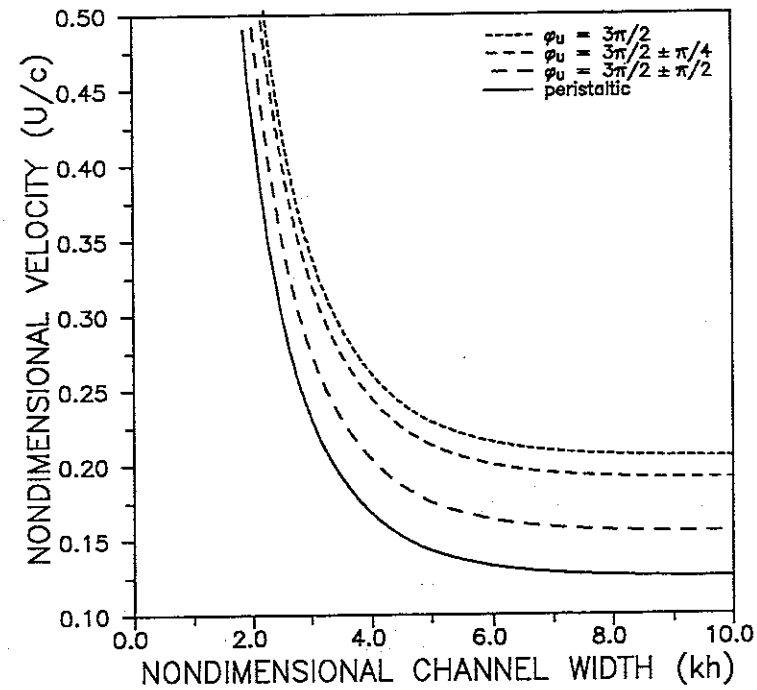

Figure 12. Variation of the dimensionless streaming velocity U/c with the dimensionless channel width (kh) for different phase relations; case of symplectic metachronism ($\varphi_L=3\pi/2$), ka=0.20, kb=0.50 (ka/kb=0.4), c=0.225mm/s, P=0.

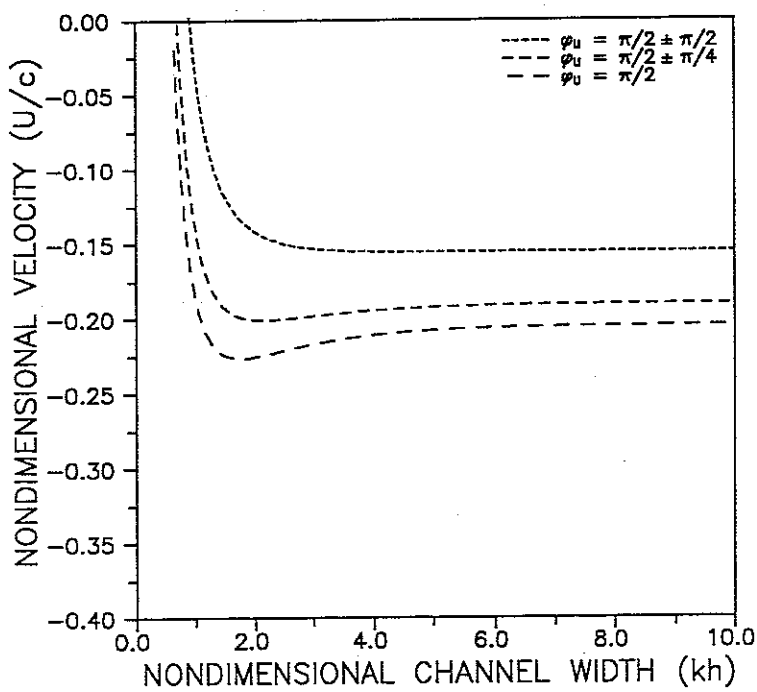

Figure 13. Variation of the dimensionless streaming velocity U/c with the dimensionless channel width (kh) for different phase relations; case of antiplectic metachronism ($\varphi_L=\pi/2$), ka=0.50, kb=0.20 (ka/kb=2.5), c=0.225mm/s, P=0.

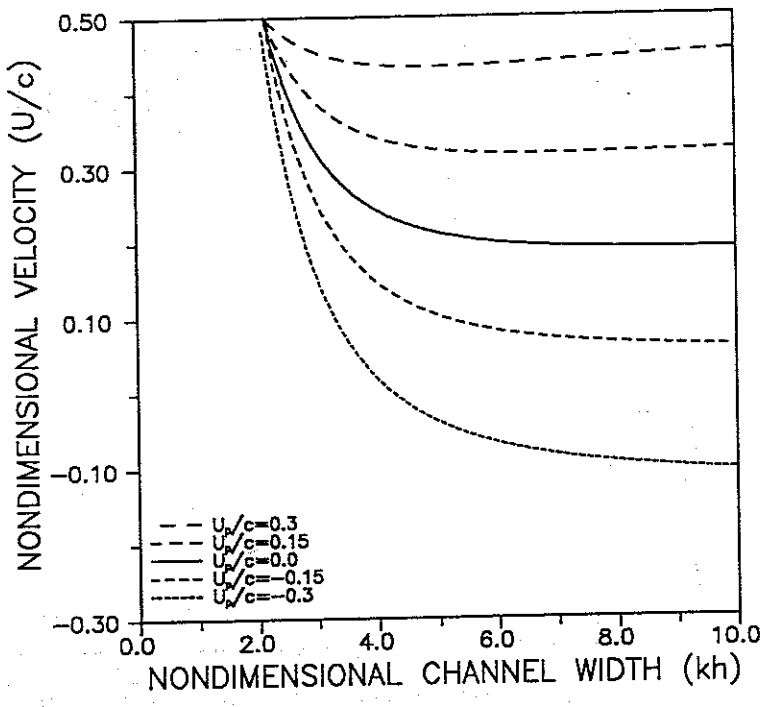

Figure 14. Variation of the mean velocity U/c with channel width (kh) for different pressure parameters; case of symplectic metachronism ($\varphi_L=3\pi/2$, $\varphi_U=5\pi/4$), ka=0.20, kb=0.50 (ka/kb=0.4), c=0.225mm/s.

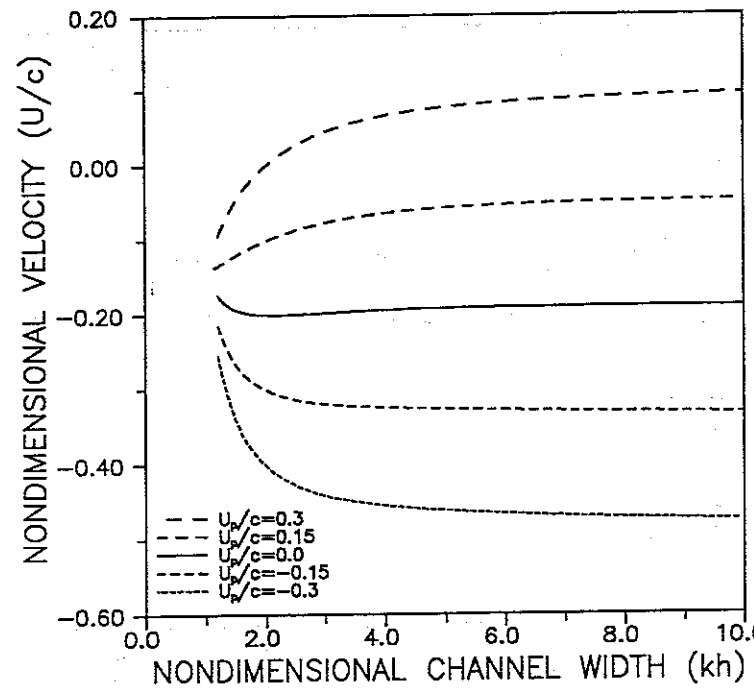

Figure 15. Variation of the mean velocity U/c with channel width (kh) for different pressure parameters; case of antiplectic metachronism ($\varphi_L=\pi/2$, $\varphi_U=\pi/4$), ka=0.50, kb=0.20 (ka/kb=2.5), c=0.225mm/s.

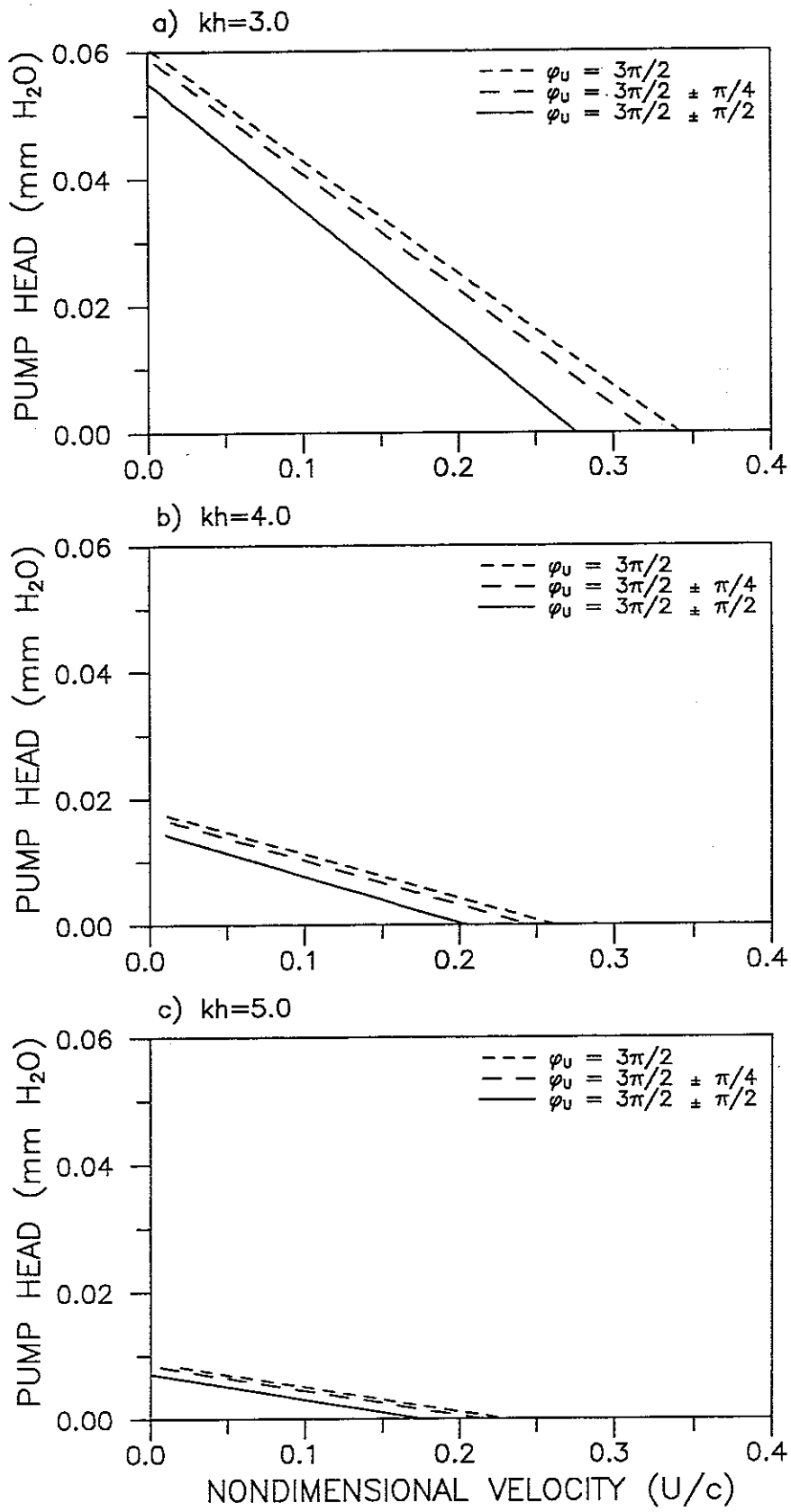

Figure 16a–c. Pump characteristics for different phase relations and distance between the two sheets (kh); case of symplectic metachronism (φ_L=3π/2), ka=0.20, kb=0.50 (ka/kb=0.4), c=0.225mm/s.

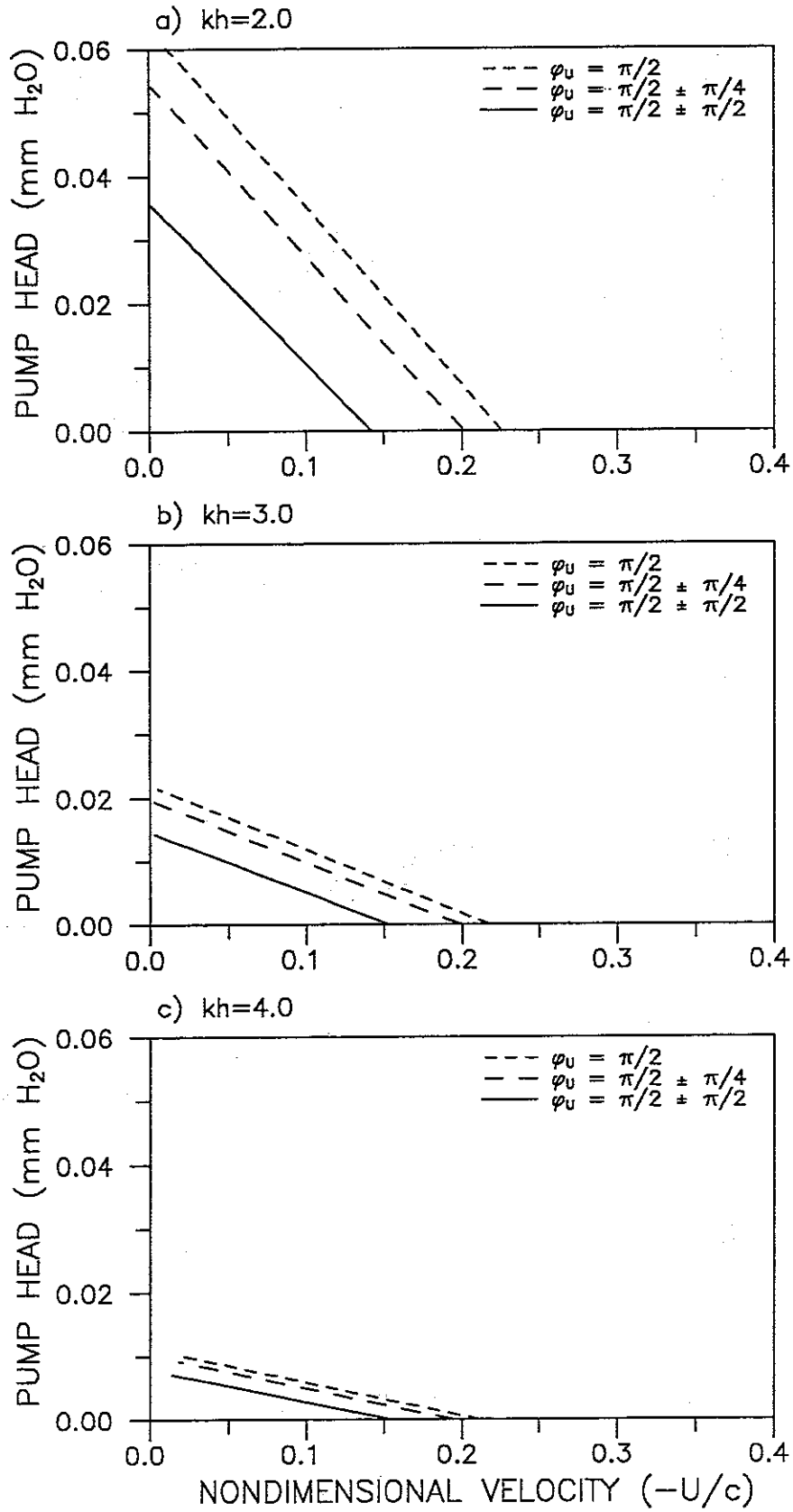

Figure 17a–c. Pump characteristics for different phase relations and distance between the two sheets (kh); case of antiplectic metachronism ($\varphi_L=\pi/2$), ka=0.50, kb=0.20 (ka/kb=2.5), c=0.225mm/s.

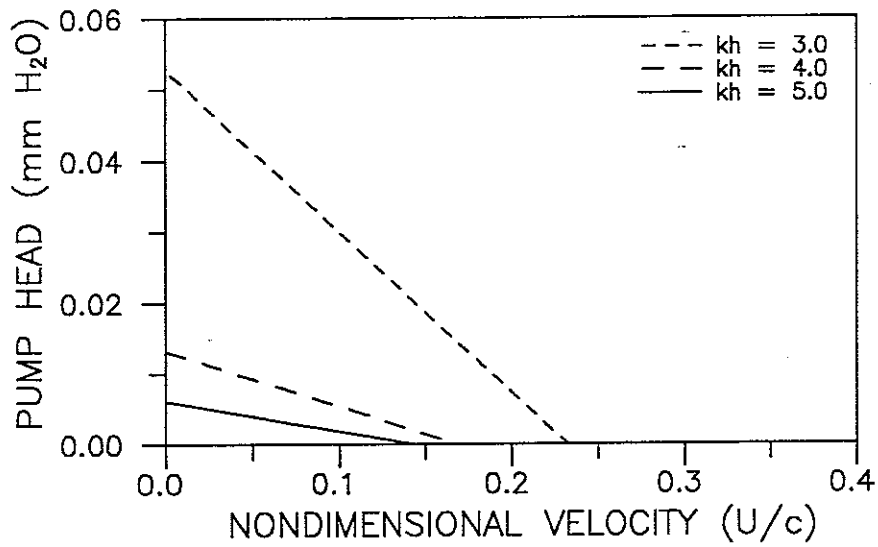

Figure 18. Pump characteristics for different distance between the two sheets (kh); case of peristaltic motion, ka=0.0, kb=0.50,c=0.225mm/s.

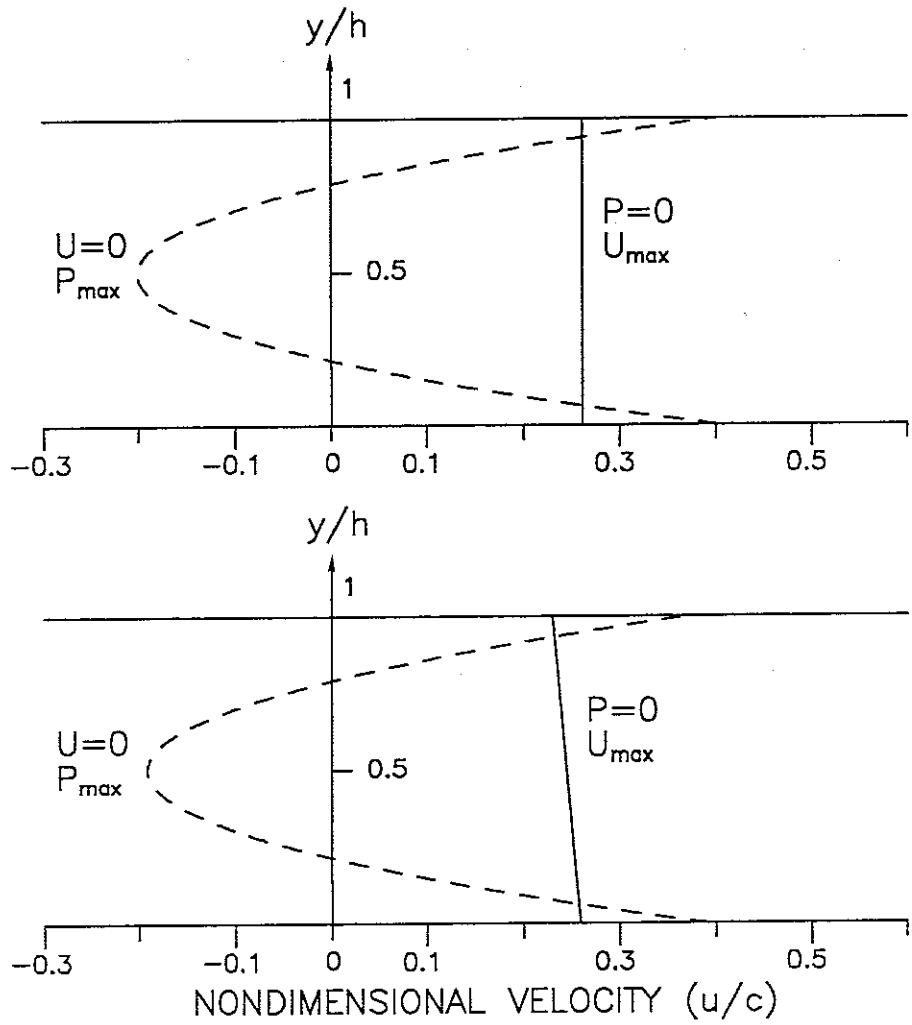

Figure 19. Variation of the time mean velocity $\bar{u}$ with y–coordinate, for U=0 and P=0. Upper part; symplectic metachronism ($\varphi_L=3\pi/2$, $\varphi_U=3\pi/2$). Lower part; ($\varphi_L=3\pi/2$, $\varphi_U=5\pi/4$); Case of, ka=0.2, kb=0.5 (ka/kb=0.4), c=0.225mm/s, kh=4.

Appendix

First order coefficients:

$$a_1 = -f_1 - ka\cdot\sin\varphi_L$$

$$b_1 = \frac{B_1+B_2}{-\tanh^2(kh)\cdot\left[1+(kh)^2\right]+(kh)^2}$$

$$B_1 = ka\cdot\left[\sin\varphi_L\left[-kh\tanh^2(kh)-\tanh(kh)+kh\right]-\sin\varphi_U/\cosh(kh)\left[-\tanh(kh)+kh\right]\right]$$

$$B_2 = kb\cdot\left[\tanh^2(kh)-kh\tanh(kh)/\cosh(kh)\right]$$

$$c_1 = \frac{k^2ah\cdot\left[\cos\varphi_L\left[-kh\tanh^2(kh)+kh\right]+\cos\varphi_U\cdot\tanh(kh)/\cosh(kh)\right]}{-\tanh^2(kh)\cdot\left[1+(kh)^2\right]+(kh)^2}$$

$$d_1 = \frac{ka\left[\cos\varphi_L\left[kh\tanh^2(kh)+\tanh(kh)-kh\right]-\cos\varphi_U\cdot\left[\tanh(kh)-kh\right]/\cosh(kh)\right]}{-\tanh^2(kh)\cdot\left[1+(kh)^2\right]+(kh)^2}$$

$$e_1 = kb$$

$$f_1 = \frac{F_1+F_2}{-\tanh^2(kh)\cdot\left[1+(kh)^2\right]+(kh)^2}$$

$$F_1 = ka\cdot\left[\sin\varphi_L\cdot\tanh^2(kh)+\sin\varphi_U/\cosh(kh)\left[kh\tanh(kh)\right]\right]$$

$$F_2 = kb\cdot\left[kh\cdot\tanh^2(kh)-\tanh(kh)\left[1+1/\cosh(kh)\right]-kh\left[1+1/\cosh(kh)\right]\right]$$

$$g_1 = 0$$

$$h_1 = ka\cdot\cos\varphi_L - c_1$$

Recalculated first order coefficients arising from second order coupling. The new coefficients a_1, b_1, f_1 are solved by Gauss elimination of the linear system $Ax = y$, where

$$A = \begin{bmatrix} a_{11} & a_{12} & a_{13} \\ a_{21} & a_{22} & a_{23} \\ a_{31} & a_{32} & a_{33} \end{bmatrix}, \qquad x = \begin{bmatrix} a_1 \\ b_1 \\ f_1 \end{bmatrix}, \qquad y = \begin{bmatrix} y_1 \\ y_2 \\ y_3 \end{bmatrix},$$

$$a_{11} = \frac{k}{\omega}\cdot\left[k + \frac{k}{\cosh(kh)}\right]$$

$$a_{12} = \frac{k}{\omega}\cdot\left[kh + \tanh(kh)\right]$$

$$a_{13} = \frac{k}{\omega}\cdot\left[1 + kh\cdot\tanh(kh) + 1/\cosh(kh)\right]$$

$$a_{21} = \frac{k^2}{\omega}\cdot\tanh(kh)$$

$$a_{22} = \frac{k}{\omega}\cdot kh\cdot\tanh(kh)$$

$$a_{23} = \frac{k}{\omega}\cdot kh$$

$$a_{31} = \frac{1}{2}\cdot\frac{k}{\omega}\cdot ka\cdot\left[\frac{k\sin\varphi_L}{\cosh(kh)} - k\sin\varphi_U\right] - \frac{1}{2}k^2 b\cdot\tanh(kh) - \frac{kh}{b\cdot\cosh(kh)}$$

$$a_{32} = -\frac{1}{2}\cdot\frac{k}{\omega}\cdot ka\cdot\left[\sin\varphi_U(\tanh(kh)+kh)\right] - \frac{1}{2}kbkh\cdot\tanh(kh) - kb\left[1+\frac{1}{\cosh(kh)}\right]$$

$$a_{33} = \frac{1}{2}\cdot\frac{k}{\omega}\cdot ka\cdot\left[\frac{\sin\varphi_L}{\cosh(kh)} - \sin\varphi_U(1+kh\tanh(kh))\right] - \frac{1}{2}kb\cdot\left[2\tanh(kh)+kh\right] - \frac{kh}{kb\cosh(kh)}$$

$$y_1 = -kb\cdot\tanh(kh) - \frac{ka}{\cosh(kh)}\left[\sin\varphi_L + \sin\varphi_U\right] + \frac{6l_0 khb}{\omega\cdot\cosh(kh)}$$

$$y_2 = -kb\cdot\left[\frac{1}{\cosh(kh)} + 1\right]$$

$$y_3 = \frac{1}{2}ka\left[\left[\frac{(c_1+h_1)\cos\varphi_L}{\cosh(kh)} - \cos\varphi_U\left[c_1 + khd_1 + h_1 + (d_1 + khh_1)\tanh(kh)\right]\right] + \right.$$

$$\frac{1}{2}(kb)^2\left[1+\frac{1}{\cosh(kh)}\right] + \frac{1}{2}kakbsin\varphi_U\tanh(kh) - \frac{akh}{b\cosh(kh)}\sin\varphi_L - \frac{3l_0 kh^2}{\omega\cdot\cosh(kh)}$$

Nomenclature

Latin symbols

a	longitudinal amplitude	(m)
a_n	velocity coefficient (see eq.(10))	(–)
b	transverse amplitude	(m)
b_n	velocity coefficient (see eq.(10))	(–)
c	wave velocity ($c=\omega/k$)	(m/s)
C	geometric constant	(m^2)
c_n	velocity coefficient (see eq.(10))	(–)
d	base separation between neighboring cilia	(m)
d_n	velocity coefficient (see eq.(10))	(–)
e_n	velocity coefficient (see eq.(10))	(–)
f	frequency ($f=\omega/2\pi$)	(1/s)
f_n	velocity coefficient (see eq.(10))	(–)
F_1	function ($F_1=F_1(a,b,k,h,\varphi)$)	(m^2)
F_2	function ($F_2=F_2(a,b,k,h,\varphi)$)	(m^2)
g_n	velocity coefficient (see eq.(10))	(–)
h	channel width	(m)
h_n	velocity coefficient (see eq.(10))	(–)
k	wave number ($k=2\pi/\lambda$)	(1/m)
l_0	pressure coefficient (see eq.(11))	(1/ms)
L	cilium length	(m)
m_0	coefficient (see eq.(10))	(1/s)
p	pressure	(Pa)
P	pressure drop per wavelength	(Pa/m)
Re	Reynolds number ($Re=hU/\nu$)	(–)
$Re_{f,\lambda}$	oscillatory Reynolds number ($Re_{f,\lambda}=\omega/k^2\nu$)	(–)
t	time	(s)
u	velocity component in x–direction	(m/s)
$\bar{u}$	time mean velocity	(m/s)
U	mean velocity in the channel	(m/s)
U_P	mean Poiseuille velocity ($U_P=Ph^2/12\mu$)	(m/s)
U_s	mean velocity of single sheet	(m/s)
u_s	envelope surface velocity in x–direction	(m/s)
v	velocity component in y–direction	(m/s)
v_s	envelope surface velocity in y–direction	(m/s)
x	x–coordinate	(m)
y	y–coordinate	(m)
X_L	x–coordinate of lower surface envelope	(m)
X_U	x–coordinate of upper surface envelope	(m)
Y_L	y–coordinate of lower surface envelope	(m)
Y_U	y–coordinate of upper surface envelope	(m)
z	stationary frame parameter	(–)

Greek symbols

λ	wavelength ($\lambda=2\pi/k$)	(m)
φ	phase angle	(radian)
φ_L	phase angle at lower surface	(radian)
φ_U	phase angle at upper surface	(radian)
ψ	stream function (see eq.(3))	(m^2/s)
ω	radian frequency ($\omega=2\pi f$)	(radian/s)
μ	dynamic viscosity	(Pa·s)
ν	kinematic viscosity	(m^2/s)

References

Blake,J.R.
A spherical envelope approach to ciliary propulsion.
Journal of Fluid Mechanics, vol.46, p.199–208, 1971a

Blake,J.R.
Infinite models for ciliary propulsion.
Journal of Fluid Mechanics, vol.49, p.209–222, 1971b

Blake,J.R.
A model for the micro–structure in ciliated organisms
Journal of Fluid Mechanics, vol.55, p.1–23, 1972

Blake,J.R. & Sleigh,M.A.
Hydromechanical aspects of ciliary propulsion.
Swimming and Flying in Nature (eds. T.Y.Wu, C.J.Brokaw & C Brennen)
Plenum Press, New york, vol.1, p.185–209, 1975

Brennen,C.
An oscillating–boundary–layer theory for ciliary propulsion.
Journal of Fluid Mechanics, vol.65, p.799–824, 1974

Brennen,C. & Winet,H.
Fluid mechanics of propulsion by cilia and flagella.
Annual Review of Fluid Mechanics p.339–398, 1977

Burns,J. & Parkes,T.
Peristaltic motion.
Journal of Fluid Mechanics, vol.29, p.731–741, 1967

Jørgensen,C.B., Larsen,P.S., Riisgård,H.U.
Effect of temparature on the mussel pump
Marine Ecology Progress Series, vol.64, p.89–97, 1990

Knight–Jones,E.W.
Relations between metachronism and the direction of cilia beat in Metazoa.
Quarterly Journal of Microscopical Science, vol.95, p.503–521, 1954

Liron,N. & Mochan,S.
The discrete–cilia approach to propulsion of ciliated microorganisms.
Journal of Fluid Mechanics, vol.75, p.593–607, 1976a

Liron,N.
Fluid transport by cilia between parallel plates.
Journal of Fluid Mechanics, vol.86, p.705–726, 1978

Reynolds,A.J.
The swimming of minute organisms.
Journal of Fluid Mechanics, vol.23, p.241–260, 1965

Taylor,G.I.
Analysis of the swimming of microscopic organisms.
Proceedings of Royal Society, London, vol.A 209, p.447–461, 1951

Tuck,E.O.
A note on a swimming problem.
Journal of Fluid Mechanics, vol.31, p.305–308, 1968

Report 2

NUMERICAL SIMULATION OF WATER TRANSPORT BY CILIA SYSTEMS

Niels Finderup Nielsen.

Table of contents

NUMERICAL SIMULATION OF WATER TRANSPORT BY CILIA SYSTEMS

Niels Finderup Nielsen.

Abstract

Water transport generated by a periodic oscillating "interior boundary" which represents cilia movement, is presented. Numerical solutions of the full unsteady as well as the steady form of Navier–Stokes equations are computed. Three cases of results are considered, that of oscillating flow inside a square cavity, that of streaming velocity of quasi–steady periodic solutions, and that of flow separation of steady solutions at low Reynolds numbers. The results indicate that the unsteady term in the Navier–Stokes equations may be neglected for a rotational Reynolds number ($Re_r = \ell^2\omega/\nu$) less than about order unity and that the convective term (nonlinear term) may influence the flow system when the translational Reynolds number ($Re_t = \ell U/\nu$) is greater than about 0.05. Of much interest in problems of the present type is the streaming velocity. This component of the flow is set up through the nonlinearity of the problem which in this study may be a result of purely oscillating cilia motion or a combination of cilia motion and streaming from the nonlinear terms of the governing equations. Results include comparison with experimental investigations of the blue mussel, and a more general discussion of recirculating flows as steady solutions at low Reynolds numbers.

1. Introduction

Cilia are hairlike organelles that are found on the surface of organisms and the basic function of the cilia is to move air, water and in some cases mucous. The typical beat form includes the effective stroke in which the cilia move rapidly towards one side, followed by the recovery stroke in which they move more slowly back in the other direction in a bend position (see figure 1). In this "rowing type" beat each cilium has a regular beat pattern consisting of the effective stroke and the recovery stroke. However, cilia usually occur in large numbers of the cell surface and often the cilia form an isolated clump or band. If the group of cilia beat asynchronously, so that

adjacent cilia are slightly out of phase, the movement gives rise to metachronal waves (out of phase waves).

Of special interest in cilia motion is the steady velocity component which is a result of the above described cycle of cilia activity which produces a resultant movement of water (streaming) in the direction of the effective stroke. This steady streaming will in general appear in oscillatory flows due to the nonlinearity of the problem. This may be the nonlinearity of the governing equations (Navier–stokes equations) or the nonlinearity of the boundary conditions.

The structure and the functioning of cilia systems of especially the blue mussel is well known (see Aiello & Sleigh 1972, Owen 1974, and Jørgensen 1975 for further details). The lateral cilia bands of the blue mussel, which produces the main flow and thus constitute the mussel pump, is a complicated three dimensional beat and the streaming velocity is perpendicular to the direction of the metachronal wave mentioned above (see report 3 for further details about the blue mussel).

Water transport by cilia systems has been of much interest in many years, but so far only analytical solutions of the Stokes equation (inertia terms neglected) has been made. Considering the relevant parameters for cilia systems as cilium length L (~10–20μm), beat frequency f (~10–30Hz), and velocity amplitude U (~10^{-3}m/s), clearly, the Stokes approximation is valid due to a Reynolds number of order 10^{-2} (see section 2). But considering a flow system outside the cilia sublayer as for example a channel in which cilia transport water, the length scale may be several times the cilia length and both the unsteady term and the convective term in the Navier–Stokes equations may influence the flow system.

Not much work has been done in solving the time dependent and the quasi–steady periodic Navier–Stokes equations for low non–zero Reynolds number flows involving oscillatory systems. One is the investigation of flow inside a square cavity (Re=0–600), generated by a uniform oscillatory motion of the upper cavity wall (Duck 1982). Another is oscillatory flow over a simi–infinite flat plate (Re=0–50, Duck 1988).

In the present study we introduce a numerical model for synchronous cilia movement (oscillatory motion in the interior of the calculation domain). We consider two–dimensional unsteady and quasi–steady periodic low Reynolds number flows with special attention to water transport by cilia systems. Furthermore, we investigate recirculating flows as steady solutions at low Reynolds numbers. The results are represented with use of representative values of the lateral cilia bands of the blue mussel. Some results are compared with experimental investigations for evaluation of the cilia model. In spite of the two–dimensional model and a relative simple cilia modeling it is expected that the present analysis will give important

information of theoretical modeling of water transport by cilia systems and flow separation at low Reynolds numbers. The advantage of the numerical approach is easy modeling of finite amplitudes and different speeds in effective and recovery strokes. These features could not be treated in the envelope model (see report 1).

2. Formulation of the problem

Considering two–dimensional, incompressible, and laminar flow the unsteady form of the conservation laws are described by the Navier–Stokes equations

$$\rho\left(\frac{\partial \mathbf{v}}{\partial t} + \mathbf{v}\cdot\nabla\mathbf{v}\right) = -\nabla p + \mu\nabla^2\mathbf{v} + \mathbf{s}_v \,, \tag{1}$$

and by continuity

$$\nabla\cdot\mathbf{v} = 0 \,, \tag{2}$$

where ρ is the density, ∇ the nabla (del) operator, $\mathbf{v}=(u,v)$ the velocity vector, p the thermodynamic pressure, $\mu=\rho\nu$ is the dynamic viscosity, ν denoting the kinematic viscosity, and $\mathbf{s}_v$ the source term.

We now define the following dimensionless quantities

$$\begin{gathered} \hat{t} \equiv \omega t \quad , \quad \hat{\nabla} \equiv l\nabla \quad , \quad \hat{\mathbf{v}} \equiv \frac{\mathbf{v}}{U} \quad , \quad \hat{p} \equiv (p-p_\infty) l/\mu U \,, \\ \hat{\mathbf{s}}_v \equiv \frac{\mathbf{s}_v l^2}{\mu U} \quad , \quad Re_r \equiv \frac{l^2\omega}{\nu} \quad , \quad Re_t \equiv \frac{lU}{\nu} \,, \end{gathered} \tag{3}$$

where ω ($\omega=2\pi f$) denotes a typical angular velocity, l and U typical length and velocity scales, respectively, p_∞ the constant pressure at infinity, and Re_r and Re_t the rotational (oscillatory) and translational Reynolds numbers, respectively. Inserting (3) in (1) and (2) yields the nondimensional form

$$Re_r\left(\frac{\partial \hat{\mathbf{v}}}{\partial \hat{t}}\right) + Re_t(\hat{\mathbf{v}}\cdot\hat{\nabla}\hat{\mathbf{v}}) = -\hat{\nabla}\hat{p} + \hat{\nabla}^2\hat{\mathbf{v}} + \hat{\mathbf{s}}_v \,, \tag{4}$$

$$\hat{\nabla}\cdot\hat{\mathbf{v}} = 0 \,. \tag{5}$$

In the Navier–Stokes equations (4) the inertia terms comprise the unsteady term and

the convective term which belong to the rotational and translational Reynolds numbers, respectively.

The numerical problem consists of solving (4) and (5), with appropriate boundary conditions and relevant values of Re_r and Re_t.

3. Numerical model

In order to solve the differential equations of the previous section it is necessary to discretize the equations. Discretization of the differential equations and the boundary conditions of a continuous domain yields a finite set of algebraic equations to be solved in a domain of discrete points (grid points).

Here, we use a finite volume discretization approach in which the calculation domain is divided into a number of non–overlapping control volumes such that there is one control volume surrounding each grid point. The differential equations are then integrated over the control volumes, one of which is sketched in figure 2, and we obtain the discretized equations containing the values of the dependent variables (P of figure 2) for a group of grid points. The main feature of the finite volume discretization is that the integral balance of momentum is satisfied over any group of control volumes and, of course, over the whole calculation domain. Hence, the integral balance is not only fulfilled when the number of grid points become large but also on a coarse grid (Patankar 1980). This property is fully exploited when the governing equations are written in conservative form.

In the discrete form of the governing equations there appears values of the dependent variables at the control volume surfaces. These values have to be expressed in terms of neighbor grid point values (interpolation) in order to achieve algebraic equations. This is effected by differencing schemes. The choice of difference scheme depends on the nature of the physical problem. Here, the hybrid scheme is used (see Patankar 1980). This scheme employs central differences for vanishing cell Peclet numbers (the cell Peclet number is defined as the ratio of convective fluxes to diffusive fluxes, $Pe_c=u\Delta x/\nu$) and upwinding schemes for large Peclet numbers ($Pe_c>2$). In either case the discretization of (4), for the two–dimensional case considered here, is given by

$$\left[a_P+\frac{\rho\Delta x\Delta y}{\Delta t}\right]v_{i,P}^{n+1} = a_E v_{i,E}^{n+1} + a_W v_{i,W}^{n+1} + a_N v_{i,N}^{n+1} + a_S v_{i,S}^{n+1} + \tag{6}$$

$$s_c + \frac{\rho\Delta x\Delta y}{\Delta t}v_{i,P}^{n} \quad , \quad a_P=a_E+a_W+a_N+a_S \, ,$$

where a fully implicit scheme with an implicit Euler time step is used (see Patankar 1980 for further details). In (6) $v_{i,P}$ denotes the velocity component in the central point P, $v_{i,E}$, $v_{i,W}$, etc. the velocity components in the neighbor points to the central point (West, East, North, South, see figure 2), a_P and a_E, a_W, etc. the coefficients associated with the central and the neighbor velocities, respectively, s_c the source term including the pressure, Δx and Δy the grid spacing in the x– and y–directions, respectively, and Δt the time step. The superscripts n and n+1 are taken as "old" values (i.e. the values at the previous time step) and "new" values, respectively.

In equation (6) above, the velocity, the pressure, and other variables could be located at the main node, P, of the control volume. However, locating these variables at the main node a zig–zag structure may arise. A pressure field where every second pressure node has the same value different from the other values will satisfy the momentum equations as well as an uniform pressure field would do. A zig–zag pressure field arising during the iterative solution will persists until convergence (Patankar 1980). One way to get rid of the zig–zag fields is to use a staggered grid. In the staggered grid, which we will use here, the u velocities are stored at the center of the "e" and "w" faces and v velocities are stored at the center of the "n" and "s" faces. Only the velocities are staggered from the main grid point whereas all other variables as pressure, density, and viscosity are stored at the main grid point. Hence, in place of (6) the momentum equations, for example u_e and v_n, are given by

$$\left[a_e+\frac{\rho\Delta x\Delta y}{\Delta t}\right]u_e^{n+1} = \Sigma a_{nb}u_{nb}^{n+1} + (p_P-p_E)A_e + s_c + \frac{\rho\Delta x\Delta y}{\Delta t}u_e^n \quad , \quad a_e=\Sigma a_{nb} \, , \tag{7a}$$

$$\left[a_n+\frac{\rho\Delta x\Delta y}{\Delta t}\right]v_n^{n+1} = \Sigma a_{nb}v_{nb}^{n+1} + (p_P-p_N)A_n + s_c + \frac{\rho\Delta x\Delta y}{\Delta t}v_n^n \quad , \quad a_n=\Sigma a_{nb} \, , \tag{7b}$$

where the summation Σa_{nb} denotes the neighbor values linking to the center value P and A_e the area of the e–face of the main control volume.

The discretized form of the continuity equation (5), written for the P–centered control volume, is given by

$$A_w(u_e-u_w) + A_s(v_n-v_s) = 0 \, . \tag{8}$$

4. Solution procedure

In this section we describe the solution procedure of the discretized Navier–Stokes equations and the equation of continuity. The solution procedure includes velocity–pressure coupling, boundary conditions, solvers and periodic boundary conditions, numerical treatment of ciliary movement, and finally time stepping procedure and stop criterion.

4.1 Velocity–pressure coupling

As indicated by the equations (7) and (8) the pressure does not have its own governing equation, but has to be determined through the equation of continuity. Only if the correct pressure field is substituted into the momentum equations (7), the resulting velocity field will satisfy the equation of continuity (8). Several methods has been developed to determine the velocity pressure coupling (see for example Gervang 1988). Here, we only consider the PISO algorithm (Pressure Implicit with Splitting of Operators, Issa 1985). The PISO algorithm is a predictor–corrector scheme including one predictor level and two corrector levels. The algorithm was developed to handle unsteady flows with no iterations in each time step and no under relaxation to suppress effects of nonlinearities. It is noted, that other algorithms as for example SIMPLE or SIMPLER require several iterations in each time step and under relaxation on both the pressure and the velocity field. Clearly, the PISO algorithm needs under relaxation, and this is also obtained through the time step Δt. But what about steady state solutions ? – It can be shown that there is a close relationship between under relaxation in steady state iteration problems and relaxation through the time step in time dependent problems (see Issa 1986 for further details). In conclusion, it is noted that in unsteady calculations the PISO algorithm needs no under relaxation and no global iterations in each time step. In steady state calculations no under relaxation is needed when updating the pressure field, but when updating the velocity field under relaxation is necessary. However, in the steady state version of PISO under relaxation as high as 0.90 may be used. In the present study the PISO algorithm is used in both the steady state version and the time marching version.

4.2 Boundary conditions

So far only the governing equations has been discussed. In this section a number of typical boundary conditions will be considered, rigid impermeable wall, inlet, outlet,

and finally pressure boundary conditions. Further, due to the staggered grid location the boundary condition schemes are outlined for grid points (nodes) lying on the physical boundary and outside the physical boundary.

Rigid, impermeable wall, velocity node <u>on</u> the wall. As the velocity node is placed on the wall and we assume no slip the velocity, say u_N at a north boundary (see figure 3a) equals zero. The momentum equation (6) then become

$$\left[a_P+\frac{\rho\Delta x\Delta y}{\Delta t}\right]u_P^{n+1} = a_E u_E^{n+1} + a_W u_W^{n+1} + 0 + a_S u_S^{n+1} + s_c + \frac{\rho\Delta x\Delta y}{\Delta t}u_P^n \,. \tag{9}$$

The no slip condition is therefore obtained by adjusting the usual coefficients according to the scheme

$$a_P=a_P \quad , \quad a_N=0 \,. \tag{10}$$

Rigid, impermeable wall, velocity node <u>outside</u> the wall. Here, there is no velocity node on the wall itself and a "ghost" point is considered (see figure 3b). Satisfying the no slip condition on the physical boundary we obtain $u_N=-u_P$, and the momentum equation become

$$\left[a_P+\frac{\rho\Delta x\Delta y}{\Delta t}\right]u_P^{n+1} = a_E u_E^{n+1} + a_W u_W^{n+1} + a_N(-u_P^{n+1}) + a_S u_S^{n+1} + s_c + \frac{\rho\Delta x\Delta y}{\Delta t}u_P^n \,, \tag{11}$$

implying the adjustment

$$a_P=a_P+a_N \quad , \quad a_N=0 \,. \tag{12}$$

It is noted, that similar schemes can be obtained for the case of a permeable wall.

Inlet, velocity node <u>on</u> the inlet boundary. At inlet nodes velocities are assumed to be known. The boundary condition, say $u_W=u_{in}$, is satisfied at the physical boundary, yielding a equation similar to (6). Thus, we only need to specify the known velocity u_{in} and no further modification is necessary.

Inlet, velocity node <u>outside</u> the inlet boundary. Here the grid arrangement is similar to that of figure 3b. The boundary condition on the physical boundary is

$u_{in}=(u_P+u_N)/2$ yielding $u_N=2u_{in}-u_P$ and the momentum equation (6) become

$$\left[a_P+\frac{\rho\Delta x\Delta y}{\Delta t}\right]u_P^{n+1} = a_E u_E^{n+1} + a_W(2u_{in}-u_P^{n+1}) + a_N u_N^{n+1} + a_S u_S^{n+1} + s_c + \frac{\rho\Delta x\Delta y}{\Delta t}u_P^n \,, \tag{13}$$

which implies adjustment according to the scheme

$$a_P=a_P+a_N \quad , \quad s_c=s_c+2a_W u_{in} \,. \tag{14}$$

It is noted, that the two inlet schemes outlined above, of course, also applies to the case of a specified velocity on a boundary.

Outlet. In order to assure global conservation of mass flow the integrated flux across all outlet cells is calculated. All outlet cell velocities are then normalized so that the net inlet flux equals net outlet flux. This condition equals the condition of zero velocity gradient, say $u_E=u_P$, and (6) becomes

$$\left[a_P+\frac{\rho\Delta x\Delta y}{\Delta t}\right]u_P^{n+1} = a_E u_P^{n+1} + a_W u_W^{n+1} + a_N u_N^{n+1} + a_S u_S^{n+1} + s_c + \frac{\rho\Delta x\Delta y}{\Delta t}u_P^n \,, \tag{15}$$

implying the adjustment

$$a_P=a_P-a_E \quad , \quad a_E=0 \,. \tag{16}$$

It is noted, that this outlet condition can only be used if the flow is relatively well developed at the outlet.

Pressure boundary conditions. The pressure correction equation can be obtained through the equation of continuity and takes the form (see Patankar 1980)

$$a_P P'_P = a_E P'_E + a_W P'_W + a_N P'_N + a_S P'_S + s_c \,, \qquad a_P=a_W+a_E+a_N+a_S \,, \tag{17}$$

where the source term s_c represents the mass defect which is equal to zero if continuity is satisfied and the pressure correction $P'=P-P^*$, P^* denoting a guessed pressure field.

Given normal velocity at the boundary. In the present study the grid is designed such that the boundary always coincides with a control volume face where a normal velocity is given (u or v–velocity). In the derivation of the pressure correction (17) this has the effect of setting the pressure correction, say P'_N (or a_N) of a north boundary, equal to zero. Thus the pressure coefficients are adjusted according to

$$a_P = a_P \quad , \quad a_N = 0 \, . \tag{18}$$

The alternative approach of a given pressure at the boundary will not be consider here (see for example Patankar 1980).

4.3. Solvers and periodic boundary conditions

Solvers. Before we discuss the solution scheme for periodic boundary conditions, the solvers for the discretized algebraic equations will be considered. Among many solvers, such as Jacobi, Gauss–Seidel, or successive over relaxation (SOR) point or block iterative methods, we here use the line–iteration procedure and the alternating direction implicit procedure (ADI, Peaceman & Rachford 1955). In using the two latter procedures on every internal node of the velocity (eq.(7)) and every internal node of the pressure (eq.(17)) we obtain an algebraic system of N equations and N unknowns where N is the total number of internal nodes (one system means one line, for example south–north line of a west–east sweep, of the calculation domain). This set of equations is easily solved by a Tri–Diagonal Matrix Algorithm (TDMA) which takes the form

$$\mathbf{A}\mathbf{x} = \mathbf{b} \, , \tag{19}$$

where $\mathbf{A}$ is a tridiagonal matrix of order N

$$\mathbf{A} = \begin{bmatrix} d_1 & a_1 & \cdots & 0 \\ b_2 & d_2 & a_2 & \cdots & 0 \\ . & & . & . & \\ 0 & & & . & . \\ 0 & & \cdots & & d_N \end{bmatrix} , \tag{20}$$

where d_i is the central point coefficient, a_i and b_i the north and south coefficients, respectively, for an west–east sweep and a_i and b_i is the east and west coefficients, respectively, for an south–north sweep. $\mathbf{x}$ is the dependent variable vector which here is velocity or pressure, and $\mathbf{b}$ is the source vector which include the remaining

coefficients with associated dependent variables.

Periodic boundary conditions. In many real flow situations periodic boundary conditions appears. In the notation of eq. (19) periodic boundary conditions are obtained by setting

$$x_i = x_{i+N} \quad , \quad \text{for all i} \tag{21}$$

which means that the boundaries are linked together. Inserting the condition (21) in (19) the coefficient matrix appears as

$$A = \begin{bmatrix} d_1 & a_1 & \cdots & b_1 \\ b_2 & d_2 & a_2 \cdots & 0 \\ . & & \ddots & \vdots \\ 0 & & \ddots & \vdots \\ a_N & & \cdots & d_N \end{bmatrix} . \tag{22}$$

Hence, the tridiagonal structure of the matrix is destroyed. However, the technique for solving (19) with a coefficient matrix as (22) is straightforward and will not be considered here (see Samarski & Nicolatev 1981).

In the present study we have, for one case of results, periodic boundary conditions and the u– and v–momentum equations (7a) and (7b) will be solved by the technique of Samarski & Nicolatev. But the pressure equation, which is a pressure correction equation, will be solved in the usual manner because the velocity is known and then no information about the pressure correction is needed (see *pressure boundary condition* above).

4.4. Numerical treatment of cilia movement

In this section we consider a model for cilia movement. There will be some special attention to the lateral cilia bands of the blue mussel which, however, easily can be modified to other situations.

First, how should we model cilia movement ? – In a simple configuration cilia movement can be sought of as a beat period T (T=1/f, f denoting the frequency) and an amplitude consisting of the difference in penetration into the fluid in the effective stroke and in the recovery stroke. This amplitude, in the following referred to as penetration amplitude, is defined as

$$A_c = \Delta y_{eff} - \Delta y_{rec} \tag{23}$$

where Δy_{eff} and Δy_{rec} denotes the distance from a specified wall to the cilia tip in the effective stroke and the recovery stroke, respectively.

Taking into account the nature of a numerical model there will be three obvious models to choose between

- specified time dependent velocity on a wall
- specified time dependent velocity in interior of calculation domain
- specified time dependent source in interior of calculation domain

The first model is easily implemented in a numerical model (see section 4.2) and higher order harmonic functions in time in order to model the differences in the speeds of the effective and the recovery strokes may be studied. However, the penetration amplitude defined by (23) will always be zero.

The second model eliminates the limitation of zero penetration amplitude of the first model, but here the coefficient matrix **A** (see (20)) of the pressure correction equation becomes singular.

The third model, which is the model used in the present study, is easily implemented and furthermore satisfies the condition of non–zero penetration amplitude. The specified source for this model (s_v of (1)), which may be placed anywhere in the calculation domain and at different positions at different times, is an external volume force which for a cylinder is given by

$$f_x = C_D d\frac{\rho(u_c-u_f)^2}{2} \quad , \quad f_y = C_D d\frac{\rho(v_c-v_f)^2}{2} , \tag{24}$$

where C_D denotes the drag coefficient, d the diameter of the cylinder (cilia), ρ the fluid density, u_c (and v_c) the velocity of the cilia, and u_f (and v_f) the fluid velocity. At low Reynolds numbers the drag coefficient is given by

$$C_D = C_D'/Re_c , \tag{25}$$

where Re_c is the cilia Reynolds number ($Re_c=d(u_c-u_f)/\nu$, ν denoting the kinematic viscosity). Inserting (25) in (24) yields

$$f_x = C(u_c-u_f) \quad , \quad f_y = C(v_c-v_f) , \tag{26}$$

where $C=C_D'\mu/2$, μ denoting the dynamic viscosity. Inserting (26), say f_x, in the

discretized momentum equation (7a) we obtain

$$\left[a_e+\frac{\rho\Delta x\Delta y}{\Delta t}+C\right]u_e^{n+1} = \Sigma a_{nb}u_{nb}^{n+1} + (p_P-p_E)A_e + Cu_c + \frac{\rho\Delta x\Delta y}{\Delta t}u_e^n \quad , \quad a_e=\Sigma a_{nb} \, , \tag{27}$$

which may be rearranged to

$$u_e^{n+1} = \frac{\Sigma a_{nb}u_{nb}^{n+1} + (P_P-P_E)A_e + \rho\frac{\Delta x\Delta y}{\Delta t}u_e^n}{a_e + \rho\frac{\Delta x\Delta y}{\Delta t} + C} + u_c\left[1-\frac{a_e + \rho\frac{\Delta x\Delta y}{\Delta t}}{a_e + \rho\frac{\Delta x\Delta y}{\Delta t} + C}\right] . \tag{28}$$

Investigating (27) we note that the fluid velocity, u_e, enters the implicit solution algorithm. Investigating the explicit form (28) an asymptotic analysis show that for the limit $C \longrightarrow \infty$ we obtain $u_e=u_c$. The cilia velocity, u_c, is a known kinematic condition. The drag coefficient, C, of (26) – (28) is taken from theoretical results of flow past a circular cylinder (Cheer & Koehl 1987). The drag coefficient is obtained for an isolated cylinder (C_{iso}), for a cylinder with a neighbor 50 μm away ($C_{50\mu m}$), and for a cylinder with a neighbor 0.3 μm away ($C_{0.3\mu m}$). A curve fit of these calculations gives the following expressions

$$C_{iso} = 3.60\cdot 10^{-3}(Re_c)^{-0.873} \, , \tag{29a}$$

$$C_{50\mu m} = 3.53\cdot 10^{-3}(Re_c)^{-0.833} \, , \tag{29b}$$

$$C_{0.3\mu m} = 3.35\cdot 10^{-3}(Re_c)^{-0.823} \, , \tag{29c}$$

where the diameter of the cylinders in all cases is 0.1 μm and $Re_c=d(u_c-u_f^n)/\nu$, u_f^n denoting and "old" fluid velocity (velocity from a previous time step or iteration).

Now, taking special attention to the lateral bands of the blue mussel where the effective stroke occupies one fifth of the beat period and the recovery stroke four fifth period, the cilia velocity, u_c of (26) –(28), is given by

$$u_c(t) = \begin{cases} U_e \sin(5/2\omega t) & , \ 0 \le t < T/5 \\ U_r \sin\left[5/8\omega(t+3T/5)\right] & , \ T/5 \le t \le T \end{cases} , \tag{30}$$

or the continuous Fourier series

$$u_c(t) = \tfrac{1}{2}a_0 + \sum_{n=1}^{\infty} a_n \cos(n\omega t) + b_n \sin(n\omega t) , \tag{31}$$

where the Fourier coefficients a_0, a_n, and b_n are listed in appendix. It is noted, that in a numerical model, which is discrete in nature, equation (30) is sufficient in spite of the discontinuity at t=T/5. The amplitudes U_e and U_r of equation (30) and (31) (see appendix) is the maximum velocity in effective and recovery strokes, respectively. The effective stroke of the lateral band of the blue mussel occupies, as mentioned, one fifth of the beat period, within which the cilium sweeps though an arc of 150^0 (Sleigh & Aiello 1972). Thus, the mean speed in the effective stroke is $U_{m,eff}=(150/360)2\pi L/(T/5) \simeq 13Lf$, where L is the cilium length and f the beat frequency. This yields a maximum velocity in the effective stroke of

$$U_e = (\pi/2)U_{m,eff} . \tag{32}$$

The recovery stroke occupies four fifth of the beat period, and in order to ensure zero time mean velocity during a cilium beat period, which is the result of a cilium following a closed curve, we obtain

$$\tfrac{1}{5}U_e - \tfrac{4}{5}U_r = 0 \implies U_r = \tfrac{1}{4}U_e . \tag{33}$$

This has the effect of making the Fourier coefficient a_0 in (31) equal to zero, as expected.

In conclusion, the present cilia model approximates cilia movement by specified sources which may be placed anywhere in interior of the calculation domain (eq.(26)). The cilia velocity will in the present study be represented by a model of the lateral band of the blue mussel (eq.(30) or (31) and (32),(33)). The drag coefficient of the cilia are represented by theoretical results of flow past circular cylinders (eq.(29)).

4.5. Time stepping procedure and stop criterion

Time dependent solutions. The PISO algorithm (see section 4.1) calculates with great

accuracy the velocity and the pressure corrections within only one global iteration in each time step (Issa 1986). The result of this is a time marching procedure with relaxation obtained through the time step (no under relaxation of velocity and pressure fields). In order to obtain a converged solution on each time step with the PISO algorithm it is necessary to use a small time step and many internal iterations (sweeps) in both the predictor and the corrector step of the pressure correction equation.

In the present study two approaches, which gave same results, were used. In the first approach the time step, Δt, was obtained by a CFL–criterion given by

$$\Delta t = \min_{all\ i,j} \left\{ \frac{\Delta x}{U}, \frac{\Delta y}{V} \right\}, \tag{34}$$

where Δx and Δy denotes the grid spacing in the x– and y–directions and U and V typical velocities in in x– and y–directions. In some cases a time step lower than the CFL–criterion was used in order to obtain convergence. In this approach a converged solution was assumed if the ratio of the total residual in the first sweep to the total residual in sweep number n satisfied

$$\frac{R^0}{R^n} \leq 0.01 , \tag{35}$$

where the total residual is calculated by the 1–norm

$$R = \sum_{1}^{N} |r| , \tag{36}$$

and where the residual at each point, r, is calculated by

$$r = a_P \varphi_P - \Sigma a_{nb} \varphi_{nb} - s_c , \tag{37}$$

where φ denotes the dependent variable (velocity or pressure) and where the unsteady terms are included in a_P and s_c (see eq.(6)).

In the second approach a solution with a time step equal to the CFL–criterion was obtained after one tenth the time period (maximum velocity of (30) or (31)). In this approach the convergence criterion was ten times as high as condition (35), hence

$$\frac{R^0}{R^n} \leq 0.1 . \tag{38}$$

Now, a new solution after one tenth period was obtained with a time step of half the value of the first one. This procedure was maintained until the difference between two successive solutions was lesser than 1 $^0/_{00}$. This was usually obtained after halving the time step 3–4 times. This time step, and the condition (38), was then used from t=0 and throughout the calculations.

In the first approach the condition (35) was obtained after 20–40 sweeps for the momentum equations and after 100–200 sweeps for the pressure correction equation. In the second approach these values were 5–10 sweeps for the momentum equations and 25–50 sweeps for the pressure correction equation. The cpu–time consumption for the two approaches was about the same, but for cases of specifying sources in different grid points at different times (because the specified source (cilia) change position) the second approach yields the best results, because some time steps between removal of specified sources is necessary in order to avoid instabilities.

Steady state solution. The PISO algorithm was also used in steady state solutions and in this version under relaxation for the velocity fields was needed. The value of the under relaxation factor was between 0.70 and 0.85, where the lower value was used for stretched grids. In the present study a steady state solution means either a steady solution in the usual manner or a so called quasi–steady periodic solution, where a steady solution is obtained for different phases within the time period (different values of (26) and different positions of the specified source).

A converged solution in steady state is obtained if the normalized total residual satisfies

$$\frac{R^n}{flux} \leq 5 \cdot 10^{-4}\,, \tag{39}$$

where, for example, the flux is the total momentum inlet flux when solving the momentum equations and the total mass inlet flux when solving the pressure correction equation.

5. Numerical results

Three cases of results, which uses the cilia model presented in section 4.4, are considered here. In the first case, we consider a square cavity (100x100μm^2) where a 10 μm wide cilia band is placed at the lower cavity wall (see figure 4). In this case, results of the quasi–steady periodic Navier–Stokes equations, in which the rotational Reynolds number defined by (3) equals zero, and results of the time dependent Navier–Stokes equations for different rotational numbers are presented. In the second

case we will focus attention on the streaming velocity for quasi–steady periodic solutions and compare the results with experimental data. The streaming velocity, which is non–zero due to the nonlinearity of the problem, is found by integrating the velocities at each grid point over a complete time cycle T. In this study we consider two geometries, the squared cavity from case one (figure 4), and a geometry which is representative for the blue mussel gill (figure 5). Finally, in the third case, we consider recirculating flows as steady solutions at low Reynolds numbers. The geometry of this problem (figure 6) is presented in report 3 and has been used for experimental investigation of water transport in narrow channels. The numerical model simulates the steady flow produced by the lateral cilia band of the blue mussel gill, where a single filament is removed from the entire gill system and positioned close to a perspex plate far from other surfaces (see report 3 for further details).

In all cases presented here the specified source defined by (26) is limited to the case of $f_y=0$. The cilia velocity is described by (31) which is a representative model of the lateral band of the blue mussel (figure 7) and the drag coefficient is described by (29c) which is the drag coefficient of a cylinder with a diameter 0.1 μm and a neighbor 0.3 μm away. The removal of the specified source (cilia) is limited to displacement in only the y–direction. Physically, this model may be thought of as an actuator disc as used to represent a wind turbine or a propeller (cilia) in which the power is varied during a specified time period (beat period of the cilia). Furthermore, the position of the actuator disc is varied during the period.

Parameter selection. For all cases the results are presented with attention confined to the normalized velocity u/u_{max} and the normalized streaming u_s/u_{max} both in the x–direction where u_{max} is the maximum velocity in the effective stroke (see U_e below). We select the values f=10Hz and L=15μm which yields a maximum velocity in the effective stroke U_e=3mm/s (see (32)) and a maximum velocity in the recovery stroke U_r=0.75mm/s (see (33)).

Case I. Oscillatory flow inside a square cavity.

The dependence on the unsteady term in the Navier–Stokes equations may be evaluated by the rotational Reynolds number (Re_r) defined by (3) (see section 2). In this first case we use a 30x30 grid on a 100x100 μm^2 cavity which yields a grid size in both the x– and y–direction of $\Delta x=\Delta y=3.3$ μm. Here the translational Reynolds number is Re_t=0.30, which is a result of representative values of the lateral band of the blue mussel gill and the cavity height and the penetration amplitude defined by (23) $A_c=10\mu m$.

First, for Re_r=0.94, figure 8a–b show time dependent solutions over five periods for two grid points at the centerline of the cavity, one 14 μm (cilia tip in the effective stroke) and one 30 μm above the lower cavity wall. For comparison the figure also show the quasi–steady periodic solution (Re_r=0) in the first period. As expected, due to the nature of the boundary condition (see eq.(31)), the flow is periodic. Also the quasi–steady results correspond well to the unsteady results, and so the solution for Re_r=0.94 appears quasi–steady to a very good approximation.

Similarly, for Re_r=4.71, 23.6 and 125, figures 9–11 shows time dependent solutions over five periods for two grid points at the centerline of the cavity and in the first period the quasi–steady periodic solution. For Re_r=4.71 the solution still appears to bee quasi– steady to a good approximation. However, for the grid point 30 μm above the lower cavity wall a little amplitude difference appears at t=T/10 and t=T/5. For rotational Reynolds numbers equal to 23.6 and 125 the solutions deviate significantly from the quasi–steady solution, and so the unsteady form of the governing equations is necessary to obtain a satisfactory solution. It is noted that in the present study, where the flow is very viscous (Re_t=0.30), we only observe amplitude differences and no phase differences.

Next, for Re_r=0 (quasi–steady), 0.94, 4.71, and 23.6, figure 12 shows the normalized centerline velocity at the time t=T/10, corresponding to the instant when the cilia possess the greatest velocities (maximum effective stroke). Similarly, for Re_r=0, 125, and 625 figure 13 shows the normalized centerline velocity at t=T/10. In agreement with the time courses showed above the figures shows that for a rotational Reynolds number lesser than 23.6 quasi–steady solutions is a good approximation.

The results of figure 8–13 confirms that a quasi–steady solution will be satisfactory whenever $Re_r < O(1)$, as expected.

Comparing the centerline velocity profiles for the different rotational Reynolds numbers of figure 12 and 13, we observe that the general trend is an overall weakening of the flow away from the moving cilia (lower wall). Hence, as $Re_r \longrightarrow \infty$ the general trend appears as a concentration of the flow within a boundary layer around the cilia. Considering the Navier–Stokes equations in the limit $Re_r \longrightarrow \infty$ we obtain a balance between the unsteady term (acceleration term) and the viscous term. This indicates that the unsteady form of the Stokes equation is valid. The physical explanation of the phenomenon indicated by figures 12 and 13, as argued by Duck (1982), appear to be that, at higher values of Re_r, the greater importance of the acceleration terms in the equation of motion introduces more "lag" in the flow compared with the quasi–steady solution, and this effect offsets the trend of a weaker flow away from the moving cilia.

In the previous results we only considered the centerline velocity. To obtain a

general view of the flow field, figures 14 and 15 shows selected streamlines at t=T/10 in the cavity for the quasi–steady solution and for the time dependent solution of Re_r=625. The figures show one main eddy that, as expected from the previous set of results, move the center of the eddy towards the lower wall for increasing rotational Reynolds number.

Considering the quasi–steady solution (figure 14) we observe counter rotating fluid in a small region at each of the corners of the cavity. Such a phenomenon is commonly observed in steady solutions (see for example Pan & Acrivos 1967, see also Moffat 1964 (corner eddies)). Considering the solution for Re_r=625 we see that the counter rotating regions in the cavity corners disappear. This result is in agreement with the calculations of Duck (1982).

It is noted, that the results of figure 14 and 15 are symmetrical about the centerline which is not surprising due to the low translational Reynolds number of 0.30.

Finally, we consider the x–direction streaming velocity which is a result of the nonlinearity of the problem. Figures 16 and 17 show the normalized centerline streaming velocity for different rotational Reynolds numbers. In agreement with results considered above the figures show that for Rotational Reynolds numbers below 23.6 the quasi–steady solution appears to be a good approximation.

Case II. Streaming velocity for quasi–steady periodic solutions. Cavity and gill model.

In this case we consider quasi–steady solutions with special attention to the steady x–direction streaming velocity. Two geometries will be considered, the square cavity of case I (figure 4) and a geometry representative for the blue mussel gill (figure 5).

For the square cavity the translational Reynolds number is Re_t=0.30 and a 30x30 grid ($\Delta x=\Delta y=3.3\mu m$) is used.

First, figure 18a–b shows the normalized centerline streaming velocity for different penetration amplitudes defined by (23). For finite amplitudes figure 18a show a back flow in the cilia sublayer which decreases with decreasing penetration amplitude but maximum streaming remains at a position equal to the cilia tip in the maximum effective stroke. As expected, the streaming velocity decreases with decreasing penetration amplitude, becoming almost zero for zero penetration amplitude, as shown on figure 18b. The latter result indicates that the nonlinearity of the problem, which for a penetration amplitude equal to zero means the convective term of the Navier–Stokes equations, may be neglected. It is noted, that in figure 18b the streaming velocity in the cilia sublayer is zero. This means that fluid velocity equals cilia velocity and we have the asymptotic solution of drag coefficient $C \longrightarrow \infty$

(see eq.(28)).

Figure 19 shows the normalized centerline streaming velocity for zero penetration amplitude, but here for translational Reynolds numbers equal to 23.6 and 125. For translational Reynolds number equal to 23.6 the nonlinearity of the convective terms still only influences the flow system very little. At a Reynolds number equal to 125 it is necessary to solve the steady form of Navier–Stokes equations. It is noted, that the streaming velocity of figure 19, say for Re_t=125 (streaming due to the nonlinearity of the governing equations), is about one fifth the streaming obtained by a quasi–steady periodic solution of the present cilia model (see figure 16, Re_r=0, streaming due to an oscillating "boundary").

The results above (figure 18b and 19) and the results of case I indicate that the solution of Stokes equation will yield satisfactory results whenever Re_r<O(1) and Re_t<O(1). Hence, the governing equation has become linear and superposition of solutions is valid. For periodic solutions, as considered here, this means that only one (steady) solution for each phase, containing different penetration amplitudes (see (23)), is necessary.

Next, having attention to the linear nature of the problem, figure 20 shows the x–direction streaming velocity for one steady solution in the effective and the recovery strokes, respectively, which means that we have the same velocity throughout the effective and the recovery strokes (step function instead of the Fourier function given by (31)). Furthermore, the figure shows the solution for equal speeds in the effective and recovery strokes and, for comparison, the solution for the Fourier function given by (31) (see figure 18a, A_c=10μm). These calculations, of course, satisfy the condition of zero time mean velocity during a complete beat period T. Hence, the difference in the streaming velocity of (b) and (c) of the figure is a result of different penetration amplitudes in some part of the effective stroke (the penetration amplitude, A_c, is not 10μm throughout the effective beat for the solution with cilia velocity given by the Fourier function (31)). If the governing equations are linear as suggested above then we only expect to obtain streaming through cilia oscillations and not through the convective terms. The difference of figure 20a and b arise mainly from the nonlinearity of cilia oscillations and only about 10% arise from the nonlinearity of the convective terms. Further step function calculations, with zero penetration amplitude (only streaming through the convective term) and different translational Reynolds numbers, shows that the governing equations are nonlinear in each phase (here the effective phase and the recovery phase) and that for Re_t>0.05 the convective term influence the flow system. But it is noted that this nonlinearity does not affect the streaming for calculations with cilia velocity given by the fourier function (31) (see figure 18b and 19, integration over a complete time cycle of many

nonlinear solutions).

Finally, for Re_r=0 and Re_t=0.30, figure 21 shows streamlines for the streaming velocity. The figure shows one main eddy located at a position about one third the cavity height from the lower cavity wall and one eddy located in the cilia sublayer. Furthermore, the streaming velocity, as in the case of a quasi–steady solution at t=T/10 (see figure 14), shows four symmetric recirculating regions in the cavity corners.

Comparing the streaming velocity of figure 18a for a penetration amplitude of 10 μm, which is about the value of the lateral band of the blue mussel (Aiello & Sleigh 1972), with measured velocities of Jørgensen (1982) for an isolated gill filament (see also report 3), we obtain about one fourth the value measured by Jørgensen at a position corresponding to about the cilia tip in effective stroke. It is noted that the present geometry is not quite that used by Jørgensen. However, calculations for an equivalent geometry (2000x600 μm^2 cavity with a gill filament placed about 200 μm above the lower cavity wall) yield the same result.

For the blue mussel gill geometry we use a step function with maximum cilia velocity in one fifth of the beat period and one fourth the maximum velocity (negative x–direction) in four fifth of the beat period (the same function as used in (b) of figure 20, see also eq.(33)). The translational Reynolds number is Re_t=0.12 (based on the channel height) and a 40x32 grid (Δx=7.5μm, Δy=2.5μm) is used.

Figure 22 shows, for different phase relations on the lower "cilia band" (see figure 5), the mean x–direction streaming velocity (streaming velocity integrated across the channel) in the channel. The figure shows that two cilia bands in phase yield a greater streaming than two cilia bands out of phase. This result is in agreement with a perturbation solution of the creeping flow equation (see report 1).

Comparing the result of figure 22 having the two cilia bands in phase with experimental mean velocities, calculated from the pumping rate, the gill area, and the filamentary and interfilamentary dimensions of the intact blue mussel (see for example Walne 1972, Jørgensen 1975, Møhlenberg & Riisgård 1979, Kiørboe et al. 1980, or Jørgensen et al. 1986) we obtain about one fifth of these values.

The reason for the significant discrepancy between measured and calculated velocities may be a cilia model which not quite represent realistic cilia movement and the three–dimensional beat of the lateral cilia which is not considered in the present study.

Case III. Flow separation of steady solutions at low Reynolds numbers

The calculations of case II presented above yields velocities of one fourth to one fifth

the values obtained experimentally. Let us assume that the velocities throughout the beat period equals the maximum velocity in the effective stroke (experimental data input for the numerical model) and then use a steady state solution procedure. This steady procedure means, compared with the quasi–steady periodic procedure of case I and II above, a steady solution for only one phase, here the phase at t=T/10. This simple model is used for comparison with experimental investigations. However, this comparison is not done here but a detailed description is given in report 3.

Presently we focus attention on flow separation of steady solutions at low Reynolds numbers. The translational Reynolds number, based on three different channel widths of the model of figure 6, h=40μm, h=100μm, and h=200μm, are Re_t=0.12, 0.30, and 0.60, respectively. We use a stretched 100x100 cartesian grid with minimum grid size Δx and Δy of 8.6μm and 3.0μm, respectively, and a maximum velocity input of 3.0 mm/s. This maximum value is a typical maximum measured value for experimental investigation of the same model (see rapport 3).

First, for channel width h=100μm, figure 23 shows streamlines of the overall calculation domain (see also figure 6) and a picture magnified 64 times of the flow between the perspex plate and the gill filament. Figure 24 shows streamlines around the filament and between the filament and the perspex plate for 256 x magnification. The figure shows recirculating flow near the perspex plate for a position equal to about the lateral cilia band. The eddy is about 50 μm wide and about 68 μm deep (measured from the perspex plate). Defining a nondimensional depth of penetration ($\hat{y}_{eddy}$) for the recirculating flow near the perspex plate as the ratio of the distance from the perspex plate to the end of the eddy to the channel height ($\hat{y}_{eddy}$= $\Delta y_{recirculating}$/h) we obtain, for this channel, $\hat{y}_{eddy}$=0.68. The center of the eddy is located about 2.5μm upstream of the centerline of the lateral cilia band.

Similarly, for channel widths h=200μm and h=40μm, figures 25 and 26a show streamlines around the filament and between the filament and the perspex plate for a 256 x magnification. Figure 26b shows velocity vectors instead of streamlines for the case of h=40μm. In figure 25 (h=200μm) the eddy is about 100 μm wide and about 120 μm deep, which for the latter value yields $\hat{y}_{eddy}$=0.60. The center of the eddy for this channel width is located about 21 μm upstream of the centerline of the lateral cilia band. Figure 26a (h=40μm) shows an eddy that is about 29μm wide, 21μm deep, $\hat{y}_{eddy}$=0.53, and the center of the eddy is located at the centerline of the lateral band. Hence, for this case the eddy is symmetrical about the lateral band.

It is expected that the recirculating flow regions near the perspex plate are a result of an adverse pressure gradient due to wall friction on the perspex plate. In all cases considered so far the perspex plate was about 5mm long (filament length was about 120μm). Now, for the case of h=100μm, figure 27 shows velocity vectors around

the filament and between the filament and the perspex plate for a 256 x magnification. For this case the length of the perspex plate is the same as the filament length about 120μm (this model is physically impossible and is only studied numerically), but the recirculating region still exists. Further calculations show that when the perspex plate is one grid point (~10μm) upstream and downstream of the lateral cilia band the eddy disappears for the grid used in the present calculations.

Finally, the calculations of this case show that the magnitude of the eddy motion near the perspex plate increases with decreasing channel width. The velocity profile for channel width h=40μm is fully developed a very short distance after the lateral band (see figure 26a or 26b) which is contrary the channels of width h=100μm and h=200μm where the velocity profile never becomes fully developed before leaving the channel.

6. Conclusions

In conclusion, this report has presented a discrete cilia model for water propulsion based on a numerical approach. The unsteady as well as the steady form of the Navier–Stokes equations have been solved for a periodic oscillating "interior boundary" which represents cilia movement in the interior of the calculation domain.

Three cases of results are considered, that of oscillating flow inside a square cavity, that of streaming velocity of quasi–steady periodic solutions, and that of flow separation of steady solutions at low Reynolds numbers. In the first case, results of the quasi–steady periodic Navier–Stokes equations in which the rotational Reynolds number defined by (3) equals zero and results of the time dependent Navier–Stokes equations for different rotational numbers are discussed. In the second case, special attention was given to the streaming velocity for quasi–steady periodic solutions with the geometry of case one and a geometry representative for the blue mussel gill. Finally, in the third case, flow separation of steady solutions at low Reynolds numbers has been considered.

The results indicate that the unsteady term in the Navier–Stokes equations may be neglected for a rotational Reynolds number ($Re_r = \ell^2\omega/\nu$) less than about order unity and that the convective term (nonlinear term) may influence the flow system when the translational Reynolds number ($Re_t = \ell U/\nu$) is greater than about 0.05. For $Re_r \longrightarrow \infty$ the general trend appears as a concentration of the flow within a boundary layer around the cilia. The physical explanation of this phenomenon appear to be that, at higher values of Re_r, the greater importance of the acceleration terms in the equation of motion introduces more "lag" in the flow, compared with the

quasi–steady solution, and this effect offsets the trend of a weaker flow away from the moving cilia. For quasi–steady periodic solutions the results indicate counter rotating fluid in a small region of the corners of the cavity but, in agreement with Duck's (1982) calculations, these eddies disappear for unsteady solutions.

The streaming velocity, which in general appears in oscillatory flows, is a result of the nonlinearity of the problem and in the present study a result of purely oscillating cilia motion or a combination of cilia motion and streaming from the nonlinear terms of the governing equations. Also, the streaming velocity indicates corner eddies as in the quasi–steady results above and furthermore recirculating flow in the cilia sublayer. The present values of streaming yields one fourth to one fifth the values obtained experimentally for the blue mussel. This significant discrepancy may be explained by a cilia model which does not quite represent realistic cilia movements and by the three–dimensional beat of the lateral cilia which is not considered in the present study, suggesting the need for further analysis.

Steady solutions of low Reynolds number flow between a filament and a perspex plate, representing partly one narrow channel of the entire blue mussel gill, shows recirculating flow near the perspex plate. These eddies, which are expected to be a result of an adverse pressure gradient due to wall friction on the perspex plate, increase in magnitude for decreasing channel width. The center of the eddies are located symmetrically about the lateral cilia band for channel width equal to 40μm and are moving upstream of the of the lateral band for increasing channel width.

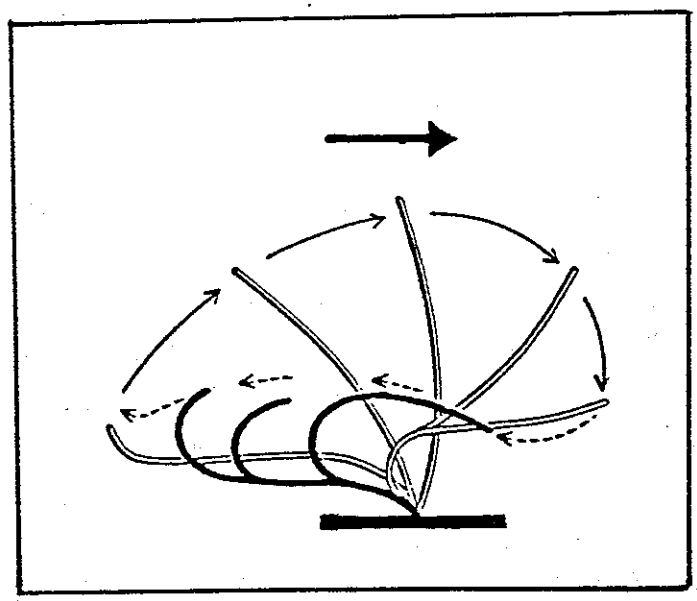

Figure 1. Typical pattern of cilia motion which show stages in the cycle of beating of a cilium, with stages of the effective stroke shown as solid lines and stages of the recovery stroke as dotted lines. The heavy arrows indicate the resultant water flow (adapted from Satir 1974).

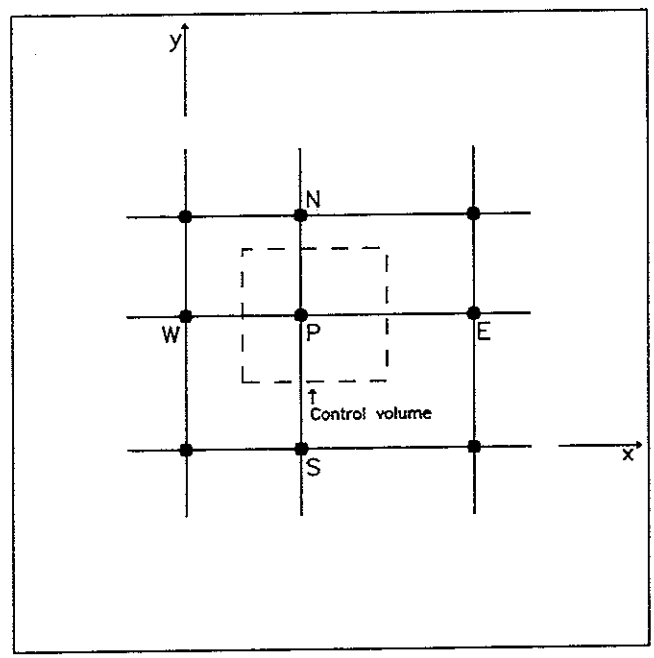

Figure 2. Main control volume for the two–dimensional situation. The figure show face locations and associated neighbours.

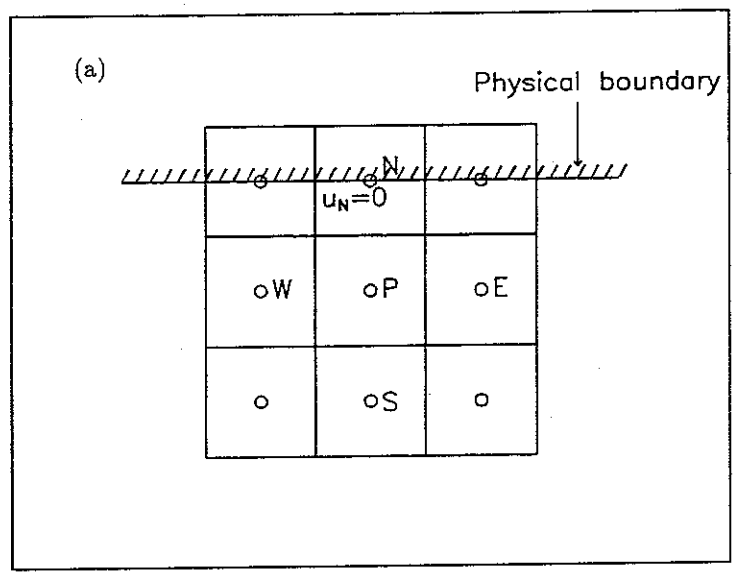

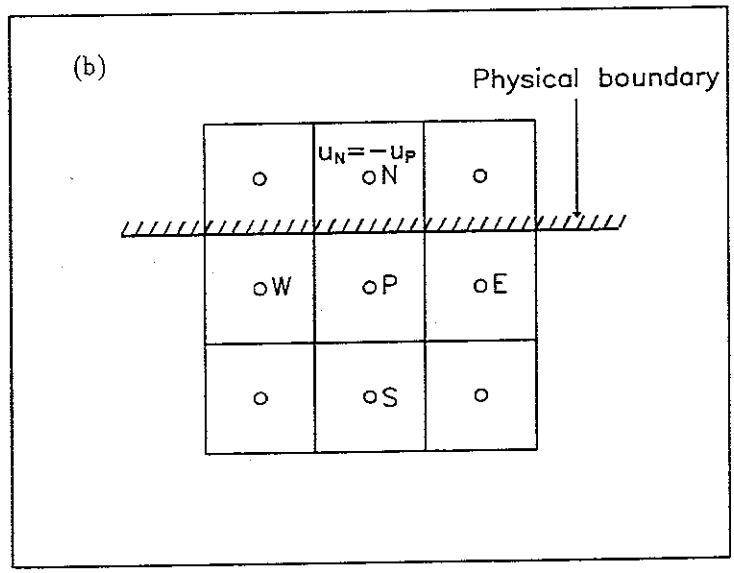

Figure 3a–b. Boundary conditions for rigid, impermeable wall where a linear vibration of the dependent variable is assumed across the wall. (a) node on wall, (b) node outside wall.

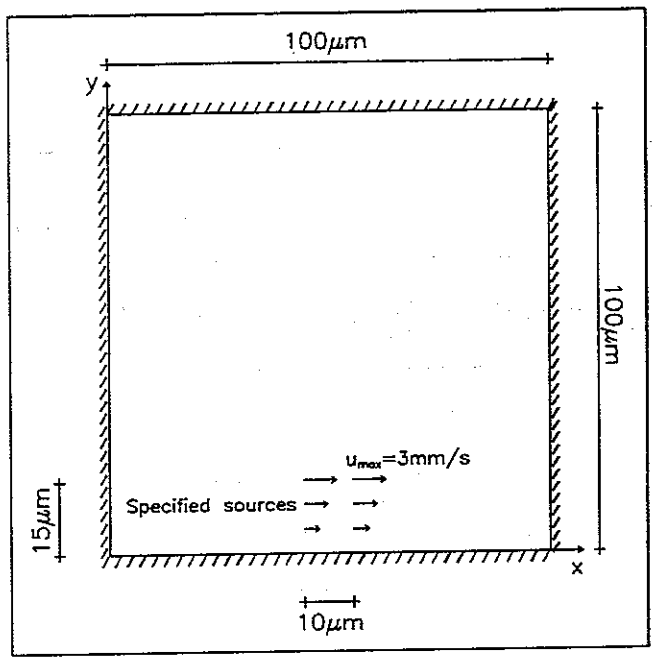

Figure 4. Layout of case I. Driven cavity with oscillating sources (cilia) in interior.

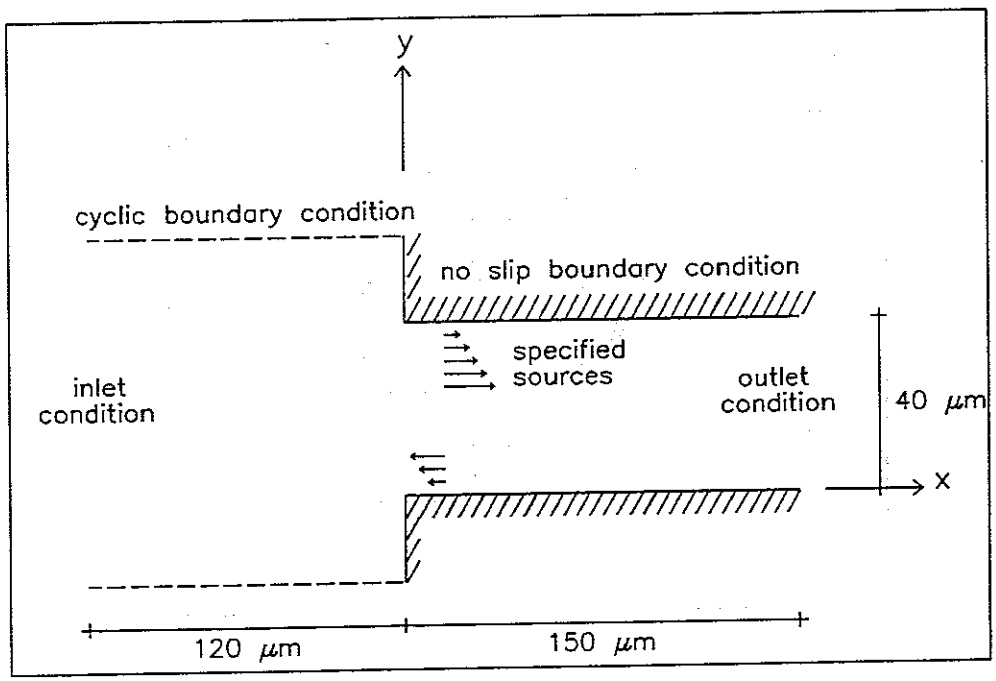

Figure 5. Layout of case II. Geometry of the blue mussel gill with specified sources simulating the lateral cilia.

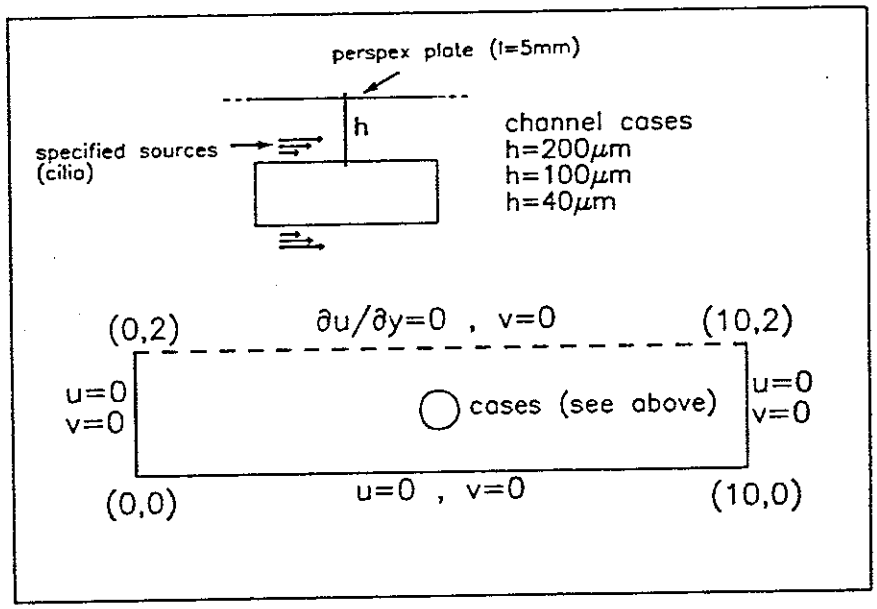

Figure 6. Layout of case III. Lower part; boundary conditions and coordinates in cm. Upper part; single gill filament and perspex plate representing partly one narrow channel of the the entire blue mussel gill. The specified sources represents the lateral cilia.

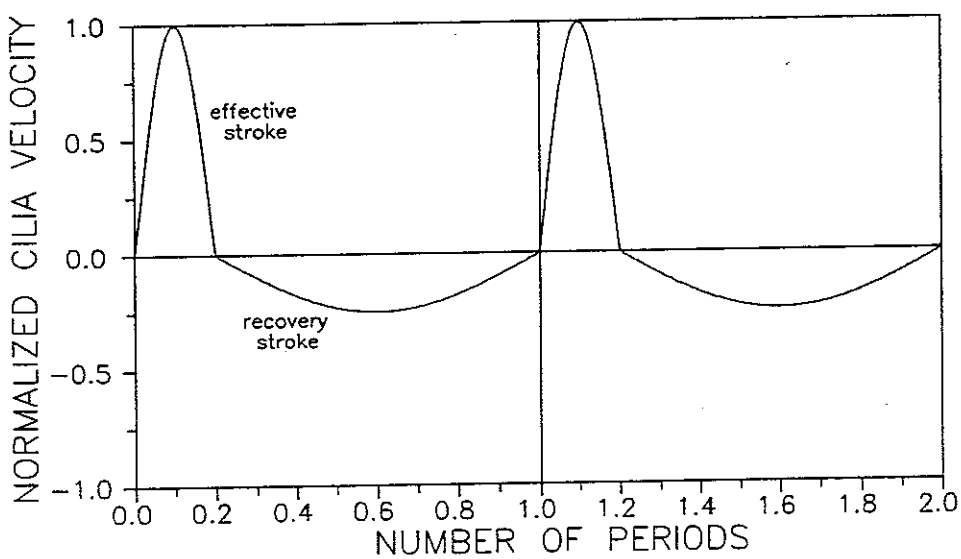

Figure 7. Cilia velocity in the effective and the recovery strokes (see eq.(31), n=50). This model is represents the lateral cilia of the blue mussel.

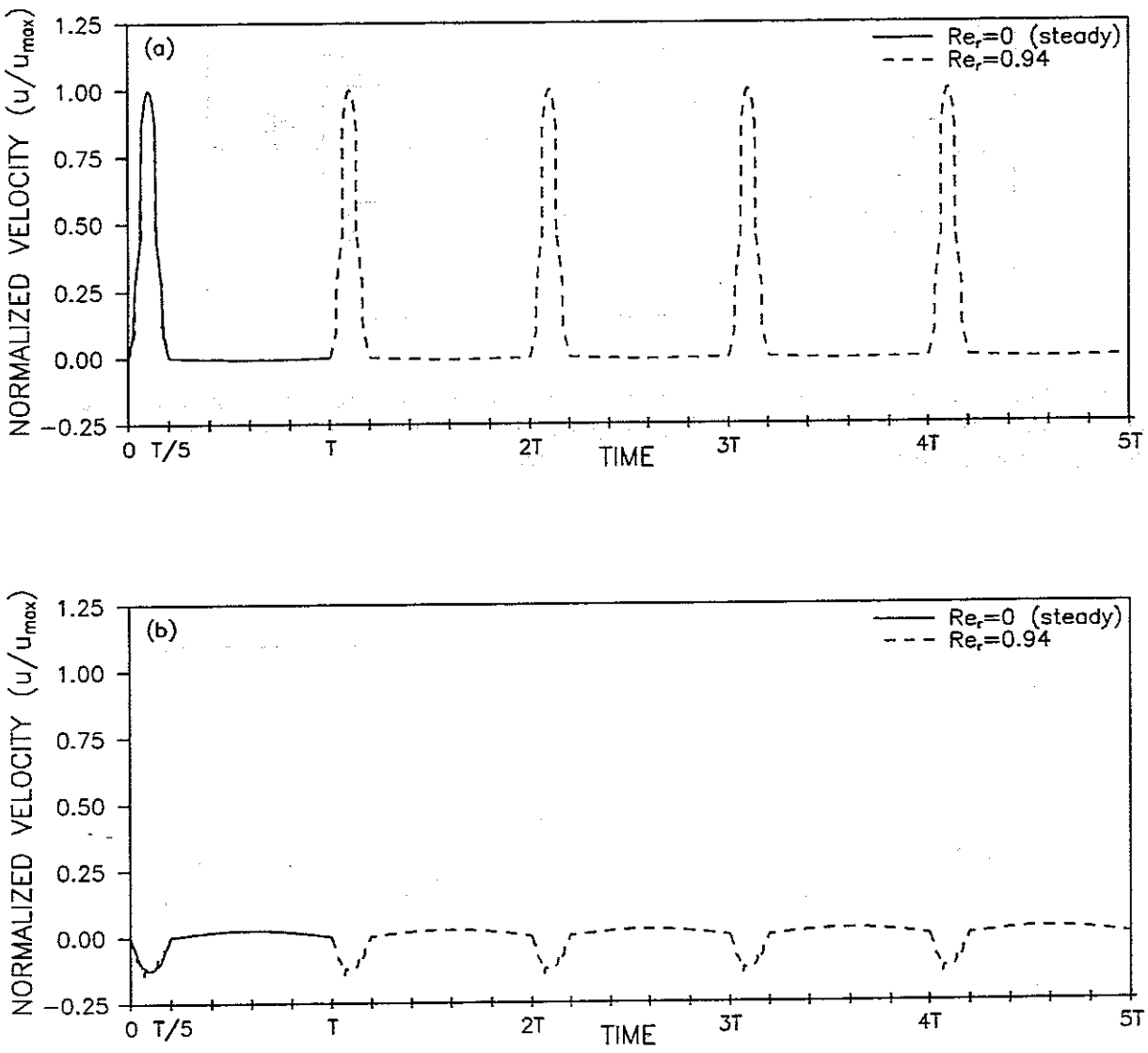

Figure 8a–b. Time dependent solutions over five periods for a specified grid point at x=50μm and (a) y=14μm, (b) y=30μm; case of Re_r=0 (steady), Re_r=0.94, Re_t=0.30, 30x30 grid (Δx=Δy=3.3 μm), $\Delta t=6.9\cdot10^{-5}$s, u_{max}=3.0mm/s, A_c=10μm.

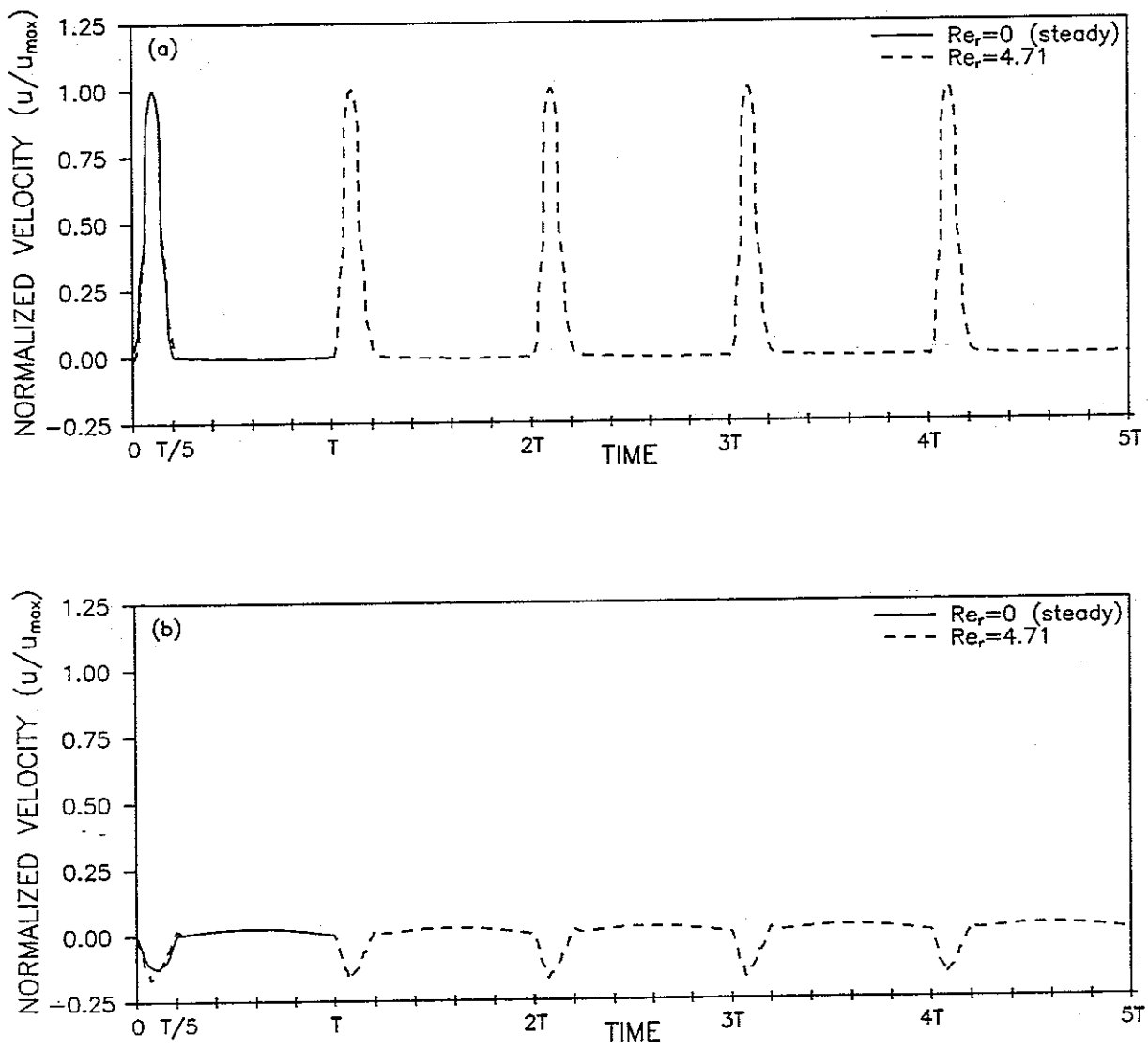

Figure 9a–b. Time dependent solutions over five periods for a specified grid point at x=50μm and (a) y=14μm, (b) y=30μm; case of Re_r (steady), Re_r=4.71, Re_t=0.30, 30x30 grid ($\Delta x=\Delta y$=3.3 μm), $\Delta t=5.6\cdot10^{-5}$s, u_{max}=3.0mm/s, A_c=10μm.

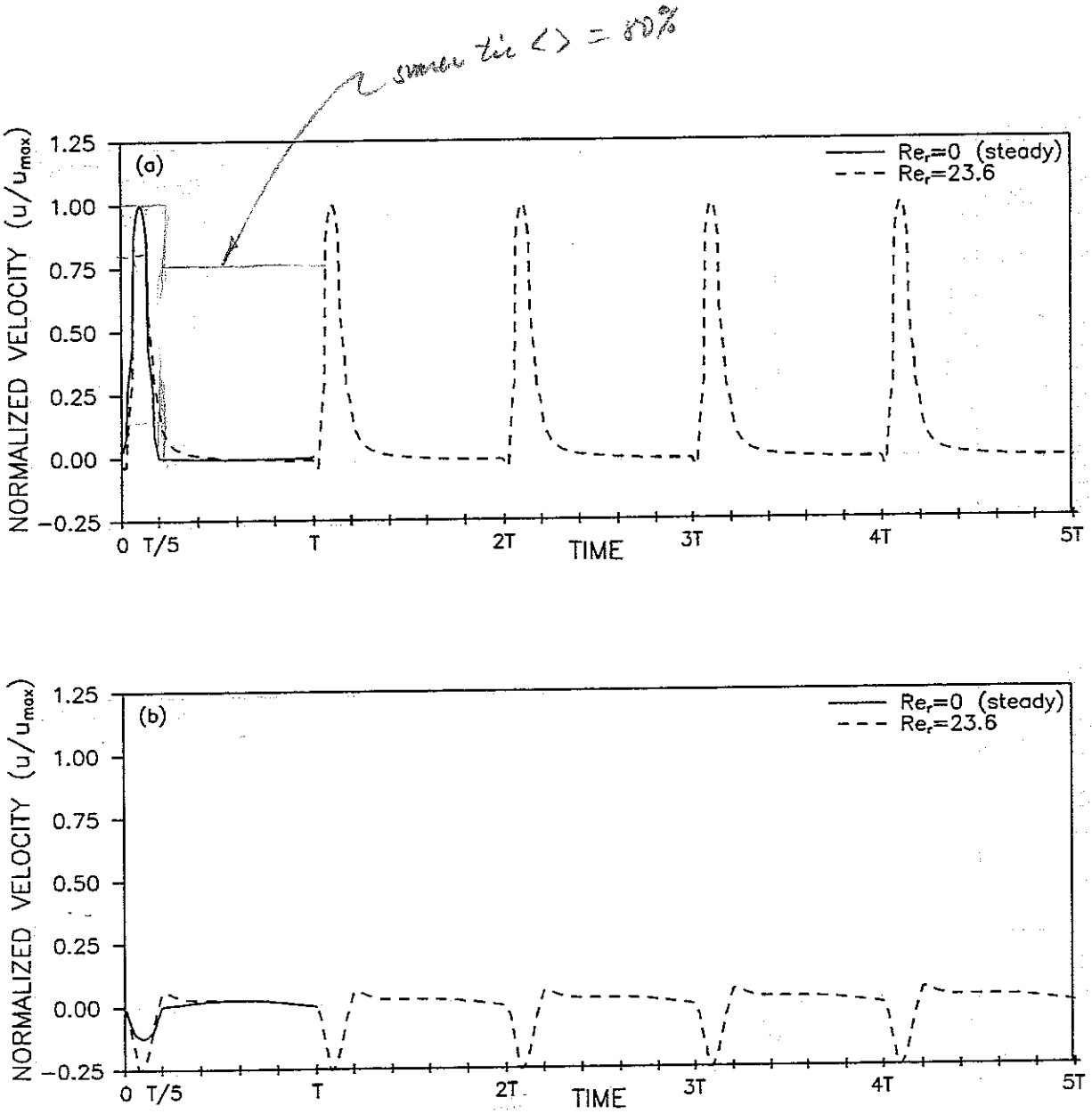

Figure 10a–b. Time dependent solutions over five periods for a specified grid point at x=50μm and, (a) y=14μm, (b) y=30μm; case of Re_r=0 (steady), Re_r=23.6, Re_t=0.30, 30x30 grid (Δx=Δy=3.3μm), $\Delta t=2.2\cdot10^{-5}$s, u_{max}=3.0mm/s, A_c=10μm.

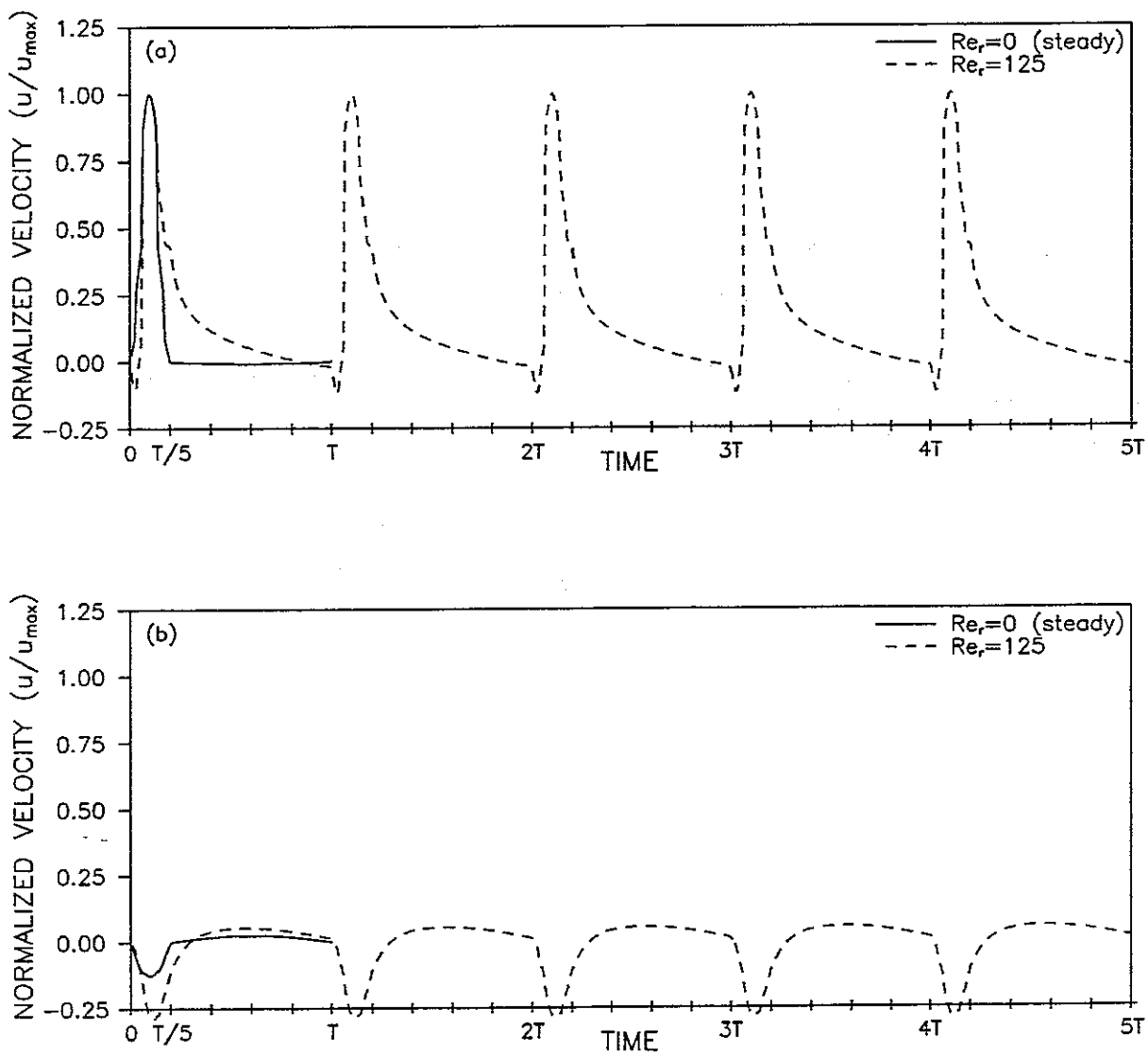

Figure 11a—b. Time dependent solutions over five periods for a specified grid point at x=50μm and (a) y=14μm, (b) y=30μm; case of Re_r=0 (steady), Re_r=125, Re_t=0.30, 30x30 grid (Δx=Δy=3.3 μm), $\Delta t = 4.2 \cdot 10^{-6}$s, u_{max}=3.0mm/s, A_c=10μm.

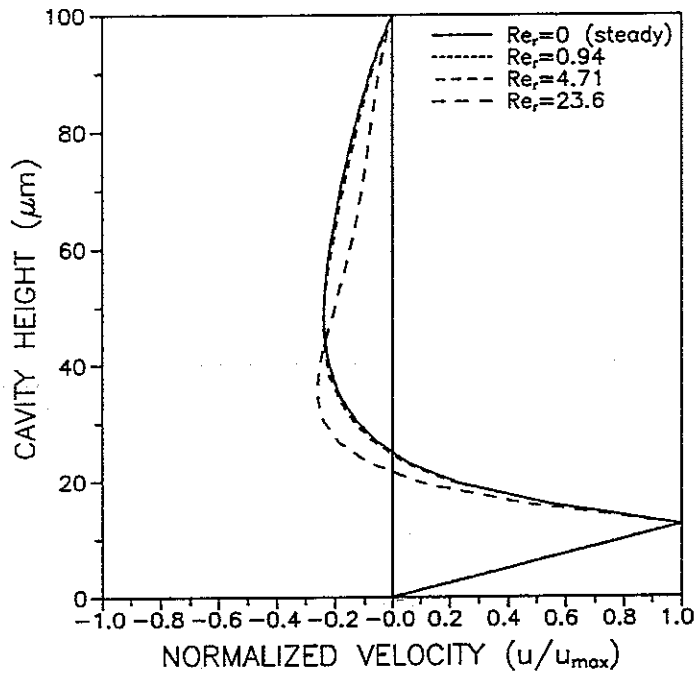

Figure 12. Normalized centerline velocity profiles (u/u_{max}) at t=T/10 for different rotational Reynolds numbers, Re_r=0, Re_r=0.94, Re_r=4.71, Re_r=23.6; case of Re_t=0.30, 30x30 grid ($\Delta x = \Delta y = 3.3\mu m$), Δt (see figure 8, 9, and 10), u_{max}=3.0mm/s, A_C=10μm.

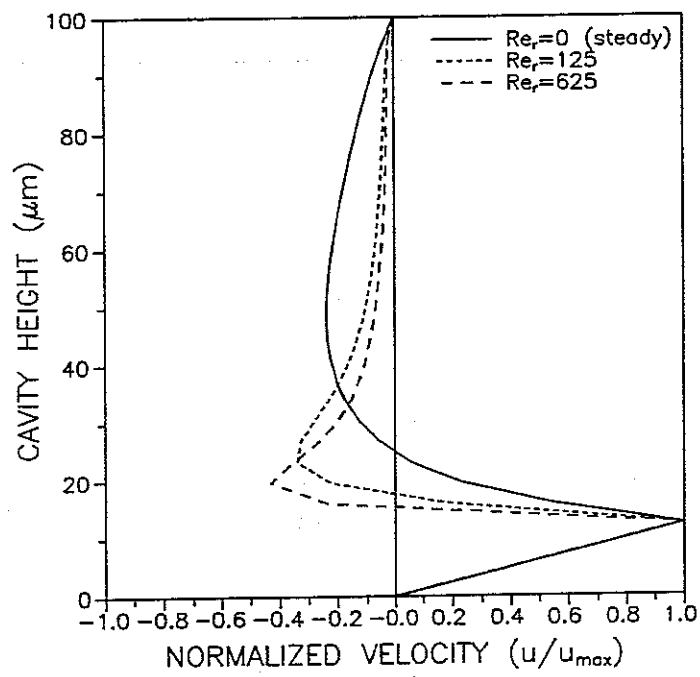

Figure 13. Normalized centerline profiles (u/u_{max}) at t=T/10 for different rotational Reynolds numbers, Re_r=0, Re_r=125, Re_r=625; case of Re_t=0.30, 30x30 grid ($\Delta x = \Delta y = 3.3\mu m$), $\Delta t(Re_r=125) = 4.2 \cdot 10^{-6}$s, $\Delta t(Re_r=625) = 8.4 \cdot 10^{-7}$s, u_{max}=3.0mm/s, A_C=10μm.

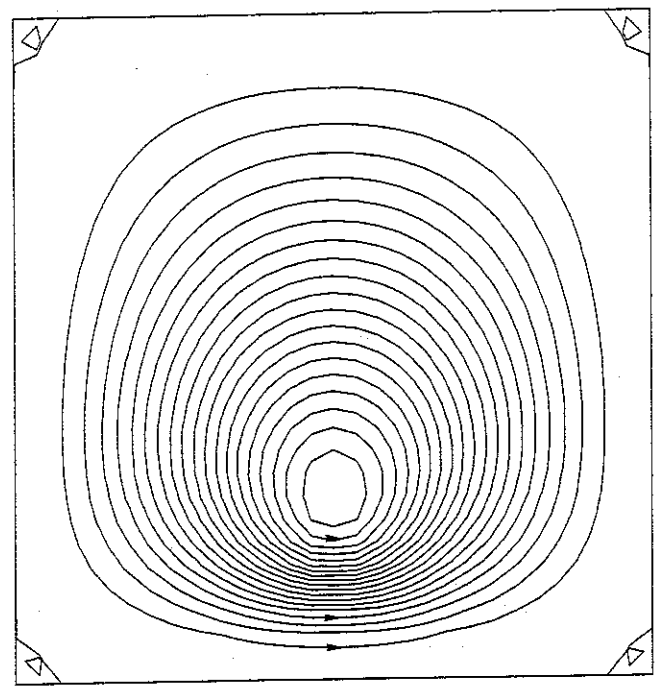

Figure 14. Streamlines at t=T/10 for the quasi–steady periodic solution of a driven cavity ($100\text{x}100\mu\text{m}^2$); case of $\text{Re}_r=0$, $\text{Re}_t=0.30$, 30x30 grid ($\Delta x=\Delta y=3.3\mu\text{m}$), $A_c=10\mu\text{m}$, $\Delta\psi=1.20\cdot10^{-9}$ m^2/s, $\Delta\psi_{\text{corners}}=3.60\cdot10^{-13}\text{m}^2/\text{s}$.

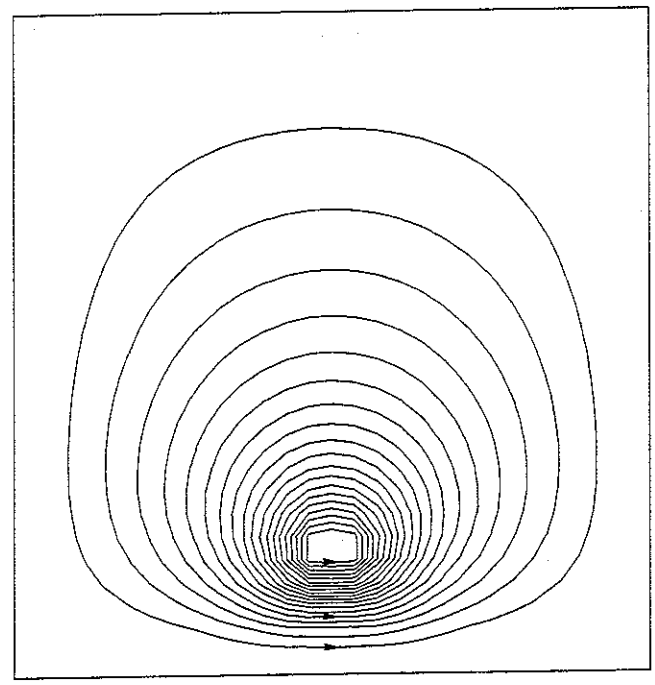

Figure 15. Streamlines at t=T/10 for the unsteady solution of a driven cavity; case of $\text{Re}_r=625$, $\text{Re}_t=0.30$, 30x30 grid ($\Delta x=\Delta y=3.3\mu\text{m}$), $\Delta t=8.4\cdot10^{-7}$, $A_c=10\mu\text{m}$, $\Delta\psi=1.20\cdot10^{-9}\text{m}^2/\text{s}$.

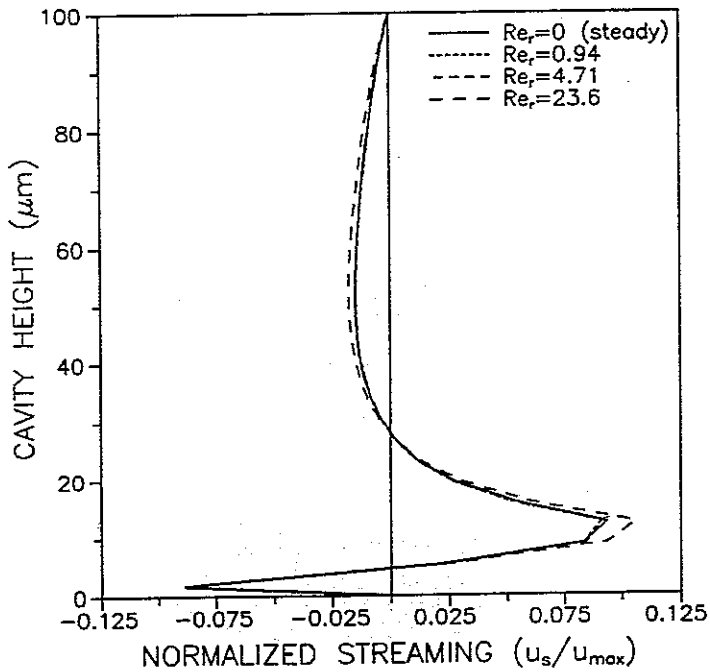

Figure 16. Normalized centerline streaming velocity profiles (u_S/u_{max}) for different rotational Reynolds numbers, Re_r=0, Re_r=0.94, Re_r=4.71, Re_r=23.6; case off Re_t=0.30, 30x30 grid ($\Delta x=\Delta y=3.3\mu m$), Δt (see figure 8, 9, and 10), u_{max}=3.0mm/s, $A_C=10\mu m$.

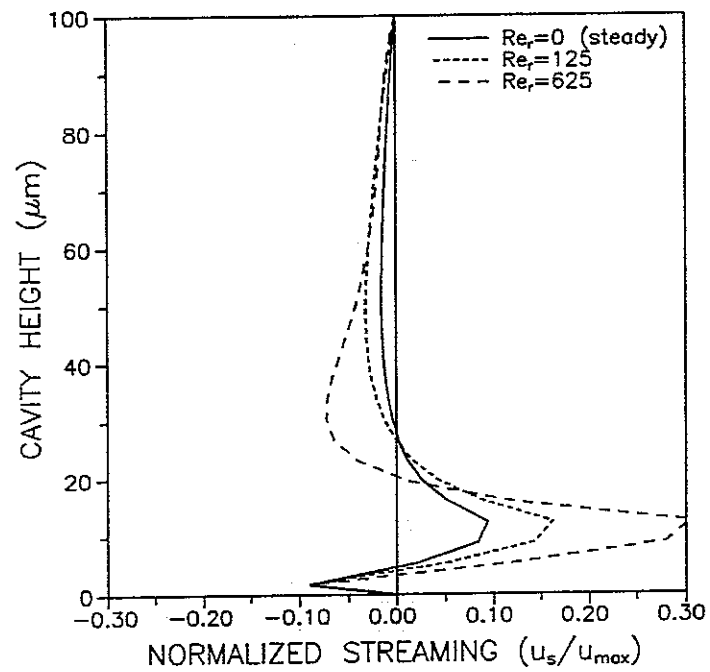

Figure 17. Normalized centerline streaming velocity profiles (u_S/u_{max}) for different rotational Reynolds numbers, Re_r=0, Re_r=125, Re_r=625; case of Re_t=0.30, 30x30 grid ($\Delta x=\Delta y=3.3\mu m$), $\Delta t(Re_r=125)=4.2\cdot10^{-6}$s, $\Delta t(Re_r=625)=8.4\cdot10^{-7}$s, u_{max}=3.0mm/s, $A_C=10\mu m$.

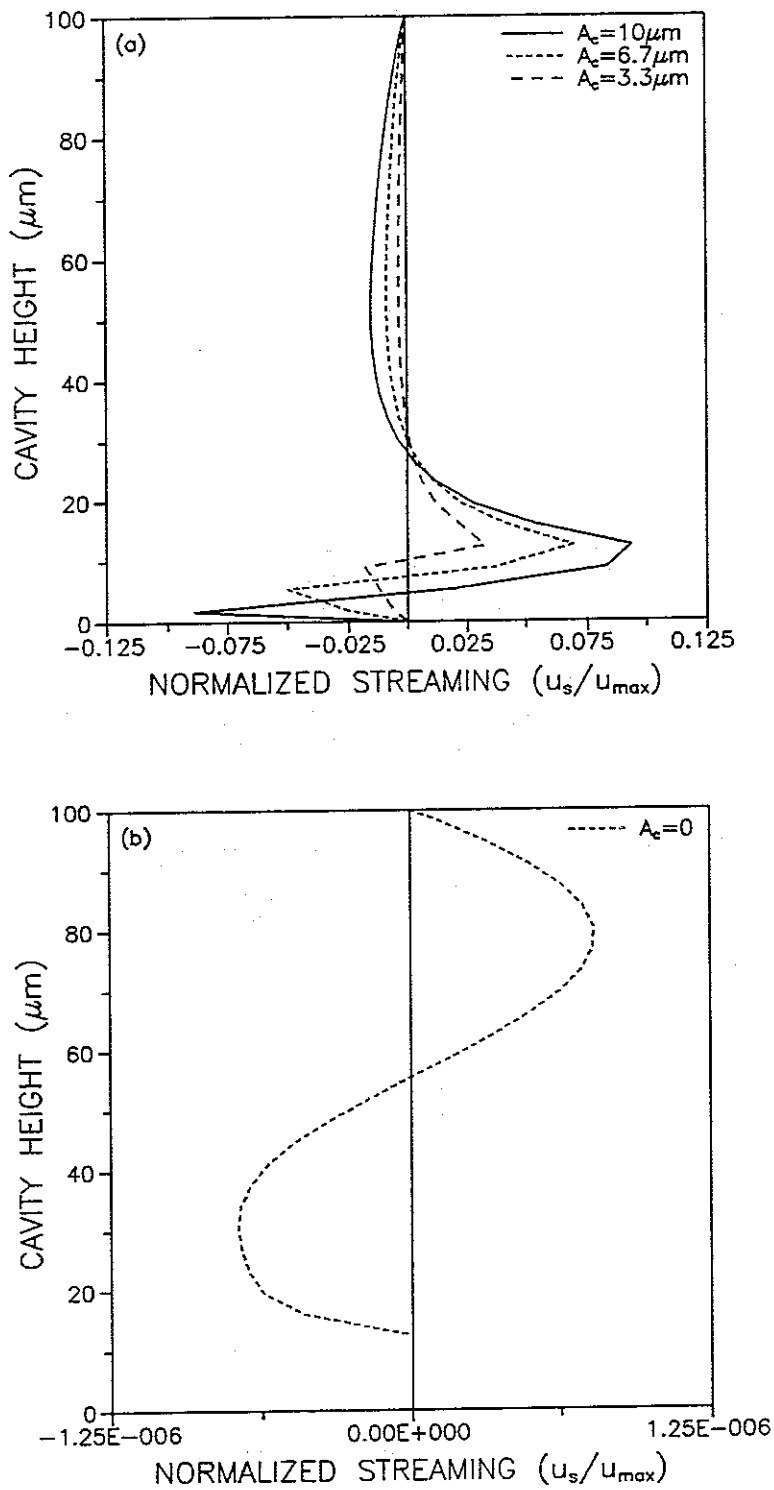

Figure 18a–b. Normalized centerline streaming velocity profiles (u_S/u_{max}) for different penetrations amplitudes (a) A_C=10μm, A_C=6.7μm, A_C=3.3μm; (b) A_C=0; case of Re_r=0, Re_t=0.30, 30x30 grid ($\Delta x=\Delta y$=3.3μm), u_{max}=3.0mm/s.

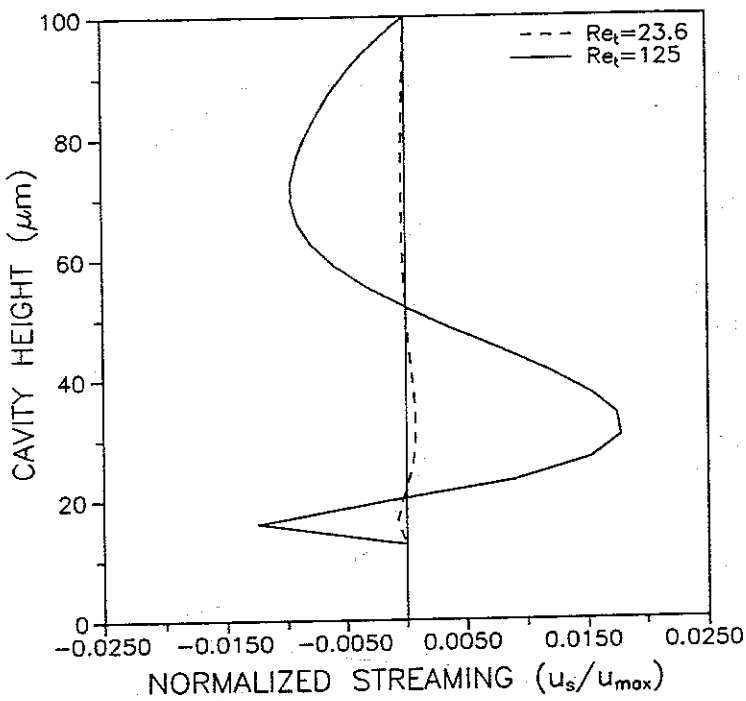

Figure 19. Normalized centerline streaming velocity profiles (u_S/u_{max}) for different Reynolds numbers; case of Re_r=0, Re_t=23.6 (u_{max}=0.236m/s), Re_t=125 (u_{max}=1.25m/s), 30x30 grid ($\Delta x=\Delta y=3.3\mu m$), $\Delta t(Re_r=23.6)=2.2\cdot10^{-5}$s, $\Delta t(Re_r=125)=4.2\cdot10^{-6}$s, A_C=0.

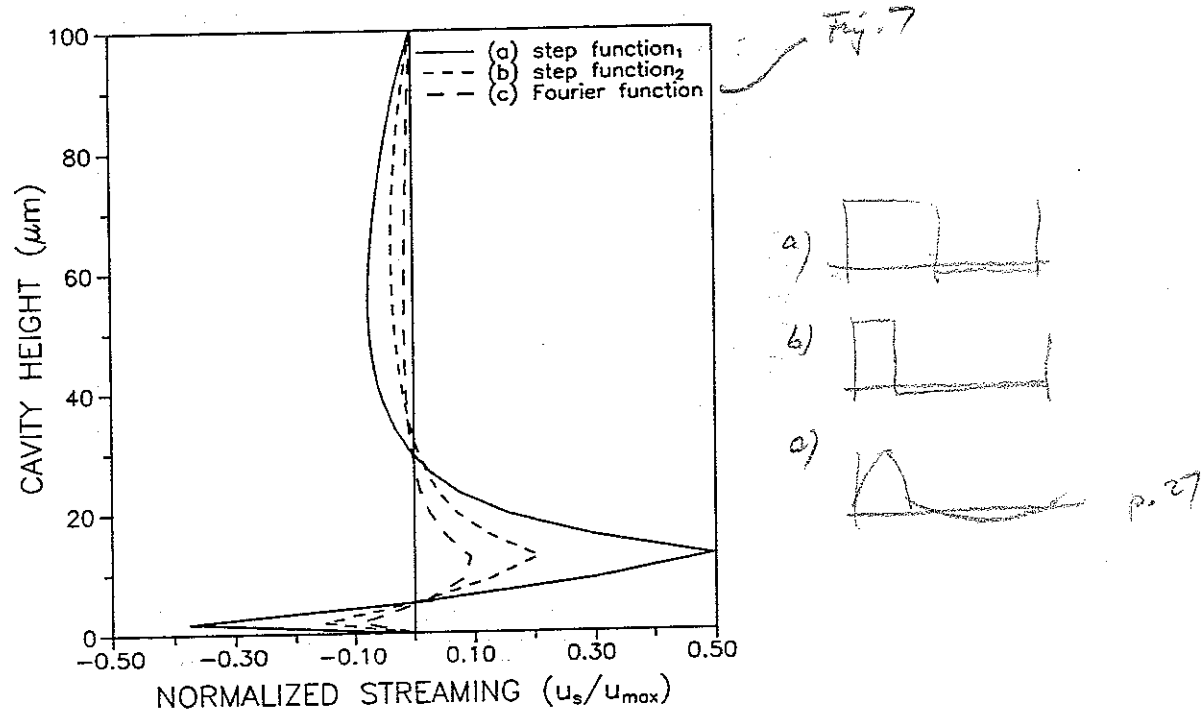

Figure 20. Normalized centerline streaming velocity profiles (u_S/u_{max}) for different velocity functions (a) step function, $\Delta t_{eff}=\Delta t_{rec}=1/2T$, (b) step function, $\Delta t_{eff}=1/5T$, $\Delta t_{rec}=4/5T$ (c) Fourier function $\Delta t_{eff}=1/5T$, $\Delta t_{rec}=4/5T$; case of Re_r=0, Re_t=0.30, 30x30 grid ($\Delta x=\Delta y=3.3$ μm), u_{max}=3.0mm/s, $A_C=10\mu m$.

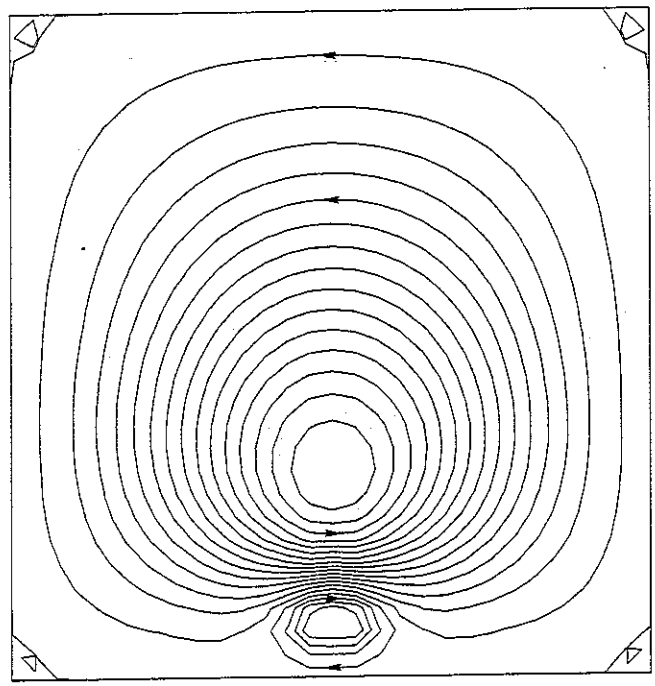

Figure 21. Streamlines of the streaming velocity for a driven cavity ($100x100\mu m^2$); case of $Re_r=0$, $Re_t=0.30$, 30x30 grid ($\Delta x=\Delta y=3.3\mu m$), $u_{max}=3.0mm/s$, $A_c=10\mu m$, $\Delta\psi=2.83\cdot10^{-9}m^2/s$, $\Delta\psi_{corners}=3.11\cdot10^{-14}m^2/s$.

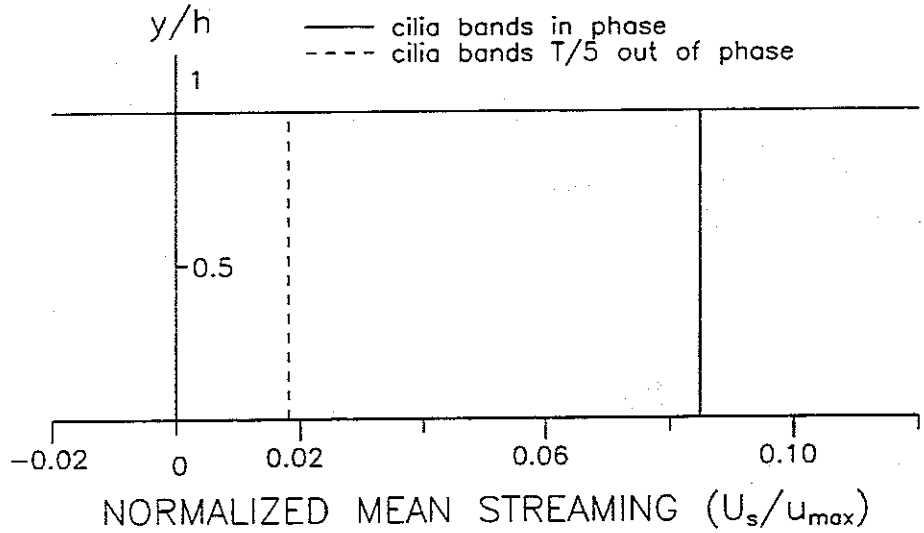

Figure 22. Mean normalized x–direction streaming velocity (U_S/u_{max}) for the blue mussel geometry. Two cases of results are considered, the two "cilia bands" in phase (solid line) and the two "cilia bands" T/5 out of phase (dashed line); case of $Re_r=0$, $Re_t=0.12$, 40x32 grid ($\Delta x=7.5\mu m$, $\Delta y=2.5\mu m$), $u_{max}=3.0mm/s$, $A_c=10\mu m$, $h=40\mu m$.

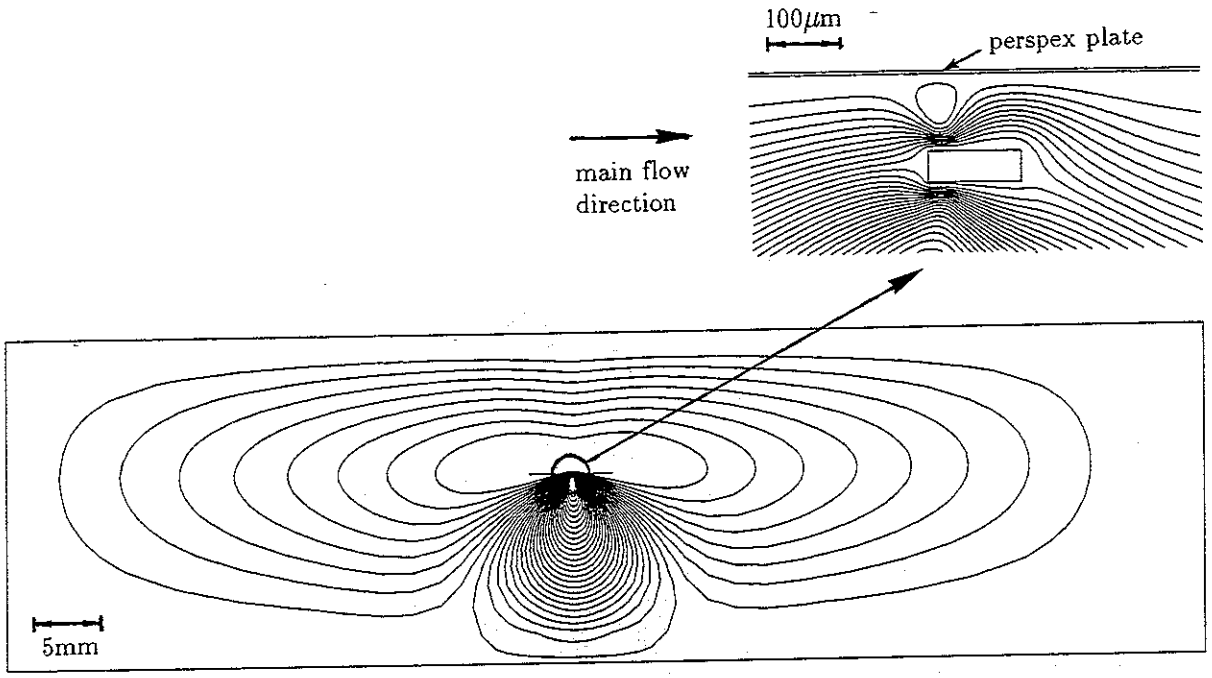

Figure 23. General view of the calculations domain (see also figure 6) and a picture magnified 64 times of the flow between the perspex plate and the gill filament; steady solution case of Re_t=0.30, 100x100 grid ($\Delta x_{channel}$=8.58μm, $\Delta y_{channel}$=4.56μm), $u_{max,input}$=3.0mm/s, A_C=10μm, h=100μm, $l_{perspex}$=5mm, $\Delta\psi$=2.40$\cdot 10^{-9}$m^2/s.

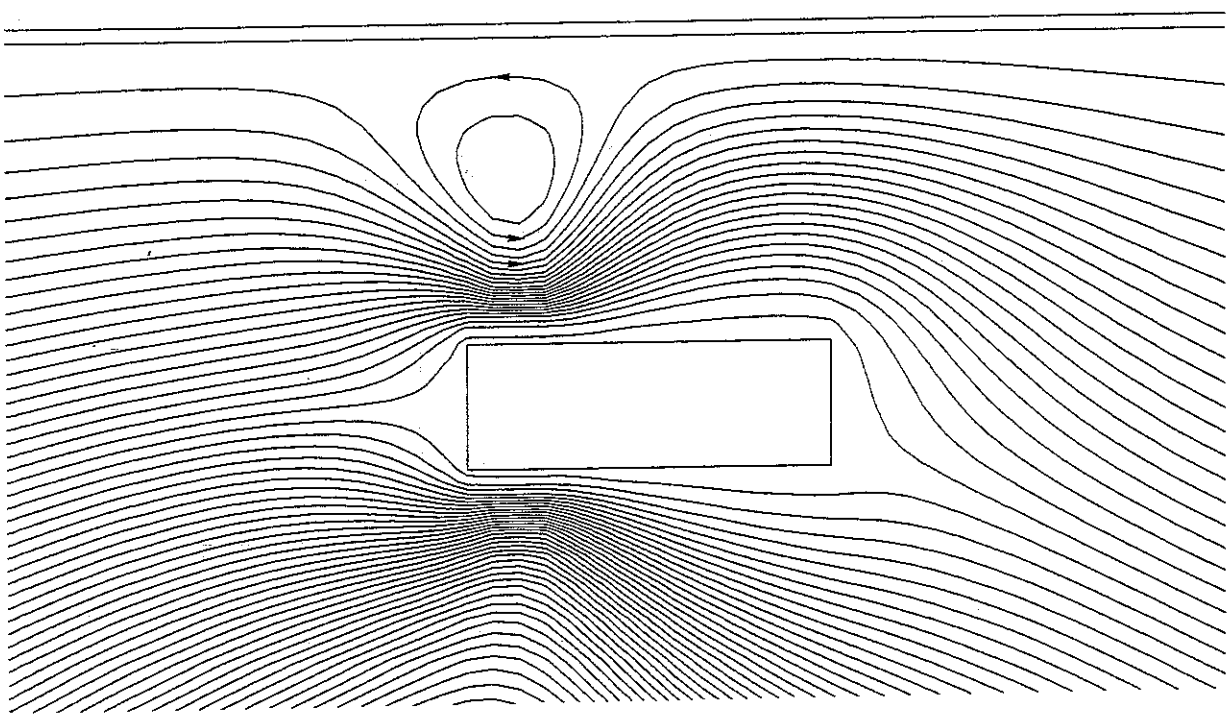

Figure 24. Streamlines around the filament and between the filament and the perspex plate for 256 x magnification.; steady solution case of Re_t=0.30, 100x100 grid ($\Delta x_{channel}$=8.58μm, $\Delta y_{channel}$=4.56μm), $u_{max,input}$=3.0mm/s, A_C=10μm, h=100μm, $l_{perspex}$=5mm, $\Delta\psi$=2.40$\cdot 10^{-9}$ m^2/s.

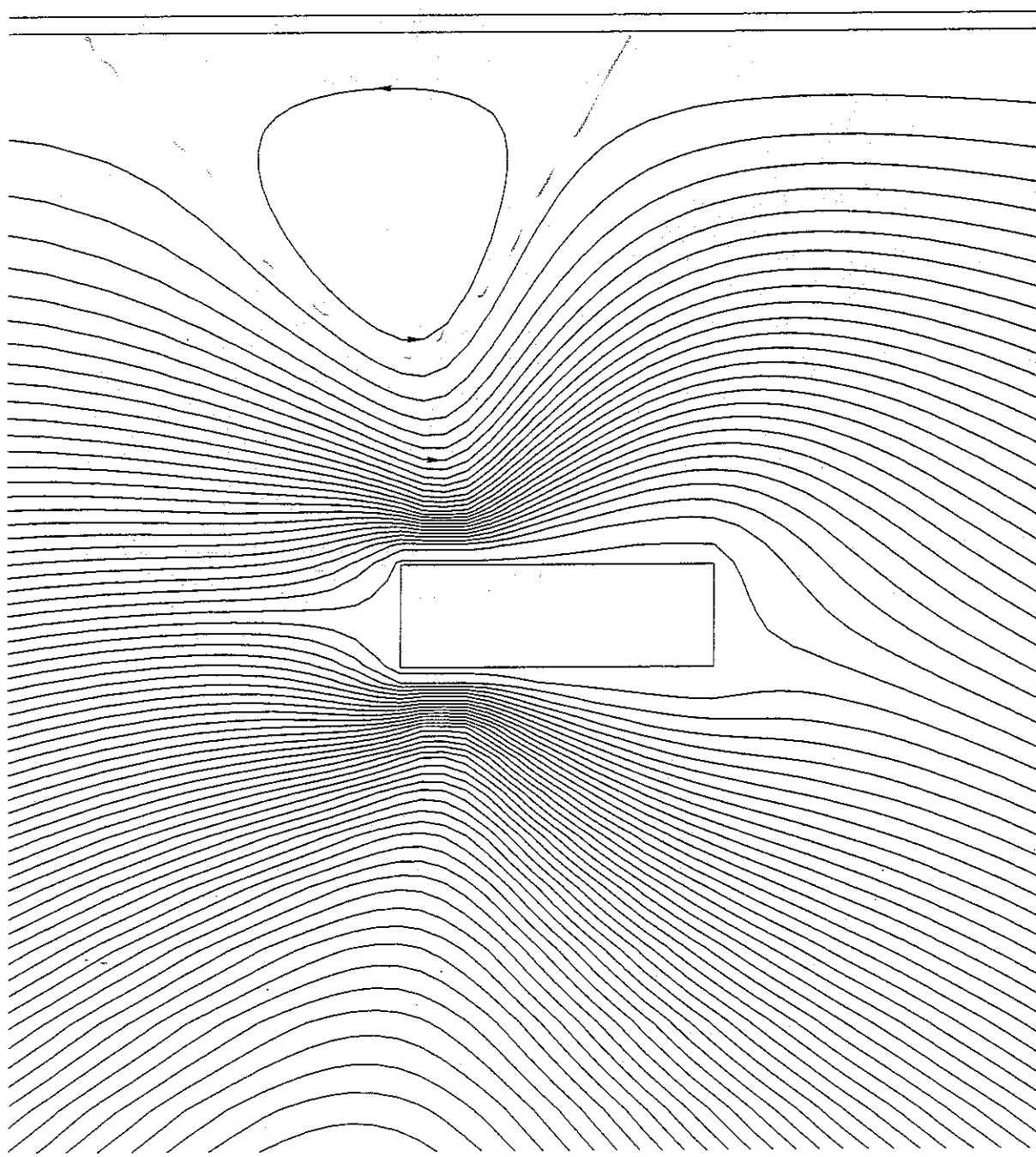

Figure 25. Streamlines around the filament and between the filament and the perspex plate for 256 x magnification.; steady solution case of Re_t=0.60, 100x100 grid ($\Delta x_{channel}$=8.58μm, $\Delta y_{channel}$=6.54μm), $u_{max,input}$=3.0mm/s, A_C=10μm, h=200μm, $l_{perspex}$=5mm, $\Delta\psi$=2.96$\cdot 10^{-9}$ m^2/s.

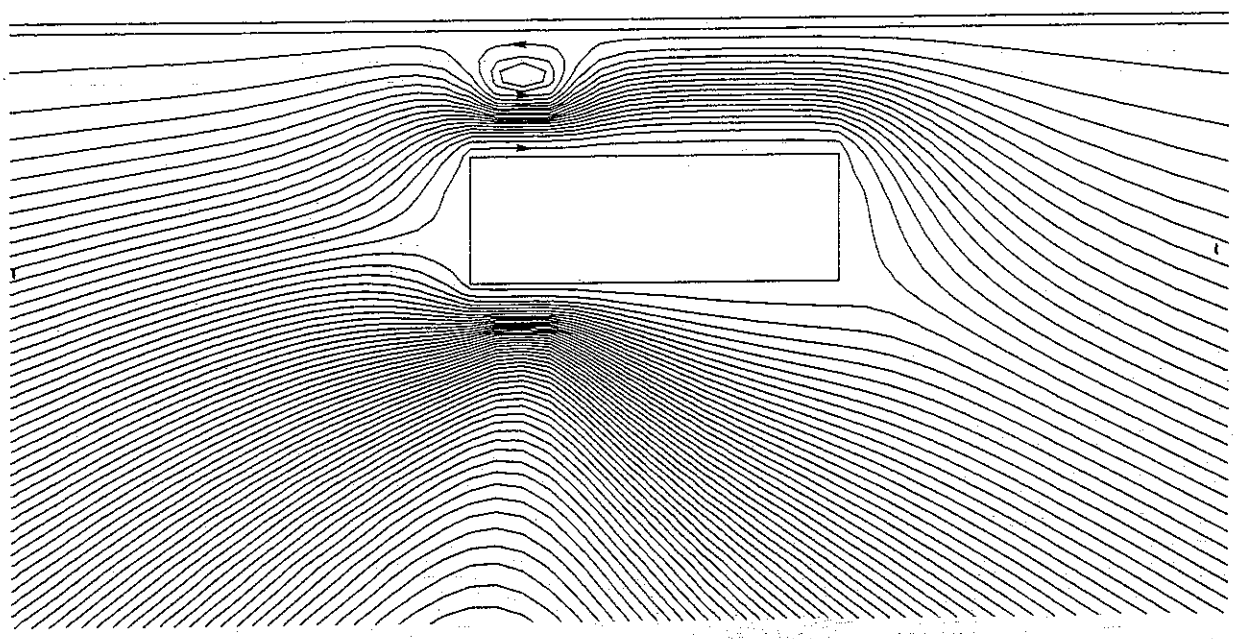

Figure 26a. Streamlines around the filament and between the filament and the perspex plate for 256 x magnification.; steady solution case of Re_t=0.12, 100x100 grid ($\Delta x_{channel}$=8.58μm, $\Delta y_{channel}$=2.0μm), $u_{max,input}$=3.0mm/s, A_c=10μm, h=40μm, $l_{perspex}$=5mm, $\Delta\psi$=1.82·10^{-9} m^2/s.

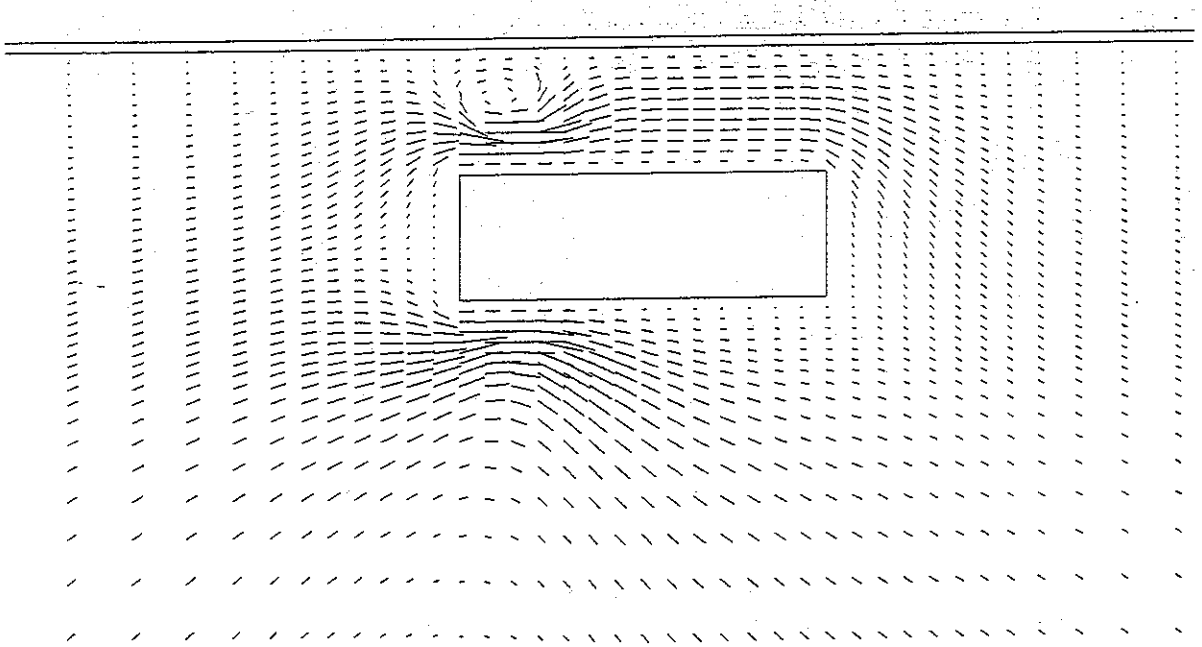

Figure 26b. Velocity vectors around the filament and between the filament and the perspex plate for 256 x magnification.; steady solution case of Re_t=0.12, 100x100 grid ($\Delta x_{channel}$=8.58μm, $\Delta y_{channel}$=2.0μm), $u_{max,input}$=3.0mm/s, A_c=10μm, h=40μm, $l_{perspex}$=5mm.

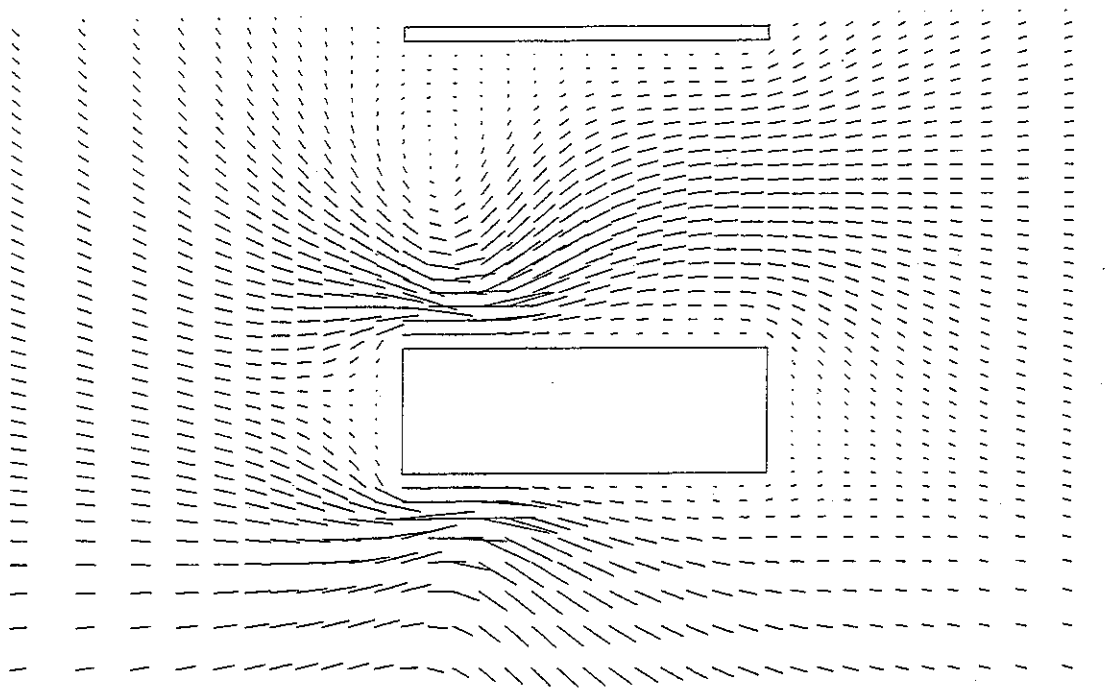

Figure 27. Velocity vectors around the filament and between the filament and the perspex plate for 256 x magnification.; steady solution case of Re_t=0.30, 100x100 grid ($\Delta x_{channel}$=8.58μm, $\Delta y_{channel}$=4.56μm), $u_{max,input}$=3.0mm/s, A_c=10μm, h=100μm, $l_{perspex}$=120μm.

Appendix

Fourier coefficients (see eq.(31))

$$a_0 = \frac{4U_e - 16U_r}{5\pi}$$

$$a_n = \frac{U_e}{\pi}\left[\frac{1-\cos(1-2n/5)\pi}{5-2n} + \frac{1-\cos(1+2n/5)\pi}{5+2n}\right] +$$

$$\frac{\sqrt{2}U_r}{\pi}\left[\frac{\cos(3/4-6/5n)\pi\cdot\sin(1/2-4/5n)\pi - \sin(3/4-6/5n)\pi\cdot\sin(1/2-4/5n)\pi}{5/4-2n} +\right.$$

$$\left.\frac{\cos(3/4+6/5n)\pi\cdot\sin(1/2+4/5n)\pi - \sin(3/4+6/5n)\pi\cdot\sin(1/2+4/5n)\pi}{5/4+2n}\right]$$

$$b_n = \frac{U_e}{\pi}\left[\frac{\sin(1-2n/5)\pi}{5-2n} - \frac{\sin(1+2n/5)\pi}{5+2n}\right] +$$

$$\frac{\sqrt{2}U_r}{\pi}\left[\frac{-\sin(3/4-6/5n)\pi\cdot\sin(1/2-4/5n)\pi - \cos(3/4-6/5n)\pi\cdot\sin(1/2-4/5n)\pi}{5/4-2n} +\right.$$

$$\left.\frac{\sin(3/4+6/5n)\pi\cdot\sin(1/2+4/5n)\pi + \cos(3/4+6/5n)\pi\cdot\sin(1/2+4/5n)\pi}{5/4+2n}\right]$$

Nomenclature

Latin symbols

a_0	Fourier coefficient	(–)
a_n	Fourier coefficient	(–)
a_E	east coefficient of discretized equation	(kg/m³)
a_N	north coefficient of discretized equation	(kg/m³)
a_P	central point of discretized equation	(kg/m³)
a_S	south coefficient of discretized equation	(kg/m³)
a_W	west coefficient of discretized equation	(kg/m³)
A_c	penetration amplitude	(m)
$\mathbf{A}$	tridiagonal matrix	(–)
$\mathbf{b}$	source vector	(–)
b_n	Fourier coefficient	(–)
C_D	drag coefficient	(–)
C	drag coefficient	(–)
d	cylinder diameter	(m)
f	frequency ($f=\omega/2\pi$)	(1/s)
$\mathbf{f}$	volume force ($f=(f_x,f_y)$)	(N/m³)
f_x	volume force in x–direction	(N/m³)
f_y	volume force in y–direction	(N/m³)
h	channel width	(m)
k	wave number ($k=2\pi/\lambda$)	(1/m)
l	length scale	(m)
L	cilium length	(m)
p	thermodynamic pressure	(Pa)
p_∞	thermodynamic pressure at infinity	(Pa)
Pe_c	cell Peclet number ($Pe_c=u\Delta x/\nu$)	(–)
r	residual at each grid point	(N/m³)
R^0	total residual in sweep number one	(N/m³)
R^n	total residual in sweep number n	(N/m³)
Re_c	cilia Reynolds number ($Re_c=d(u_c-u_f)/\nu$)	(–)
Re_r	rotational Reynolds number ($Re_r=\rho\omega/\nu$)	(–)
Re_t	translational Reynolds number ($Re_t=\bar{l}U/\nu$)	(–)
s_v	source term	(N/m³)
s_c	source term	(N/m³)
t	time	(s)
Δt	time step	(s)
Δt	CFL–criterion	(s)
T	beat period	(s)
u	velocity component in x–direction	(m/s)
u_c	cilia velocity in x–direction	(m/s)
u_f	flow velocity in x–direction	(m/s)
u_{max}	maximum velocity in effective stroke	(m/s)
u_s	streaming velocity	(m/s)
U	velocity scale for x–direction	(m/s)
U_e	velocity amplitude in effective stroke	(m/s)
U_r	velocity amplitude in recovery stroke	(m/s)
U_s	mean streaming velocity	(m/s)
v	velocity component in y–direction	(m/s)

v_c	cilia velocity in y–direction	(m/s)
v_f	flow velocity in y–direction	(m/s)
$\mathbf{v}$	velocity vector ($\mathbf{v}$=(u,v))	(m/s)
v_{tip}	tip speed of cilium in effective stroke	(m/s)
V	velocity scale for y–direction	(m/s)
x	x–coordinate	(m)
$\mathbf{x}$	dependent variable vector	(–)
Δx	grid spacing in x–direction	(m)
y	y–coordinate	(m)
Δy	grid spacing in y–direction	(m)
Δy_{eff}	distance to wall in effective stroke	(m)
Δy_{rec}	distance to wall in recovery stroke	(m)
z	z–coordinate	(m)

Greek symbols

λ	wavelength (λ=2π/k)	(m)
μ	dynamic viscosity of the fluid	(Pa·s)
ν	kinematic viscosity of the fluid	(m^2/s)
ρ	fluid density	(kg/m^3)
ρ_f	fluid density	(kg/m^3)
φ	dependent variable	(–)
ω	radian frequency (ω=2πf)	(radian/s)

References

Aiello,E. & Sleigh,M.A.
The metachronal wave of lateral cilia of Mytilus edulis
The Journal of Cell Biology, vol.54, p.493–506, 1972

Batchelor,G.K.
An introduction to fluid dynamics
Cambridge, 1967

Brennen,C. & Winet,H.
Fluid mechanics of propulsion by cilia and flagella.
Annual Review of Fluid Mechanics, p.339–398, 1977

Cheer,A.Y.L. & Koehl,M.A.R.
Paddles and Rakes: fluid flow through bristled appendages of small organisms
Journal of Theoretical Biology, vol.129, p.17–39, 1987

Duck,P.W.
Oscillatory flow inside a square cavity
Journal of Fluid Mechanics, vol.122, p.215–234, 1982

Gervang, Bo
Numerical fluid mechanics: description of common solution algorithms in finite volume calculations
Department of Fluid Mechanics, Techn. Univ. of Denmark, 1988

Issa,R.I.
Solution of the implicitly discretised fluid flow equations by operator–splitting
Journal of Computational Physics, vol.62, p.40–65, 1985

Issa,R.I.
The computation of compressible and incompressible recirculating flows by a non–iterative implicit scheme
Journal of Computational Physics, vol.62, p.66–82, 1986

Jørgensen,C.B.
On gill function in the mussel Mytilus edulis L.
Ophelia, vol.13, p.187–232, 1975

Jørgensen,C.B.
Fluid mechanics of the mussel gill: The lateral cilia
Marine Biology, vol.70, p.275–281, 1982

Jørgensen,C.B., Famme,P., Kristensen,H.S., Larsen,P.S., Møhlenberg,F., Riisgård,H.U.
The bivalve pump
Marine Ecology, vol.34, p.69–71, 1986

Kiørboe,T., Møhlenberg,F. & Nøhr,O.
Feeding, particle selection and carbon absorption in Mytilus edulis in different mixtures of algae and resuspended bottom material
Ophelia, vol.19, p.193–205, 1980

Moffatt,K.
Viscous and resistive eddies near a sharp corner
Journal of Fluid Mechanics, vol.18, p.1–18, 1964

Møhlenberg,F. & Riisgård,H.U.
Filtration rate, using a new indirect technique, in thirteen species of suspension–feeding bivalves
Marine Biology, vol.54, p.143–148, 1979

Owen,G.
Studies on the gill of Mytilus edulis: the eu–latero–frontal cirri
Proceedings of Royal Society, London, vol.B 187, p.83–91, 1974

Pan,F. & Acrivos,A.
Steady flow in rectangular cavities
Journal of Fluid Mechanics, vol.28, p.643–656, 1967

Patankar,S.V.
Numerical heat transfer and fluid flow
Hemiphere, Washington,D.C. 1980

Peaceman,D.W. & Rachford,H.H.
The numerical solution of parabolic and elliptic differential equations
Journal of Soc. Ind. Appl. Math., vol.3, p.28, 1955

Samarski,A. & Nicolatev,E.
Methodes de resolution des equations de maille
Ed. Moscow, (1981)

Satir,P.
How cilia move
Scientific American, vol.10, p.45–52, (1974)

Sleigh,M.A. & Aiello,E.
The movement of water by cilia
Acta Protozoologica, vol.11, p.265–277, 1972

Walne, P.R.
The influence of current speed, body size and water temperature on the filtration rate of five species of bivalves
Journal of the Marine Biological Association of the United Kingdom, vol.52, p.345–374, 1972